FACULTY OF ENGINEERING AND ARCHITECTURE

On-Chip Carbon Dioxide Sensor Based on Non-Dispersive Infrared Spectroscopy

Xiaoning Jia

Doctoral dissertation submitted to obtain the academic degree of
Doctor of Photonics Engineering

Supervisors
Prof. Roel Baets, PhD - Prof. Günther Roelkens, PhD

Department of Information Technology
Faculty of Engineering and Architecture, Ghent University

April 2021

GHENT UNIVERSITY

ISBN 978-94-6355-477-0
NUR 959
Wettelijk depot: D/2021/10.500/25

Members of the Examination Board

Chair

Prof. Filip De Turck, PhD, Ghent University

Other members entitled to vote

Prof. Bart Kuyken, PhD, Ghent University
Prof. Jeroen Missinne, PhD, Ghent University
Prof. Delphine Morini, PhD, Université Paris-Saclay, France
Joris Roels, PhD, Melexis Technologies

Supervisors

Prof. Roel Baets, PhD, Ghent University
Prof. Günther Roelkens, PhD, Ghent University

Acknowledgements

Doing a PhD is a challenging but undeniably exciting and fruitful experience, and it's been a quite unforgettable 4-year journey in my life. Looking back, I now feel so happy and fortunate that I had this chance to pursue a PhD degree in a world-renowned research group and a lovely city like Gent. This PhD wouldn't have been possible without the help and support from many people: my colleagues, friends, and my family. First of all, I would like to give my deepest (and deepest) gratitude to my PhD promoters: Prof. Roel Baets, Prof. Gunther Roelkens, and my industrial advisor Dr. Joris Roels. Roel, thank you very much for taking me in when I knocked the door of your office with the ambition of doing a PhD in the Photonics Research Group. Your warm smile was the beginning of my wonderful 4-year PhD journey, and it has been filled with your kind guidance and numerous advice ever since. The countless discussions I had with you really inspired me, and I hope one day I can have the same mind as deep and broad as yours. Gunther, thank you for your help and patient guidance when I came to you with problems that I can't solve, your 'no problem, that's what I'm here for' really eased my anxiety. I deeply appreciate your recognition of my work and your kind reminder when I was about to deviate from the right path. Joris, thank you for providing precious thoughts and ideas from the industrial point of view, you have been a very good mentor as well as a friend. I would also like to thank Melexis and Vlaio for funding this PhD project, this PhD would not have been possible without your financial support.

Second, I would like to express my gratitude to the people who provided help and support with their expertise and precious time in the course of this PhD. Jasper, it was very nice of you that you didn't even hesitate to help when I asked you to layout the PCBs and to make some cables. Steven and Muhammad, thank you both very much for answering my numerous processing and training requests, and for the countless useful discussions regarding clean room processing. Liesbet, thank you for helping me take the nice pictures with the SEM and FIB. Kristof Dhaenens, Sheila Dunphy and Stijn Duynslager, thank you for your help in the film lamination and wafer dicing. Joris Van Kerrebrouck, I sincerely appreciate your efforts in helping with the amplifier design and solving all kinds of electronics problems. Michael Vanslembrouck and Peter Guns, your help in setting up my measurement are greatly appreciated. Of course, many thanks go to the supporting

and administrative staff: Ilse Van Royen, Kristien De Meulder, Ilse Meersman, Mike Van Puyenbroeck, and Bert Coryn, my work and life in Gent went a lot smoother with your help.

I would also like to express my thanks to my colleagues in the Photonics Research Group, thank you for making my work and life at Gent joyful because of your help and delightful conversations. Anton, I learned a lot from you in our useful discussions when I just started my PhD. Jeroen, thank you for being a good friend with whom I could share my worries and joy, and I'm grateful that we could cheer each other up when we were in the valleys of our PhDs. My lovely office mates: Kristof, Stephane, Khannan, Ivo, Ana, Iman, thank you for making a pleasant working environment. Kristof, you've been a very good neighbor, I can still recall our common sighs and laughter when we were stressed.

2020 is a tough year due to the Corona outbreak, and we were forced to work from home and be isolated from each other. I would like to give my special thanks to my Chinese colleagues for your company in the year of 2020 and the years before it: Yuting, Xiaomin, Chonghuai, Xiangfeng, Zuyang, Yang, Jing, Haolan, Yufei, Yanlu, Chupao, Zhongtao, Chao, Mi and Hong. My four years of PhD would have been a quite lonely experience if it were not for you guys.

Finally, I would like to sincerely thank my parents, my brother, and my sister. As the youngest family member, I've grown up with your whole-hearted love and support. Although we do not speak out our love and feelings that much, I know that we all have enormous love for each other. To my lovely parents: I've worked hard towards a master and a PhD degree, I really appreciate your support and understanding in the past years, I hope I have made you very proud.

Gent, December 2020
Xiaoning Jia

Table of Contents

List of Figures

List of Tables

List of Acronyms

A

AFM	Atomic Force Microscope
ASIC	Application-Specific Integrated Circuit

B

BOX	Buried Oxide

C

CO2	Carbon Dioxide
CMOS	Complementary Metal Oxide Semiconductor

D

DRIE	Deep Reactive Ion Etching
DCV	Demand Controlled Ventilation

E

EIC	Electrical integrated Circuit
EMI	Electromagnetic Interference

F

FWHM	Full Width at Half Minimum

G

GaSb	Gallium Antimonide
GWP	Global Warming Potential
GC	Gas Chromatography

I

IoT	Internet of Things
IC	Integrating Cylinder
IR	Infra Red

L

LOD	Limit of Detection
LED	Light Emitting Diode

M

MAC	Mobile Air Conditioning
MEMS	Micro-Electro-Mechanical System
MIR	Mid-Infrared
MOS	Metal Oxide Semiconductors
MZI	Mach–Zehnder Interferometer

N

NDIR	Non-Dispersive Infrared
NEP	Noise Equivalent Power
NIR	Near Infra Red

P

PAS	Photoacoustic Spectroscopy
PCB	Printed Circuit Board
PD	Photodiode
PIC	Photonic Integrated Circuit
PMMA	Poly MethylMethAcrylate
PTS	Photothermal Spectroscopy

Q

QCW	Quasi-Continuous Wave

R

RH	Relative Humidity
RI	Refractive Index
RMS	Root Mean Square

S

SEM	Scanning Electron Microscope
SNR	Signal to Noise Ratio
SOI	Silicon on Insolator

T

TDLAS	Tunable Diode Laser Absorption Spectroscopy
TE	Transverse-electric
TIA	Trans-Impedence Amplifier
TM	Transverse-magnetic

Nederlandse samenvatting –Summary in Dutch–

De marktvraag naar een kleine en goedkope CO_2 – gassensor is snel groeiend. Een dergelijke CO_2 – sensor is van groot belang voor veel toepassingen zoals het monitoren van de luchtkwaliteit binnen gebouwen, het monitoren tuinbouwserres waarin gewassen gekweekt worden en ook het monitoren van allerlei fabricageprocessen in de algemene industrie. In het bijzonder heeft de Europese Unie een gradueel verbod geïntroduceerd op fluorgassen in mobiele airconditioningssystemen (MAC) omwille van het milieu en brandveiligheid. Het is daardoor duidelijk dat CO_2 een geschikte kandidaat is om de fluorgassen te vervangen als koelgas in de MAC koelsystemen. Echter, het risico op een CO_2 lek bestaat, wat zich vertaalt naar een risico voor de personen in de wagen, en bijgevolg ook voor de andere voertuigen in het verkeer. Vandaar de nood aan een heel responsieve CO_2 sensor die een mogelijk lek kan detecteren en bijgevolg de inzittenden kan waarschuwen voor dit lek. De afzetmarkt voor snelle en goedkope CO_2 sensoren in mobiele MAC systemen in bijvoorbeeld auto's is dan ook enorm groot.

Verschillende technologieën zijn vandaag beschikbaar op de markt als een CO_2 sensor, gaande van elektrochemische detectie tot katalytische detectie en spectroscopische methodes. Elektrochemische en katalytische methodes kunnen voordelig zijn in termen van kost, maar zijn nadelig op vlak van stabiliteit op lange termijn, lage duurzaamheid en kruisreactiviteit met andere gassen. Daarentegen bieden spectroscopische technieken een betere stabiliteit op lange termijn, zijn ze ook nauwkeurig en kunnen ze gemakkelijk een onderscheid maken tussen verschillende gassen. Spectroscopische gasdetectie is gebaseerd op de 'vingerafdruk' analyse van de absorptielijnen van het specifiek gas in het infrarode golflengtebereik (op ongeveer $4.26\mu m$ voor CO_2). Tussen de verschillende spectroscopische methodes onderscheidt niet-dispersieve infrarood (NDIR) spectroscopie zich als de beste kandidaat voor CO_2 detectie op basis van de relatief eenvoudige implementatie, de compactheid van de sensor en het veel lagere kostplaatje van de gehele sensor. Daarbovenop valt een lage kruissensitiviteit op te merken omwille van de zeer hoge CO_2 absorptiecoëfficiënt bij $4.26\mu m$ ten opzichte van de laag tot zeer lage absorptie coëfficiënten van andere gassen bij dezelfde golflengte. Omwille van de bovenstaande redenen wordt de markt van CO_2 sensoren voornamelijk bezet door de NDIR-sensoren. Echter, de huidige generatie NDIR-sensoren zijn groot, met een optische interactielengte van enkele centimeters om tot een detectielimiet te komen van 100 moleculen per miljoen. Bovendien zijn ze ook duur

omdat ze geassembleerd zijn met discrete optische elementen, wat wederom bijdraagt tot hun omvang. Dit alles voorkomt het gebruik van de huidige generatie NDIR CO_2 sensoren in prijs- en groottegevoelige markten zoals de automotive markt.

De doelstelling van dit doctoraatsonderzoek is het ontwikkelen van een drastisch kleinere en goedkopere NDIR CO_2 sensor die gefabriceerd kan worden op grote schaal, op basis van wafer-processen zoals in de elektronica gebeurt. Er zijn drie paden onderzocht om een dergelijke grote sensor te verkleinen tot een grootte die past op een silicium chip, namelijk: de 'multi-slot' veelvoudige-gleufgolfgeleider, de holle metallische golfgeleider en de holle geïntegreerde cilinder. De holle geïntegreerde cilinder is uiteindelijk gekozen als de beste kandidaat op basis van een lager stroomverbruik, eenvoudigere fabricagetechnieken en lagere productiekost ten opzichte van de andere kandidaten. De geïntegreerde cilinder kan beschouwd worden als het 2D equivalent van een 3D integrerende sfeer die op een chip past. Zoals bij een integrerende sfeer, kan het licht veelvoudig reflecteren in de cilinder, wat ertoe leidt dat het licht een lange interactielengte kan hebben met het gas. In dit doctoraatsonderzoek is de integrerende cilinder zowel numeriek als experimenteel onderzocht. De eerste CO_2 gasmetingen zijn uitgevoerd met externe optische lichtbronnen en detectoren. Naderhand zijn de lichtbron en detectoren ook geïntegreerd op dezelfde silicium chip als de sensor. In dit werk worden de volgende eigenschappen bestudeerd: de sensorreactie naar CO_2, de reactietijd van de sensor, de kruis-gevoeligheid van de sensor naar water en de lange-termijnstabiliteit van de sensor. Enkele praktische aspecten zoals de compensatie voor signaaldrift door temperatuurschommelingen en bescherming door een gasmembraan worden ook kort besproken.

Niet-dispersieve infraroodspectroscopie

Een typische NDIR optische sensor bestaat uit twee kanalen: een detectiekanaal en een referentiekanaal. Het uitgezonden licht (met emissie rond $4.26\mu m$) wordt spectraal gefilterd en belicht vervolgens twee fotodetectoren. Voor het detectiekanaal overlapt het gefilterde lichtspectrum met de absorptieband van CO_2, zodat de lichtintensiteit afneemt bij toenemende CO_2 -concentratie. De hoeveelheid absorptie van het licht wordt goed beschreven door de wet van Beer-Lambert:

$$I = I_0 \exp(-\alpha_{gas} c_{gas} L) \tag{1}$$

Hier is α_{gas} de absorptiecoëfficiënt van het te onderzoeken gas per ppm gas, hier CO_2. C_{gas} is de gasconcentratie in ppm en L is de lengte van het optische pad in het detectiekanaal. Bij het referentiekanaal verandert de lichtintensiteit niet wanneer de concentratie van het te onderzoeken gas verandert. Dit kan worden bereikt door een andere golflengte te gebruiken, waarbij geen van de gewoonlijke gassen absorberen (in het geval van CO_2 sensors is dit gewoonlijk $3.9\mu m$), of door het referentiekanaal te isoleren van de omgeving. Het gebruik van een referentieka-

naal is voornamelijk bedoeld om invloeden zoals fluctuaties in de intensiteit van de lichtbron en andere gedeelde ruis te elimineren.

On-Chip CO_2-detectie op basis van een integrerende cilinder

De integrerende cilinder bestaat uit een cilindrische caviteit met een metallisch laagje op de wanden. De caviteit wordt afgesloten door het samenbinden van twee silicium substraten onder hoge druk. Om de optimale configuratie te vinden van de integrerende cilinder wordt er gebruik gemaakt van simulatiesoftware die lichtstralen met reflecties kan volgen in een 3D ruimte. De simulatieresultaten tonen aan dat voor een gegeven cilinder met een bepaalde straal (R), hoogte (h) en breedte van de toegangsgolfgeleiders (d) kunnen worden geoptimaliseerd om de gevoeligheid van de integrerende cilinder te maximaliseren. Voor de experimentele uitvoering kiezen we bijgevolg voor een cilinder met straal $R = 2.0mm$, hoogte $h = 300\mu m$ en breedte van de toegangsgolfgeleider $d = 200\mu m$. Een dergelijke geïntegreerde cilinder levert een equivalente optische padlengte op van 3.5 cm, en een netto vermogensverlies van -7.4 dB. De fabricage van de sensor maakt gebruik van een diepe reactieve-ionen-etsstap (DRIE) om het silicium te etsen, de depositie van goud op de wanden van de caviteit en het aan elkaar binden van twee substraten om de caviteit te sluiten. Dit zijn allemaal processtappen die compatibel zijn het processen van elektronische / MEMS wafers. Daardoor is het mogelijk om de sensor te fabriceren op grote schaal, en bijgevolg met een lage kost.

Om de CO_2 gassensor experimenteel te testen is er een specifieke meetopstelling gebouwd zoals voorgesteld in Figuur 1(a). Het infrarode licht dat wordt uitgestraald door een breedbandige thermische bron (waarvan het emissiespectrum getoond wordt in Figuur 1 (c)) koppelt in aan de toegangspoort van de golfgeleider via een optische vezel. Het licht wordt gemoduleerd door een optomechanische modulator die periodiek de doorgang van licht tot de golfgeleider blokkeert. De modulator is geplaatst tussen de optische vezel en de toegangspoort van de golfgeleider. De twee golfgeleiders die als uitgangspoorten dienen van de integrerende cilinder worden gebruikt als het detectiekanaal en het referentiekanaal. In het detectiekanaal wordt het licht gedetecteerd door een fotodiode op kamertemperatuur. De opgewekte fotostroom wordt eerst versterkt door een transimpedantieversterker (TIA) en vervolgens door een lock-in versterker. Het enige verschil tussen het referentiekanaal en het detectiekanaal is de gekozen golflengte: $4.26\mu m$ en $3.9\mu m$. De selectie van de gewenste golflengte (spectrale filtering) in elk kanaal wordt bereikt door twee optische banddoorlaatfilters. Voorts zijn de twee kanalen identiek.

Eerst wordt een Allan-deviatie meting uitgevoerd voor het bepalen van het niveau van de systeemruis en het vinden van de optimale integratietijd van de lock-in versterkers. De detectielimiet van de sensor is bij benadering 2x10-4 AU (absorbance units), over een integratietijd van 1 seconde. De respons van de sensor op

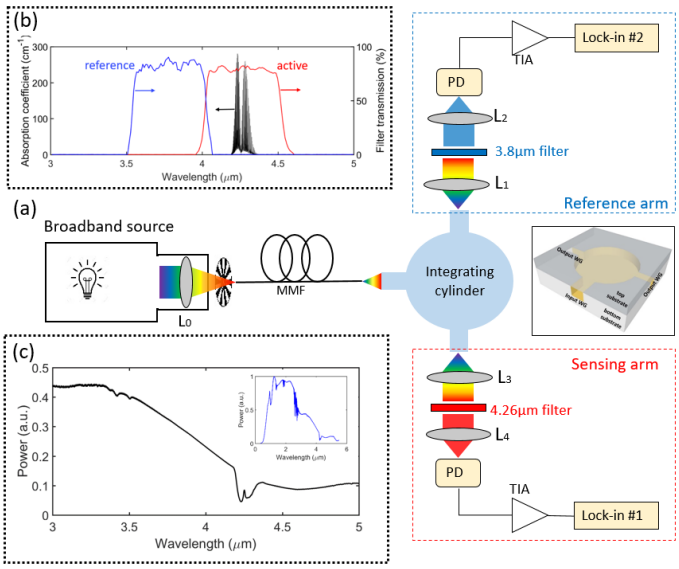

Figuur 1: (a) Specifieke meetopstelling voor het karakteriseren van de integrerende cilindrische gassensor. (b) De transmissiespectra van de optische filters in het detectiekanaal (rood) en het referentiekanaal (blauw). (c) Emissiespectra van de lichtbron in het golflengtegebied tussen 3 en 5 μm.

variërende CO_2 concentraties wordt getest door de geïntegreerde sensor te koppelen aan een externe gastoevoer. Met deze externe gastoevoer kan op een gecontroleerde manier CO_2 toegevoerd worden waarvan de concentratie extern regelbaar is. Figuur 2 (a) toont zowel het detectiesignaal als het referentiesignaal wanneer de CO_2-concentratie wordt gevarieerd.

Het is duidelijk dat wanneer de CO_2-concentratie toeneemt, het detectiesignaal afneemt door absorptie van het licht, terwijl het referentiesignaal relatief stabiel blijft. Om de gemeenschappelijke ruis op beide kanalen te elimineren, wordt het detectiesignaal genormaliseerd ten opzichte van het referentiesignaal en wordt het genormaliseerde signaal getoond in Figuur 2 (b). Men kan zien dat na de normalisatie de gemeenschappelijke fluctuaties op beide signalen worden verwijderd, waardoor het genormaliseerde signaal van hogere kwaliteit is. De detectielimiet van de sensor is ongeveer 100 ppm, wat consistent is met de voorspellingen van de Allan-afwijkingsmeting. De reactietijd van de sensor wordt gemeten door de integrerende cilinder eerst bloot te stellen aan een gasmengsel met 50% CO_2 en vervolgens de gasstroom abrupt af te sluiten. Uit deze meting is duidelijk dat de sensor een korte reactietijd heeft van slechts 2.6 seconden, dit dankzij de kleine oppervlakte van de geïntegreerde cilinder (5 mm bij 5 mm).

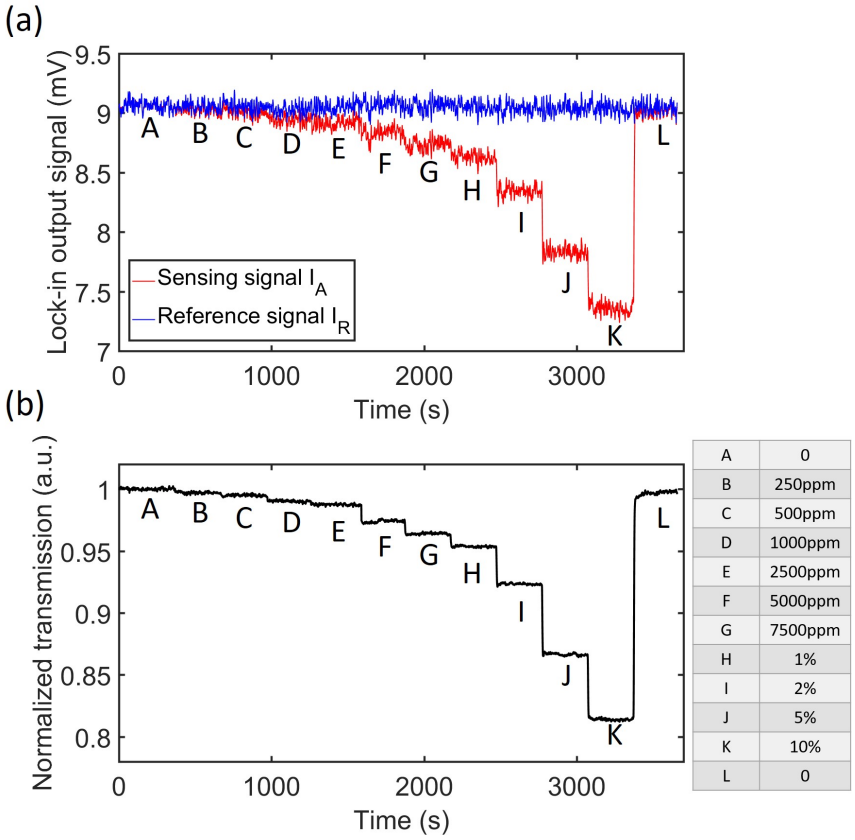

Figuur 2: (a) Signaalrespons van zowel het detectiekanaal (rood) als het referentiekanaal (blauw) voor verschillende opgelegde CO_2 concentraties. (b) De genormaliseerde signaalrespons, verkregen door de normalisatie van het detectiekanaalsignaal ten opzichte van het referentiekanaalsignaal. Een legende van de verschillende opgelegde CO_2 concentraties is weergegeven in de tabel aan de rechterzijde.

Volledig geïntegreerde NDIR CO_2-sensor

Een combinatie van een LED en fotodiode, die spectraal is afgestemd op de absorptieband van CO_2, wordt gebruikt als de optische bron en detector voor de volledig geïntegreerde sensor. Het gebruik van de relatief goedkope componenten elimineert de noodzaak van de opto-mechanische modulator en de optische filters, waardoor de CO_2-sensor zowel compact als goedkoop te maken valt. Voor het referentiekanaal wordt een fotodiode gebruikt die licht detecteert tot een golflengte van $4\mu m$, maar niet hoger. Op deze wijze verandert het referentiesignaal niet wanneer de CO_2-concentratie wijzigt, aangezien de CO_2 absorptie plaatsvindt voor golflengtes groter dan $4\mu m$. De LED en de fotodiodes zijn geïntegreerd op het on-

derliggende siliciumsubstraat door middel van een flipchip bindingsmechanisme. Vervolgens wordt de half-open cilindrische caviteit aangesloten en de uiteindelijke sensor gevormd door middel van het aan elkaar binden van beiden substraten. Het schema van de volledig geïntegreerde sensor wordt getoond in Figuur 3. Na de

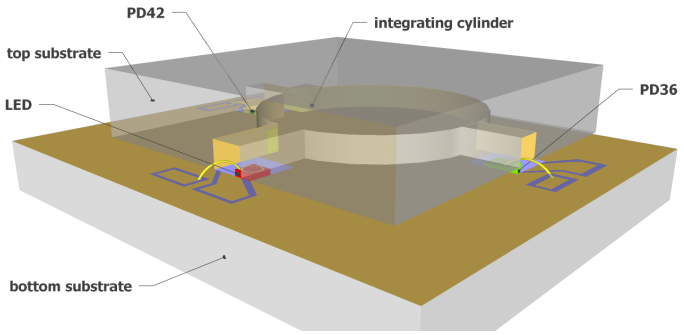

Figuur 3: Een 3D schematische voorstelling van de volledig geïntegreerde NDIR CO_2 sensor. De sensor bestaat uit twee verschillende substraten die met elkaar verbonden worden. In het bovenste substraat wordt de geïntegreerde cilindrische caviteit gevormd. Op het onderste substraat zijn de lichtbron en fotodiodes aangebracht.

fabricage is de sensor gemonteerd op een printplaat (PCB) met twee TIA's om beide kanalen uit te lezen. De sensor werkt in quasi continu bedrijf (CW). In deze modus levert de LED het meeste licht, maar verbruikt hij ook het meeste elektrische vermogen. De signaalrespons van de sensor in de CW-modus is weergegeven in Figuur 4. In tegenstelling tot eerder metingen, waarbij de lichtbron en detectoren niet geïntegreerd waren op de chip, is hier nog een merkbare ruis waar te nemen op het genormaliseerde signaal. Dit valt toe te kennen aan de onbalans tussen de beide kanalen. Ook zijn er geen optische filters aanwezig, waardoor de bandbreedte van het licht in het detectiekanaal groter is dan voordien. Beide oorzaken dragen ertoe bij dat de detectielimiet van de geïntegreerde sensor licht verslechtert is ten opzichte van de eerste configuratie. Ook is de kruisgevoeligheid met waterdamp nderzocht en er is geen noemenswaardige kruisgevoeligheid vastgesteld. Verdere simulaties bevestigen dat deze kruisgevoeligheid onder de CO_2-detectielimiet van de sensor ligt. Voor het nagaan van de stabiliteitseigenschappen van de sensor op lange termijn, werd deze gedurende vijf dagen blootgesteld aan de omgevingslucht. Uit deze resultaten blijkt dat de stabiliteit afhankelijk is van temperatuurfluctuaties van de lucht in het laboratorium. Deze afhankelijkheid aan de temperatuur kan in toekomstige iteraties uit de signaalrespons genormaliseerd worden door de sensor te pre-kalibreren en het apart monitoren van de temperatuur van de chip.

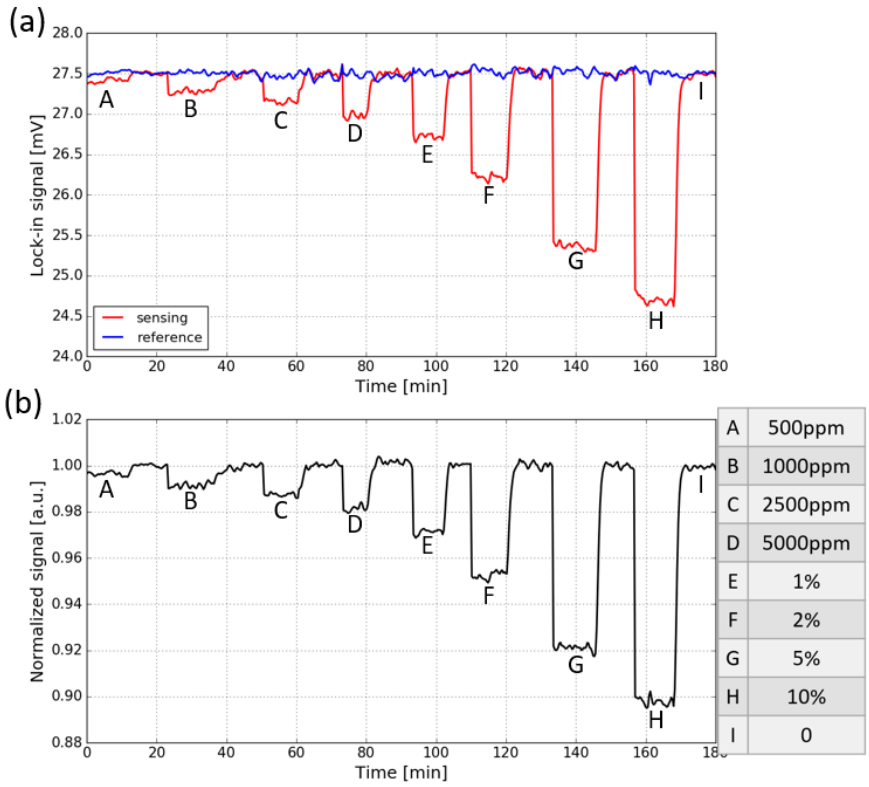

Figuur 4: (a) Signaalrespons van het detectiekanaal (rood) en het referentiekanaal (blauw) van de volledig geïntegreerde sensor aan verschillende CO_2 gasconcentraties. (b) De genormaliseerde signaalrespons, verkregen door de normalisatie van het detectiekanaalsignaal ten opzichte van het referentiekanaalsignaal. Een legende van de verschillende opgelegde CO_2 concentraties is weergegeven in de tabel aan de rechterzijde.

English summary

The need for a miniaturized, low-cost CO_2 gas sensor is rapidly growing. Such a CO_2 sensor is of great importance in many applications such as air quality monitoring, greenhouse farming, and industry process control. In particular, as the European Union introduced a gradual ban on the usage of fluorinated gases in mobile air conditioning systems (MAC) for environmental and fire safety reasons, it is becoming clear that CO_2 is a suitable substitute for MAC refrigerants. However, concerns about the potential leakage of CO_2 on board arises, as the CO_2 concentration in the cabin can quickly reach up to a few percent and it imposes a high risk for the people on board as well as for the traffic. To address this problem, a fast responsive CO_2 sensor is needed on board to identify the leakage and thus removing the safety concerns. The application in MAC systems opens a huge new market for fast, low-cost CO_2 sensors.

Different technologies are available today for CO_2 sensing, including electrochemical, catalytic and spectroscopic techniques. Electrochemical and catalytic techniques can be advantageous in terms of cost, yet they suffer from disadvantages such as short-term stability, low durability and cross-response to other gases. In contrast, spectroscopic techniques offer long-term stability, high accuracy and high gas specificity. Spectroscopic gas sensing is based on probing the 'fingerprint' absorption lines of the gas with optical radiation in the infrared wavelength range ($4.26\mu m$ for CO_2 sensing). Among the various spectroscopic techniques, non-dispersive infrared (NDIR) spectroscopy stands out as the most appropriate method for CO_2 sensing due to its simple implementation, compactness, and low cost. Furthermore, the large absorption coefficient of CO_2 at $4.26\mu m$ and the negligible overlap with the absorption bands of common gases provide high sensitivity and low cross-sensitivity. For these reasons, the CO_2 sensor market is largely dominated by NDIR sensors. However, current NDIR sensors are bulky, as a long interaction length (a few cm) is required to achieve a sub-100ppm limit of detection. They are also expensive as they are based on discrete co-assembled optical elements. This all prevents their use in price- and size-sensitive markets.

The goal of this thesis is to develop a miniaturized, low-cost NDIR CO_2 sensor that can be realized on wafer-scale. To integrate a few cm-long interaction length on a silicon chip with a small footprint, three different approaches are proposed in this work: the multi-slot silicon waveguide, the hollow metallic waveguide, and the hollow integrating cylinder. The integrating cylinder is chosen as the optimal approach due to power budget considerations, as well as fabrication complexity and production cost. The integrating cylinder can be considered as the 2D ver-

sion of an integrating sphere implemented on-chip. As in an integrating sphere, the multiple reflections of the incident light inside the cylindrical cavity provides a long interaction length with the gas. In this work, the integrating cylinder is investigated both numerically and experimentally. CO_2 sensing measurements are performed using external optical source and detectors. After the proof-of-concept demonstration of the integrating cylinder, the optical source and detectors are integrated on-chip. The characterization of the fully integrated sensor, including CO_2 sensing response, response time, cross-sensitivity to water vapor, and the long-term stability of the sensor are presented. Practical aspects such as temperature drift compensation and gas membrane protection are briefly discussed.

Non-dispersive infrared spectroscopy

A typical NDIR optical sensor consists of two channels: the sensing channel and the reference channel. The light emitted from the optical source (with emission around $4.26\mu m$) is spectrally filtered and coupled to two photodetectors. For the sensing channel, the filtered light spectrum overlaps with the absorption band of CO_2, such that the light intensity decreases with increasing CO_2 concentration.The absorption is well described by the Beer-Lambert law:

$$I = I_0 \exp(-\alpha_{gas} c_{gas} L) \tag{2}$$

where α_{gas} is the absorption coefficient of the target gas per ppm, c_{gas} is the gas concentration in ppm, and L is the optical path length. At the reference channel, the light intensity does not change when the concentration of the target gas changes, which can be achieved either by using a reference wavelength at which no common gases absorb (typically at $3.9\mu m$ for CO_2 sensing), or isolating the reference channel from the ambient. The presence of the reference channel is mainly to eliminate influences such as source fluctuations and other common-mode noise.

On-Chip CO_2 sensing based on an integrating cylinder

The integrating cylinder consists of a metallized cylindrical cavity with access waveguides, formed by wafer bonding of two silicon substrates. To determine the optimal parameters of the integrating cylinder, 3D ray tracing simulations are carried out. The simulation results show that for a given cylinder with a certain radius (R) and height (h), the widths (d) of the access waveguides can be optimized to maximize the sensitivity of the integrating cylinder. For experimental characterization, we choose an integrating cylinder with a radius $R = 2.0mm$, height $h = 300\mu m$ and access waveguide widths $d = 200\mu m$. Such an integrating cylinder yields an optical path length of $3.5cm$ and a total propagation loss of 7.4dB. The fabrication of the integrating cylinder involves deep reactive ion etching (DRIE) of silicon, gold deposition and lift-off, and wafer bonding, which are

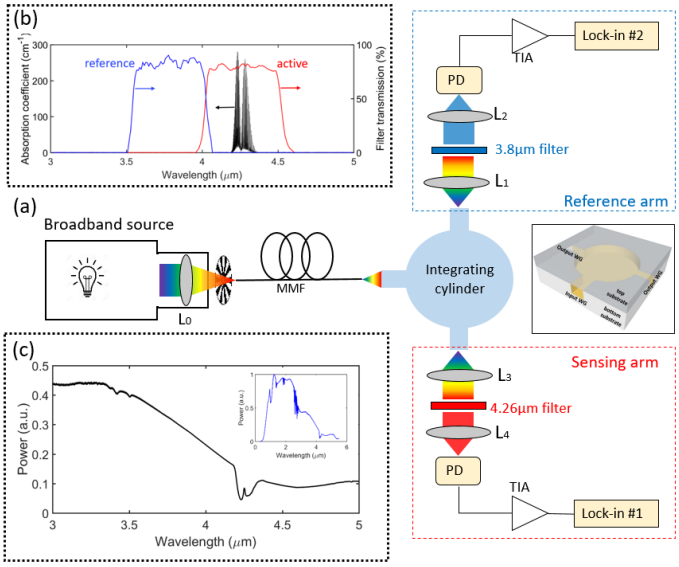

Figure 1: (a) Dedicated gas sensing setup to characterize the integrating cylinder. (b) Transmission spectra of the sensing and reference filters. (c) Emission spectrum of the light source in the $3\mu m - 5\mu m$ wavelength range.

all wafer scale fabrication techniques and therefore the sensor can be fabricated in large volume at low cost. To experimentally evaluate the fabricated integrating cylinder, a dedicated gas sensing setup as shown in Figure 1(a) is built. The infrared light emitted from a broadband thermal source (with emission spectrum shown in Figure 1(c)) is coupled into the input waveguide of the integrating cylinder by an optical fiber. An optical chopper is placed in between the source and the fiber to modulate the light. The two output waveguides of the integrating cylinder are used as the sensing channel and the reference channel. At the sensing channel, the output light is detected by an uncooled photodiode, and the photocurrent is first amplified by a trans-impedance amplifier (TIA) and then acquired by a lock-in amplifier. The only difference between the reference channel and the sensing channel is the working wavelength: $\lambda_{sens} = 4.26\mu m$ and $\lambda_{ref} = 3.8\mu m$, the wavelength selection is achieved by two optical band pass filters. The two channels are otherwise identical.

An Allan deviation measurement is first performed to determine the system noise and the optimal integration time of the lock-in amplifiers. The limit of detection of the sensing system is about 2×10^{-4} (in absorbance units, AU) at an integration time of 1 second. The response of the integrating cylinder to changes in CO_2 concentration is measured by feeding the integrating cylinder with a series of sample gases containing various concentrations of CO_2. Figure 2(a) shows both the sensing signal and the reference signal when the CO_2 concentration is varied. It can

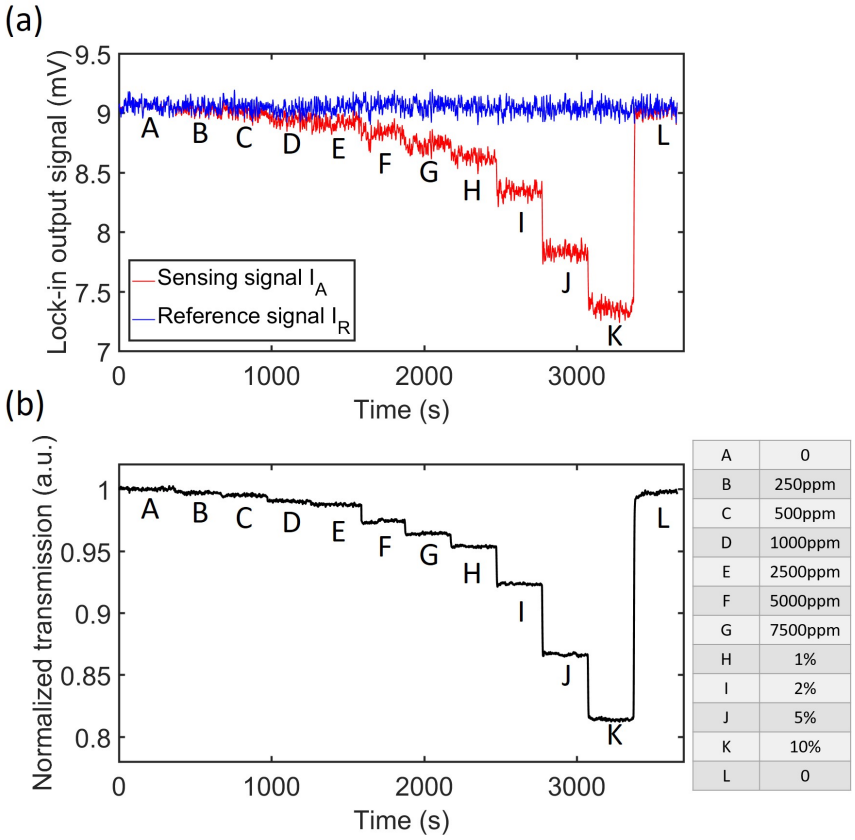

Figure 2: (a) Response of both sensing signal and reference signal to CO_2 concentration steps. (b) Normalized transmission, obtained by dividing the sensing signal with the reference signal. The CO_2 concentration steps are listed on the right side.

be seen that when the CO_2 concentration increases, the sensing signal decreases due to absorption, while the reference signal stays relatively stable. To eliminate the common mode noise present on both channels, the sensing signal is normalized w.r.t the reference signal and the normalized signal is shown in Figure 2(b). One can see that after normalization, the common fringes present on both signals are removed and the normalized signal becomes much more smooth. The limit of detection of the sensor is about 100ppm, which is consistent with the predictions from the Allan deviation measurement. The response time of the sensor is measured by first purging the integrating cylinder with 50% CO_2 and then abruptly shutting off the gas flow. The sensor has a short response time of only 2.6 seconds, owing to the small footprint of the integrating cylinder (5 mm$\times$5 mm).

Fully integrated NDIR CO_2 sensor

An LED-photodiode (PD) optopair spectrally matched to the absorption band of CO_2 is used as the optical source and the sensing photodiode for the fully integrated sensor. The use of the relatively cheap optopair bare chips eliminates the need for mechanical chopping and the optical filters, allowing for a compact and low-cost CO_2 sensor. For the reference channel, a photodiode with a cut-off wavelength at $4\mu m$ is used. In this way the reference signal will not change as a function of CO_2 concentration as there is no spectral overlap between the response of the photodiode and the CO_2 absorption band. The LED and the photodiode chips are integrated on the bottom silicon substrate by flip-chip bonding, after which the sensor is formed by wafer bonding of the top substrate (containing the integrating cylinder) and the bottom substrate. The schematic of the fully integrated sensor is shown in Figure 3.

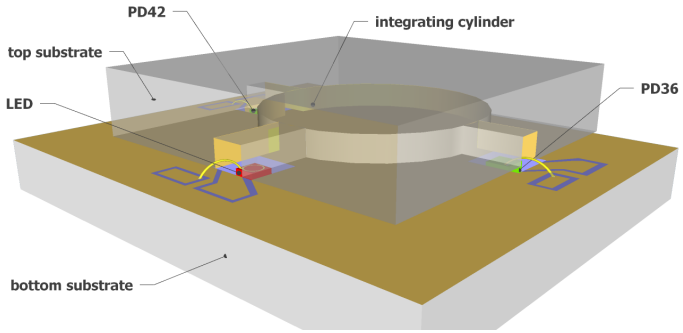

Figure 3: 3D schematic of the fully integrated NDIR CO_2 sensor. The sensor consists of two silicon substrates. On the top substrate, the integrating cylinder is defined. On the bottom substrate, the LED and photodiodes are integrated on-chip.

After fabrication, the sensor chip is mounted on a printed circuit board (PCB) containing two TIAs for testing. The sensor works in the quasi-CW mode, which provides maximum average optical power from the LED. The response of the sensor to CO_2 concentration changes is shown in Figure 4. It can be seen that unlike the 'passive' measurement of the integrating cylinder, the normalized signal is still quite noisy, which is due to the unbalancing of the two arms. This unbalancing together with the larger optical bandwidth reaching the sensing photodiode deteriorates the limit of detection of the full sensor. The cross-sensitivity of the sensor to water vapor is investigated. Measurement results shows that there is no notable water interference effects. Further numerical simulations reveal that the transmission change due to water vapor absorption is below the limit of detection of the sensor. To study the long-term stability characteristics of the sensor, the sensor was measured for a period of five days in ambient air. It is found that the long term stability of the sensor is subject to the temperature fluctuations in the laboratory. This temperature dependence can be potentially eliminated in future iterations by

constantly monitoring the chip temperature and using look up tables created during a pre-calibration of the sensor.

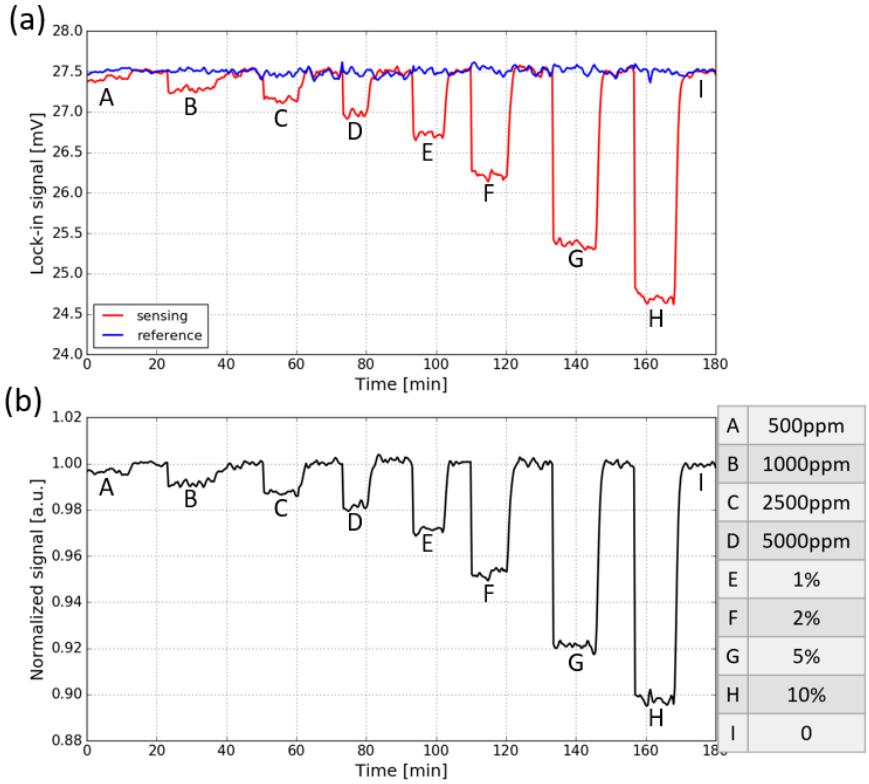

Figure 4: (a) Response of both the sensing signal and reference signal to CO_2 concentration steps. (b) Normalized transmission, obtained by dividing the sensing signal by the reference signal. The CO_2 concentration steps are listed on the right side.

1 Introduction

The goal of this work is to develop a highly integrated and low-cost non-dispersive infrared (NDIR) CO_2 gas sensor. In this chapter, the background and motivation of the work presented in this thesis are given, as well as a review of the current NDIR sensors from both academia and industry. CO_2 sensors have many applications, including mobile air conditioning systems, greenhouse farming, demand-controlled ventilation, medical diagnosis, and industrial process control. The main driver of this work is the use of CO_2 as refrigerant in mobile air conditioning (MAC) systems due to safety reasons. To prevent accidents due to the decline of human cognitive ability in case of on-board CO_2 leakage, sensors are needed for cabin CO_2 concentration monitoring and warning. The application of CO_2 sensors in smart buildings and medical diagnosis will also be elucidated. An overview of the CO_2 sensing technologies is given, with an emphasis on the NDIR technique, which is the fundamental working principle of the sensor developed in this thesis work. An overview of state-of-the-art CO_2 sensors on the market is also given. Finally, the outline of this thesis and a list of publications realized during the course of this PhD are given.

1.1 Background and motivation

Carbon dioxide(CO_2) is the fourth most abundant gas present in the earth's atmosphere, and it is a major component of the terrestrial carbon cycle. During the past 200 years, the CO_2 concentration in the ambient earth's atmosphere has increased

from ∼280ppm to ∼400ppm [1], largely due to human activities since the Industrial Revolution. CO_2 is the most significant gas responsible for global warming, accounting for 81% of the overall greenhouse gas emission, followed by Methane (10%) and Nitrous oxide(7%) [2]. Both natural and anthropogenic sources can emit CO_2. The natural sources include ocean-atmosphere exchange, plant/animal respiration, and soil respiration and decomposition. These natural sources release approximately 770 billion tons of CO_2 totally into the atmosphere per year. However, these natural sources are also huge carbon sinks, absorbing roughly the same amount of CO_2 by means of gas diffusion into the ocean, terrestrial vegetation, and land processes [3, 4], thus maintaining the global CO_2 concentration at a relatively safe level [5]. On the other hand, the amount of CO_2 emitted from anthropogenic sources is much smaller than that from natural emissions. Burning fossil fuels alone gives about 33.2 billion tons of CO_2 every year, which is about 87% of the total anthropogenic emission [6]. Although much smaller, the lack of anthropogenic carbon sink exerts pressure on nature's capability of carbon regulation, causing the CO_2 concentration to increase extensively.

CO_2 plays an important role in both nature and human society. The atmospheric CO_2 captures the radiation from the sun and keeps the temperature in a proper range thus supporting life on earth. It is also the reactant for the process of photosynthesis of both micro-organism and plants. The generated oxygen is essential for the existence and evolution of life on earth. In the context of human society, CO_2 is widely applied in the food industry either as an additive for acidity regulations or as a refrigerant for food storage and transportation due to its high volumetric cooling capacity. In the medical domain, low-concentration($\sim 0.8\%$) CO_2 is used as a stimulus to treat apnea in preterm infants and to restore O_2/CO_2 balance in blood [7].

Despite the benevolent role in the above-mentioned applications, CO_2 can be potentially detrimental. As discussed earlier, CO_2 is the most significant greenhouse gas. The elevated atmospheric CO_2 concentration during the past few hundred years has caused quite a notable impact on the environment. A recent study shows that the global average temperature has increased by approximately 1°C compared to pre-industrial levels [8]. Although seemingly a negligible increase, we have suffered severe consequences, including extreme climate events [9], increased global economic inequality [10], and reduced biodiversity [11]. Physiologically, exposure to elevated CO_2 concentrations may produce a variety of health problems. For instance, one may experience headaches and dizziness at a CO_2 concentration of 5% [12]. Even at a concentration as low as 2000ppm, prolonged exposure can cause symptoms like drowsiness and sleepiness [13]. Strict laws and regulations have been issued in order to provide a safe and comfortable occupational environment [14, 15].

To fight against global warming and mitigate the aforementioned risks, it is

critical to monitor and control the CO_2 concentration and emission at every possible site. Therefore, a low-cost, highly sensitive CO_2 sensor with minimal power consumption is required in both domestic and industrial domains. The research of CO_2 gas sensing is receiving increasing attention in both industry and academia, driven by its vast market. The European advanced CO_2 sensor market is expected to grow to 3.6 billion dollars by 2021 with a compound annual growth rate of 14.6% [16]. The CO_2 sensor market can be segmented into different domains. In the chemical industry, CO_2 is a common reactant or byproduct of many chemical processes, therefore monitoring the CO_2 concentration is essential for good process control or for CO_2 emission management [17, 18]. In the food industry, CO_2 sensors are increasingly applied in both food production and packaging sectors [19, 20]. As CO_2 is often used to modify the atmosphere in food packaging to prevent spoilage, CO_2 sensors can be applied to identify the leakage in a package. In greenhouse farming, CO_2 is one of the key ingredients for photosynthesis. To control the CO_2 concentration and thus maximize the crop yield, CO_2 sensors are indispensable elements for precision agriculture. The application of CO_2 sensors is not limited to the aforementioned domains. The following sections enumerate several key envisioned applications of the cost-effective and sensitive CO_2 sensors developed in this work.

1.1.1 Mobile air conditioning and refrigeration systems

It is estimated that there are currently over one billion vehicles on the roads and this number will hit two billion in 2035 [21]. Apart from the CO_2 emitted directly from the combustion process, greenhouse gases such as hydrofluorocarbons(HFCs) emitted from the mobile air conditioning (MAC) systems account for 30% of the total greenhouse gas emission in passenger cars [22]. The Intergovernmental Panel on Climate Change estimated that in 2015 alone, the greenhouse gas emission from the refrigerant in MAC systems is about 270 million tons of CO_2-eq [23]. Before the 1990s, chlorofluorocarbons (CFCs, commercially known as R12) were used as a refrigerant in MAC systems due to its properties such as non-flammability, low toxicity, and high chemical stability. However, its role as a refrigerant was phased out under legislative regulations due to concerns of ozone layer depletion [24]. Other substances such as perfluorocarbons (FCs) and hydrofluorocarbons (HFCs) with virtually no ozone depletion potential have been developed, and they are the most commonly used substitute refrigerants (commercially known as R134a) to date in MAC systems. Nevertheless, R134a has a relatively high global warming potential (GWP[1]), which raises concerns about its impact on climate change. The use of R134 as a refrigerant in MAC systems is currently under prohibition discussions [25]. As global warming is becoming an im-

[1] defined as the warming potential of a substance relative to CO_2 with the same mass over 100 years.

minent threat, it's important to develop a new efficient, environmentally friendly, and safe refrigerant for MAC systems. The European Union initiated a directive that R134a must be replaced by a refrigerant with GWP smaller than 150 in all new passenger cars since January 2017 [26]. Two refrigerants have been proposed as alternatives of R134a: R1234yf and CO_2, and the battle between them is not yet settled. The advantage of R1234yf is that it's compatible with the existing technology in existing air conditioning systems, therefore minimizing the cost for the development of new MAC systems. As a result, the majority of the automotive community has accepted R1234yf as the refrigerant in their MAC systems starting from 2017 [27]. CO_2 as a natural refrigerant (commercially known as R744), was extensively used before the discovery of R12 and it's now being revisited and investigated due to its excellent properties such as high volumetric cooling capacity, non-flammability, and zero ozone depletion potential [28]. As the scientific society and the general public are calling for low CO_2 emissions, CO_2 is actually the most environment-neutral refrigerant, not only in MAC systems but also in buildings and homes. It has a GWP of only 1, which is about 1400 times smaller than the currently deployed refrigerant R134a [29]. Moreover, research shows that MAC systems with CO_2 are more efficient [30], thus the energy consumption for heating and cooling can be reduced which gives a low overall CO_2 emission. The technology of R744-based MAC systems is now being developed for series production, and several German car manufacturers are planning or have committed to using CO_2 as a refrigerant in their MAC systems [31, 32]. CO_2(R744) is considered as the next generation refrigerant in MAC systems due to its superior environmental and heating performance [33–35], and extensive standards for R744-based MAC systems are being developed by institutions such as the German Association of the Automotive Industry (VDA) [36].

The transition from fluorinated gases to CO_2 is beneficial from environmental and economic aspects, yet at the same time it raises safety concerns about potential leaks from the car's onboard CO_2 tank. As the MAC compressor usually works at high pressure and the vehicle cabin is a small-volume, relatively confined environment, a trivial leakage of CO_2 onboard can lead to a surge of CO_2 concentration in the cabin. Researchers studied the CO_2 concentration level in the cabin of a B-segment car (with cabin volume $\sim 2.1m^3$). The results are shown in Figure 1.1. One can see that if the charge (CO_2 volume of 1.3 liter) is completely released within 60 seconds, the mean CO_2 concentration can spike up to 8.5% when no ventilation or re-circulation is activated. Even with maximum ventilation and re-circulation, the CO_2 concentration can go up to 6.5% in less than a minute [37]. Although CO_2 is not classified as a toxic gas, short-term exposure to relatively high (a few percents) CO_2 concentration levels can produce serious health problems [12]. For instance, one may experience headache, dizziness, and increased blood pressure when exposed to 4% CO_2 for just a few minutes. A

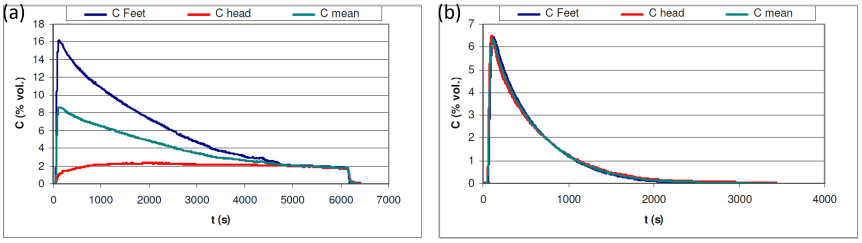

Figure 1.1: CO_2 concentration at the driver's place in the vehicle with four passengers. With a sudden leak, all the CO_2 is released in 60 seconds, the C Feet, C head and C mean denote the CO_2 concentration at the driver's feet, head and the average value, respectively. (a) With no ventilation and no re-circulation. (b) With maximum ventilation and re-circulation. Adapted from [37].

higher concentration of 7% can lead to near-unconsciousness or even complete unconsciousness in less than a minute. As a consequence, a trivial leakage of CO_2 on board can lead to fatal situations for the people onboard as well as for the traffic. As CO_2 is colorless and odorless, it is essentially not possible to detect with human senses when a sudden leak happens. Therefore, a low-cost, sensitive, and more importantly fast-responsive CO_2 sensor is needed to constantly monitor the onboard CO_2 concentration to remove the safety concerns.

1.1.2 Demand controlled ventilation

CO_2 is an important byproduct of the human metabolism, the average CO_2 concentration in human breath is about 4% and an average person breaths out approximately 1kg of CO_2 every day [38]. In an enclosed environment such as schools, workplaces, and residential buildings, human beings are the major source of CO_2 generation. If poorly ventilated, the exhaled CO_2 will accumulate and the overall indoor CO_2 concentration will increase, leading to unpleasant conditions. Figure 1.2 shows a simulation of the indoor CO_2 concentration in a typical bedroom (volume = $21m^3$) during the night for different ventilation rates [39]. One can see that when poorly ventilated (ventilation rate $< 2L/s$), the CO_2 concentration can exceed 1000ppm in the first hour, and a maximum concentration of $\sim$ 5000 ppm is reached after 8 hours when no ventilation is activated.

To provide a pleasant environment for the occupants and eliminate complaints, various countries and regions have established standards and exposure limits of CO_2 concentrations for indoor air quality (IAQ) control [40, 41]. For instance, the American Society of Heating, Refrigerating and Air-Conditioning Engineers (ASHRAE) suggested that the indoor CO_2 concentration should not exceed 1000ppm [40], which is only about three times higher than the typical outdoor concentration. These standards are rooted on numerous studies of the impact of elevated

CO_2 concentration on humans. It should be noted that CO_2 is not considered as a hazardous gas for human beings, however, intermittent- and long-term exposure to elevated CO_2 concentrations can lead to direct health risks. A review article summarizes the findings in 18 studies in various fields, including physiology, cognitive psychology, and environmental health [42]. It is shown that chronic (a few hours) exposure to a CO_2 concentration of less than 5000ppm can lead to symptoms such as a decline in cognitive abilities, bone demineralization and kidney calcification. To mitigate these health risks, constant ventilation is needed and it's essential to maintain good indoor air quality. However, this comes with the cost of increased energy consumption. In Europe, the ventilation alone consumes more than 2% of the total electricity usage, amongst the biggest consumers of indoor electricity [43]. As most of the buildings (offices, schools, residential buildings) are not always occupied during the day, the demand for ventilation also varies over time. Therefore, it is possible to achieve energy saving without compromising the occupants' well-being by using demand-controlled ventilation (DCV). Demand-controlled ventilation refers to the smart control of the ventilation rate according to the actual need. For the reasons mentioned above, the CO_2 concentration is commonly used as an indicator for indoor air quality and for DCV systems. It has been proven that energy consumption for ventilation is significantly lower when using DCV systems. A study performed in Norwegian primary schools shows that the energy consumption of a CO_2-based DCV system is reduced by 62% when compared to a constant air volume ventilation system [44]. In such DCV systems, a low-cost, sensitive (typically sub-100ppm) and low-power consumption CO_2 sensor is the key element to interrogate the indoor CO_2 concentration and adjust the ventilation rate accordingly.

1.1.3 Medical diagnosis

Another important application of CO_2 sensors is situated in the medical domain. CO_2 is a gaseous byproduct produced by the cellular metabolism in human bodies, and its concentration is strictly controlled by the carbonate buffer system in blood. The CO_2 concentration in the breath of a healthy individual is about 4% and deviations from this value may be an indicator of deterioration in the respiration system. The monitoring of the CO_2 concentration or partial pressure in the respiratory gas is called capnography. Capnography is a non-invasive, simple, and relatively low-cost technique that is commonly used in emergency medical services, intensive care units, and anaesthesiology. The measured waveform (capnogram) of the respiratory CO_2 concentration gives valuable information on the condition of the cardiorespiratory system. In the case of airway obstruction, the waveform will differentiate from that of a healthy individual. This deviation is typically used for diagnosis of cardiorespiratory diseases such as Chronic Obstructive Pulmonary

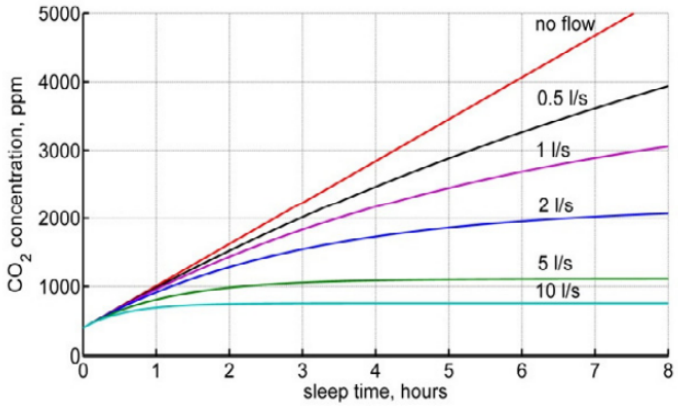

Figure 1.2: Simulation of the indoor CO_2 concentratio in a bedroom($V = 21m^3$) with one person during an 8-hour period. The initial CO_2 concentration is set to be 400ppm. When there is no ventilation, the CO_2 concentration increases linearly as a function of time. Increased ventilation rate leads to reduced steady-state CO_2 concentration and the steady state is reached faster. Adapted from [39].

Disease (COPD), asthma, and pneumonia [45]. Figure 1.3 shows a comparison of a typical capnogram for a healthy person and an asthma patient [46]. A normal capnogram consists of four successive phases: (1) expiratory upstroke marked by the segment PQ, in this phase the CO_2 concentration increases rapidly corresponding to the expiration of mixed air; (2) Alveolar plateau (segment QR), in this phase, the CO_2 concentration is relatively high due to the constant air-outflow from the alveoli in the lungs, the non-flatness of segment QR reflects the continuous diffusion of CO_2 between alveoli and the capillary blood. The CO_2 concentration at the highest point (R), typically referred to end-tidal CO_2($EtCO_2$), is an indicator of the respiratory effort; (3) inspiratory downstroke. At the end of the plateau phase, the CO_2 concentration drops quickly as the inspiration begins, noted by the segment RS; (4) respiratory baseline, in this phase, the CO_2 concentration is equal to the ambient concentration, and it's used as the baseline in capnography. In patients with asthma, the airway is obstructed and the capnogram will exhibit a decreased slope in phase 1 (segment PQ) and an increased slope in phase 2 (segment QR), as shown in Figure 1.3. This deformation of the capnogram is of particular interest because it shows a higher resistance in the airway and marks a sign for the need of administration devices for forced ventilation and perfusion. In such capnography devices, real-time monitoring of CO_2 concentrations is vital and thus choosing a CO_2 sensor with short response time and high sensitivity is essential to recover the correct time-dependent CO_2 concentration.

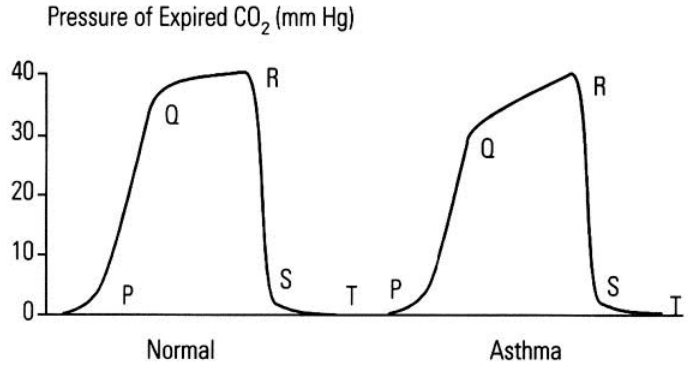

Figure 1.3: Comparison of CO_2 concentration waveforms of a normal individual and a patient with asthma. The waveform consists of four phases: (1) expiratory upstroke(segment PQ); (2)Alveolar plateau(segment QR); (3)Inspiratory downstroke(segment RS); (4)respiratory baseline(segment ST). Adapted from [46].

1.2 Overview of gas sensing technology

In this section, a review of the state-of-the-art of gas sensing technologies is given. These technologies can be categorized into optical methods and non-optical methods. As we are targeting a nearly commercial-ready gas sensing device in this work, a brief overview of the state-of-the-art of commercially available CO_2 sensors is also presented.

1.2.1 Non-optical gas sensors

In general, there are three types of non-optical gas sensors: gas chromatographic sensors, mass sensors, and electrochemical sensors. Gas chromatography is the workhorse of analytical chemistry due to its high sensitivity and high reliability. Mass sensors determine the concentration of the gas by measuring its mass with a transducer. In terms of CO_2 sensing, electrochemical sensors are the main competitors of optical sensors. In what follows, each of the three techniques is discussed with respect to its advantages and limitations.

Gas Chromatography

Gas chromatography (GC) is a common technique used in analytical chemistry to analyze the concentration of each substance in a mixed gas. It can also be used to analyze non-gaseous samples provided that the compounds can be easily vaporized and separated without decomposition. A typical GC device consists of a carrier gas injection and regulation system, a sample injection port, a column, and a detector. The carrier gas is an inert gas such as helium or nitrogen and it is used to dilute the sample gas and force it through the column. The column is typically

a few meters long and arranged in a coil, and it is enclosed in an oven chamber to maintain a uniform temperature. At the inner wall of the column, a coating is applied to adsorb or desorb the substances based on their polarity, and the adsorption/desorption rate is molecule specific. Different molecules travel at different velocities in the column and thus separation of the substances occurs. At the end of the column, a detector is used to monitor the outlet stream and various substances can be recognized based on their retention time in the column. The most commonly used detectors in GC are either flame ionization detectors (FID) or thermal conductivity detectors (TCD). In a flame ionization detector, the concentration of the substances is determined by measuring the current change induced by the ionization of the substances between the two electrodes. A thermal conductivity detector relies on the change of thermal conductivity introduced by the molecules eluted from the column. GC devices have advantages such as high sensitivity, high reliability, and they can be used to detect a wide variety of substances. Nevertheless, the cost of such devices is relatively high and their application is limited by their bulky nature. In recent years, various efforts to miniaturize chromatographic gas detectors have been made, taking advantage of the Micro-Electro-Mechanical System (MEMS) technology [47–49]. However, their applicability is fundamentally limited by the need for a relatively long capillary column and a gas pump for the carrier gas.

Mass sensor

Mass sensors measure the change of resonance frequency upon the adsorption of the gas analyte by the transducer. The resonance frequency depends on the total mass of the transducer and the adsorbed analyte. Depending on the type of transducers, mass sensors can be further categorized into three classes, namely micro-cantilevers sensors, quartz crystal micro-balance sensors, and surface acoustic wave sensors [50]. The micro-cantilevers sensor uses a free-hanging cantilever as a transducer, while in quartz crystal micro-balance sensors and surface acoustic wave sensors, quartz crystal or piezoelectric material is used. To capture the gas, a gas-adsorbing material is applied on top of the transducer and the adsorption is gas specific. During the measurement, a change in the resonance frequency, amplitude, or phase due to the added mass of the adsorbed gas can be used to extract its mass. These mass sensors can be very sensitive, surface acoustic wave sensors with a detection limit of from ppm to ppb have been reported [51]. However, the main drawback of those mass sensors is the limited selectivity as the gas adsorption depends on the specificity of the coating. Various approaches have been investigated to overcome this limitation, including using a sensor array with different selective coatings for each analyte [52], as well as utilizing pattern recognition algorithms to distinguish different analytes [50]. Even so, finding the appropriate coating material for a specific gas with superior adsorption properties is not an easy practice, and the quality of the coating can be deteriorated with the presence

of contaminants such as water vapor and dust.

Electrochemical sensors

Electrochemical sensors measure the gas concentration by measuring a change in the electrical properties such as resistance, capacitance, or electric potential induced by the adsorption of the gas. Depending on the sensing material used, they can be further divided into three sub-categories: Metal Oxide Semiconductor (MOS) sensors, polymer sensors, and Carbon Nanotube (CNT) sensors. The MOS sensor consists of a thin layer of metal oxide film and its resistance changes through the redox reaction with the target gas at elevated temperature, and this change in resistance can be correlated to the gas concentration [53]. Metal oxides such as TiO_2, ZnO, SnO_2, and WO_3 are commonly used materials and their thickness can vary from a few nanometers to tens of nanometers [50]. MOS sensors have been intensively studied and widely deployed due to their advantages such as simplicity, compactness, easy fabrication, and low cost. However, their response time is relatively long, ranging from several tens of seconds to several hundreds of seconds [4]. In addition, the high operating temperature (from 150°C to 400°C leads to higher power consumption [50]. Compared with MOS sensors, polymer-based gas sensors are more power-efficient as they can work at room temperature and the need for a micro-heater is eliminated. The working principle is quite similar to that of MOS sensors. Conducting polymers such as polyaniline (PANI) and polypyrrole (PPy) have been used for the detection of ammonia and hydrogen with excellent sensor response [54]. However, the response of such polymer-based gas sensors are temperature-dependent and they typically have a short lifetime. Carbon Nanotubes (CNT) are introduced in gas sensing applications mainly due to their unique properties such as high aspect ratio and low density, which leads to better sensitivity and shorter response times [50]. Gas sensors based on monolayer CNTs have been reported for the detection of NH_3 and NO_2, with a detection limit of 44 ppb and 262 ppb, respectively [55].

The aforementioned electrochemical sensors are advantageous because of their easy fabrication, low cost and high sensitivity to a wide range of compounds. The main issue of these sensors is the interference from unknown or unwanted molecules, as it is quite challenging to find a material with high sensitivity as well as good selectivity. The limited long-term stability is another issue that needs to be tackled.

1.2.2 Optical sensors

Optical gas sensors measure the gas concentration by means of optical absorption, emission, or scattering. Optical gas sensors offer benefits such as long-term stability, high sensitivity, and fast response. As most gases have their specific absorption lines in the optical spectrum, the interference between various gas species can be

minimized, resulting in high gas specificity. In what follows, several common optical gas sensing techniques are reviewed, including both indirect absorption methods such as refractive index sensors and photothermal/photoacoustic sensors, and direct absorption (or scattering) techniques such as tunable diode laser absorption spectroscopy (TDLAS), non-dispersive infrared spectroscopy (NDIR), and Raman spectroscopy.

1.2.2.1 Indirect methods

Refractive index sensor

Refractive index sensors are typically interferometric devices: they use the interference between two or multiple optical paths. In these refractive index sensors, an adsorbing coating is applied to capture the target gas, leading to a refractive index change of the coating layer, and this change in refractive index is correlated to the concentration of the target gas. Interferometric structures such as micro-ring resonators and Mach-Zehnder interferometers (MZI) are commonly used [56–59]. These interferometry-based sensors are quite sensitive: a tiny change in the refractive index can lead to a dramatic change in the output and a detection limit down to 5ppm has been reported for ammonia sensing [57]. In recent years, label-free refractive index sensors have also been extensively studied [60], in which a functionalization layer is applied to provide molecular binding with the analyte, and this binding gives rise to a change in refractive index that can be measured optically. Similar to the aforementioned non-optical sensors, refractive index sensors require a gas specific coating or a specific functionalization layer to achieve high selectivity.

Photothermal and photoacoustic sensors

Photothermal spectroscopy (PTS) is a highly sensitive and selective approach that relies on the indirect measurement of the optical absorption of the analyte. The absorption introduces a change in the thermal characteristics such as temperature, density, or pressure of the analyte, and this thermal response is probed and analyzed to gain information about the sample gas [61]. In PTS, the sample is illuminated with an excitation source (pump laser), the emission wavelength of which is carefully tuned to align with the characteristic absorption lines of the sample. Upon illumination, the sample is heated and the temperature change leads to a modulation of the optical properties (e.g. refractive index) of the transducer which can be probed by another optical beam (probe laser). Similar to refractive index sensors, interferometric configurations such as microring resonators and Mach-Zehnder interferometers are commonly used to retrieve this very small refractive index change [62, 63]. To further enhance the sensitivity, the output signal can be read out using schemes such as lock-in detection.

In photoacoustic spectroscopy (PAS) sensing, the working principle is quite similar to that of PTS. Instead of optically probing the temperature change due to

absorption, PAS measures the acoustic wave generated by the periodic heating and expansion of the gas. If the pump beam is chopped or modulated, the expansion produces pressure waves at the same frequency of the pump beam that can be detected using a microphone. The key advantage of this technique is that it eliminates the need for an optical detector and the generated PAS signal can be amplified by tuning the modulation frequency to the acoustic resonance frequency of the transducer. A ppb-level detection limit for trace gases has been demonstrated using a quartz tuning fork [64]. Although quite sensitive, the relatively large size and fabrication complexity limit its applicability. A few efforts have been made recently to miniaturize PAS sensors on-chip by using MEMS technology [65–67].

1.2.2.2 Direct methods

Raman spectroscopy

Raman spectroscopy is a commonly used technique to identify and quantify unknown substances in forms of gas, liquid, and solid. This technique is based on the inelastic scattering of photons (known as Raman scattering) by molecules. In this process, the incident photon may gain or lose energy due to the interaction with the vibrational or rotational modes of the molecules, causing the wavelength of the incident light to be red-shifted (Stokes) or blue-shifted (Anti-Stokes). The shift in energy provides distinctive information about the target molecules. Raman spectroscopy is considered as a complementary method to infrared spectroscopy as some substances have limited absorption in the infrared region. However, spontaneous Raman scattering is typically very weak and difficult to measure. Stimulated Raman spectroscopy (SRS) can be used to resonantly enhance the scattering process by using a second optical beam. On-chip integration of stimulated Raman spectroscopy sensors has been demonstrated using silicon nitride photonic integrated circuits [68, 69]. Furthermore, the Raman signal can be enhanced using slot waveguides or plasmonic slot waveguides by locally enhancing the optical field in the waveguide slots [70, 71]. Alternatively, metallic nanostructures such as bow-tie nano-antennas and gold nano-domes can be used [72, 73]. However, additional elements such as a light source, isolators and optical filters with an extremely high extinction ratio have to be integrated for a fully integrated Raman sensor.

Tunable Diode Laser Absorption Spectroscopy

Tunable Diode Laser Absorption Spectroscopy (TDLAS) is the most common laser-based absorption technique for identifying and quantifying certain gas species. In TDLAS, the emission wavelength of the laser is tuned over one particular characteristic absorption line of the gas, the light is absorbed by the gas and experiences an exponential decay as it propagates. The intensity change is measured by an optical detector and this change in intensity is used to determine the concentration of the gas by means of Beer-Lambert's law, which describes the relationship be-

tween the light intensity and the gas concentration. TDLAS offers advantages in terms of specificity, fast response as well as high sensitivity, and it is well suited for trace gas sensing applications. The factors determining the detection limit of the TDLAS are threefold: (1) system noise; (2) strength of the selected absorption line; (3) effective path length of the beam [74]. The system noise can be reduced by modulating the laser at a high frequency instead of using continuous-wave operation. Additionally, the detector can be cooled to reduce the noise. As most of the gases have significantly larger absorption strength in the mid-infrared (MIR) region, MIR quantum cascaded laser (QCL) can be used as the optical source. To increase the effective interaction length of the beam and the gas, optical cavities or multi-pass cells are used and they can have an effective path length of several meters. A ppb-level detection limit has been demonstrated for water vapor using a QCL operating at $7.12\mu m$, and a multi-pass cell with an effective path length of 3.5 meters [75]. Although quite sensitive, the system is quite bulky as a very long interaction length is needed to achieve low detection limits. The advances of photonic integrated circuit (PIC) technology give the potential for miniaturization of TDLAS sensors. On-chip TDLAS sensing of methane has been demonstrated at $1.65\mu m$ using an external distributed-feedback (DFB) laser and an uncooled InGaAs detector, in which a 10cm-long waveguide is integrated on-chip, yielding a detection limit of 100ppm [76]. Furthermore, The heterogeneous integration of single-mode short-wave infrared ($2\mu m$ wavelength range) lasers on silicon photonics platform have also been reported and can be used in integrated TDLAS gas sensing [77].

Non-Dispersive Infrared Spectroscopy

As the name suggests, Non-Dispersive Infrared Spectroscopy (NDIR) is a non-dispersive technique, namely no dispersive elements (prisms, diffraction gratings, etc.) are required to interrogate the content of the spectrum in order to determine the gas concentration. The working principle of NDIR sensors is quite similar with that of TDLAS sensors, they both rely on direct light absorption of the target gas. However, instead of tuning the emission wavelength of the laser across a single absorption line, NDIR sensors use a broadband light source where the emission spectrum covers a 'group' of absorption lines. Therefore low-cost light sources such as light emitting diodes (LEDs) or thermal emitters such as micro-light bulbs can be used. The infrared light emitted by the light source is directed through the gas chamber, which allows the light to be absorbed by the target gas, and the change in light intensity is measured by the detector. NDIR sensors typically consist of two channels: the sensing channel and the reference channel. In the sensing channel, an optical filter with passband overlapping with the absorption region of the gas of interest is used, while the optical filter in the reference channel is chosen such that its passband does not overlap with the absorption spectrum of any commonly encountered gases. The NDIR technique has been used for quantita-

tive determination of a variety of gas species such as carbon monoxide, methane, and ammonia [78]. Depending on the type of optical sources, detectors as well as the interaction length, the detection limit ranges from a few ppm to hundreds of ppms. Moreover, the NDIR technique is particularly suited for CO_2 sensing, as CO_2 sensing is notoriously difficult with non-optical methods and NDIR opens a new path due to the significant absorption strength of CO_2 in the MIR region. NDIR CO_2 sensors rely on the very high absorption coefficient that spans over $500cm^{-1}$ in the mid-infrared wavelength range around $4.26\mu m$, which is two orders of magnitude higher than that of the typical trace gases. Due to this high absorption coefficient, the requirement on the interaction length is relaxed and an optical path length of a few centimeters is sufficient to detect small changes in CO_2 concentration. Furthermore, the choice of the source and the detector is less demanding: simple broadband optical sources such as micro-light bulbs and LEDs can be used, and on the detector side, low-cost devices such as thermopile detectors or pyroelectric detectors are sufficient. Due to the aforementioned advantages, NDIR CO_2 sensors are commercially successful: it is estimated that about 83% of the total advanced CO_2 sensors are based on the NDIR technique [16].

However, NDIR sensors tend to be bulky because to achieve ppm level detection a long (typically several cm) interaction length is required. The cost of current NDIR sensors is also high as they are typically based on discrete co-assembled optical elements, which limits their application in price and size sensitive markets. Intense efforts have been made to miniaturize NDIR sensors: integrated optical sources such as micro-heaters based on CMOS and MEMS technologies have been developed [79, 80], LED-photodiode opto-pairs have also been used [81], giving the potential for a highly miniaturized NDIR gas sensor. To increase the gas-light interaction length while maintaining the compactness of the sensor, the design of the gas cell can be optimized by using either a multi-pass cell [82] or an optical cavity with various shapes [83–85]. A recent study demonstrated an ultra-long path length of 25cm on a chip area of less than $10mm^2$, using highly reflective mirrors formed by photonic crystals on a silicon-on-insulator (SOI) platform [86]. The advantage of this approach is that it uses CMOS-compatible fabrication technology, giving it the potential for mass production with extremely low cost. Apart from these techniques to increase the interaction length, pre-concentrator coatings can be employed to effectively 'amplify' the gas concentration in the vicinity of the optical field, thus the required optical path length can be reduced [87]. The relatively simple structure and the use of low-cost optical sources and detectors enable multi-gas detection. By choosing multiple optical filters with different passbands, simultaneous measurement of various gas species can be achieved with one single NDIR sensor [83, 88]. Although convenient and straightforward, the need for optical filters to select the desired spectrum from the broadband source hinders the miniaturization of NDIR sensors. Typical NDIR sensors use filters that are

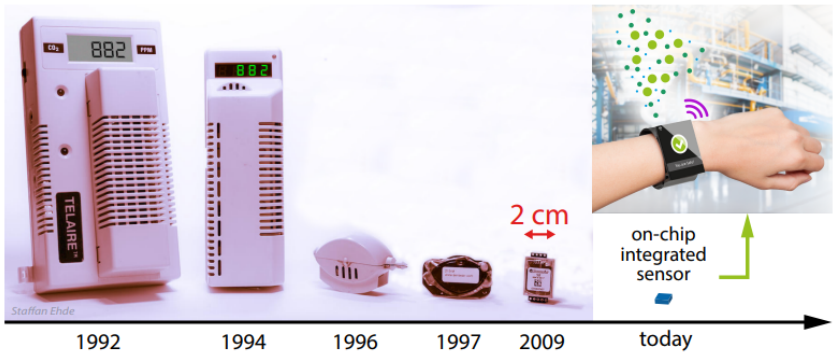

Figure 1.4: Evolution of NDIR gas sensors over the past three decades, and the vision for a fully integrated on-chip NDIR gas sensor in the future. Adapted from [90].

directly coated onto a packaged detector (eg. in a TO9-can), which is not compatible with on-chip sensors. The need for optical filters can be eliminated by using narrow-band optical sources or detectors based on meta-material emitters or absorbers, in which the emission or detection spectrum can be tuned to align with the absorption band of the gas of interest. This tuning is achieved by engineering the shape and period of the nano-structure on the emitter or absorber [79]. These meta-material based emitters can be very efficient, with an emissivity almost equal to unity. The full width at half maximum (FWHM) of the emission spectrum is typically on the order of 300nm, which is sufficient to cover the absorption band of CO_2 around $4.26\mu m$ without introducing cross-sensitivity by other common gases. Using such an emitter together with a meta-material based thermopile detector, a filter-free NDIR sensor is demonstrated with a multi-reflection cell ($5.7 \times 5.7 \times 4.5mm^3$). The cell gives an equivalent path length of around 5cm and a sensitivity of $23ppm/\sqrt{Hz}$ is achieved [89]. From the commercial point of view, the size of the commercially available NDIR gas sensors has been dramatically reduced over the last decades [90], as illustrated in Figure 1.4. This size reduction is attributed to the aforementioned reasons, i.e., the use of optical sources such as MEMS-based micro-heaters and LEDs, as well as the miniaturization of the gas cell. However, the state-of-the-art commercial NDIR sensors are still a few centimeters big, limiting their applications such as in portable devices. The development of a highly integrated, cost- and energy-efficient NDIR gas sensor can not only extend its current applications in price- and size sensitive markets, but also introduce new applications in portable devices such as smartphones.

1.3 State-of-the-art NDIR CO_2 sensors on the market

As mentioned previously, NDIR CO_2 sensors account for the largest share in the gas sensor market. The NDIR CO_2 sensor market is mainly dominated by a few companies such as Gas Sensing Solutions, Senseair, Sensirion, and each company has its own story of advancing the performance of the sensors and reducing the cost and size. Table 1.1 lists a few state-of-the-art commercial NDIR CO_2 sensors from these manufacturers together with their major specifications. It should be noted that the purpose of the 'price' column[2] is to offer a preliminary apprehension of the costs of the sensors, as the price can vary geographically and over time and it is also dependent on other factors such as purchase quantity. The maximum detectable CO_2 concentration of these sensors spans from a few thousands of ppm to a few percents and it is suitable for most common applications such as air quality monitoring and greenhouse farming. The detection limit is typically around 50 ppm, which is sufficient for most of the applications. To achieve such a low detection limit, a path length of a few centimeters is required. These sensors either use a single-pass cell and curl it to certain shapes or use cavities with specific shapes (eg. an ellipse) to attain the required path length on a small area. Nevertheless the size of these sensors is still on the order of $\sim 3cm$. Consequently, the response time of the sensors is typically long ($\sim 30s$ or longer) as most of the sensors are based on gas diffusion. The response time can be shortened by pumping the gas into the gas cell, leading to a fast response of the sensor. For instance, the response time of the sensor K30 (from SenseAir) is only 2 seconds at $0.5/l$ gas flow rate, which is 10 times shorter than that of its diffusion counterpart. Another important concern is the power consumption of the sensor, which is the summation of the power dissipated by the electronic circuits and the power consumption of the optical source and detector. In general, LED and photodiode opto-pairs are more energy-efficient than their thermal counterparts; the typical power consumption of an LED is tens of mW. The power consumption is also related to the measurement rate of the sensor, as a continuous measurement is not required in some cases and the power consumption can be reduced by increasing the measurement interval. To avoid sensor blindness by contaminants such as dust particles, a diffusion membrane with microscopic pores is applied to filter out dust particles from the airflow.

[2] From https://www.co2meter.com/, accessed 30-May-2020

Manufacturer	Product	Detection range	Detection limit	Response time (s)	Warm up time (s)	Dimensions ($L \times W, mm^2$)	Power consumption (mW)	Price (€)
Gas sensing solutions	 GC-0034	0-1%	$\pm$45ppm + 3% of reading	30	3.3	31×20	75	114
SenseAir	 SE-0117	0-0.5%	$\pm$30ppm + 3% of reading	20	60	57×51	110	84
Sensirion	 SCD30	0-4%	$\pm$30ppm + 3% of reading	20	–	35×23	48	–
Sensera	 SG111A	0-0.5%	$\pm$50ppm + 5% of reading	30	120	32×20	89	–
Amphenol	 AMP-0002	0-0.2%	$\pm$30ppm + 3% of reading	180	120	30×15.6	125	97
Figaro	 FG-010	0-0.5%	$\pm$50ppm + 3% of reading	120	–	32×17	50	105

Table 1.1: Overview of state-of-the-art commercial NDIR CO_2 sensors from several major manufacturers.

1.4 Thesis objective and outline

This doctoral research is mainly driven by the increasing interest and the vast market for better gas sensing solutions, as well as by the technological opportunities offered by the mature silicon technology, which allow for the potential mass production of gas sensors with extremely low cost. As discussed earlier in the introduction, there is a growing need for low-cost, sensitive optical gas sensors. The main driver for this work is the gradual ban of the F-gas-based refrigerant in MAC systems enacted by the European Union. CO_2 has been proposed as an environment-friendly refrigerant due to its smaller GWP. To avoid possible incidents and remove the safety concern due to on-board CO_2 leakage, sensors are needed to monitor the CO_2 concentrations in the cabin. Fast response time (a few seconds) of the sensor is of paramount importance, while detection limit down to ppm-level is less critical. Another envisioned application of the sensor developed in this work is in indoor air quality monitoring for demand-controlled ventilation systems. In this scenario a highly-sensitive CO_2 sensor is required, while the response time of the sensor is less important. Such a CO_2 sensor can also contribute to a larger sensor network for internet of things (IoT) systems. In both cases, the cost and the energy consumption of the sensor should be low. As mentioned previously in the introduction, the NDIR technique gives the potential for highly miniaturized, low-cost, and highly sensitive gas sensors with low power consumption. In this thesis we aim at such a fully integrated NDIR CO_2 optical sensor by using silicon technologies. The remaining part of this thesis will address the challenges for the implementation of the sensor, which includes: (1) how to achieve a relatively long interaction length on a limited chip area to reach the desired detection limit; (2) how can we integrate the optical source and detector on the chip in a low-cost way; (3) how to optimize the overall sensor performance; (4) what is the future path to industrialize the sensor developed in this work.

The scope of this research extends from fundamental studies on gas sensing to experimental demonstrations of a sensor prototype with practically relevant specifications. In Chapter 2, a brief introduction to silicon photonics and MEMS technologies is given, with an emphasis on their extension to the mid-infrared wavelength range. Infrared absorption spectroscopy, more particularly non-dispersive infrared (NDIR) spectroscopy is explained in more depth, and one will see the numerous benefits of CO_2 sensing in the mid-infrared wavelength range. Relevant concepts behind absorption spectroscopy such as molecular energy levels and absorption line broadening mechanisms are also discussed.

In Chapter 3, three different configurations are proposed to realize an integrated on-chip gas sensor. These sensor configurations are based on multi-slot suspended silicon waveguides, hollow metallic waveguides and a metallic integrating cylinder. A high-level comprehensive study of the three sensor structures

is given, simulations are performed to investigate the waveguide losses, power budget and achievable detection limit for the three candidates. Based on this analysis, the optimal configuration is determined. One will see that the sensor based on a metallic integrating cylinder is the most promising approach in terms of its footprint, sensitivity, and potential for future low-cost fabrication.

With the optimal configuration of the sensor fixed, Chapter 4 provides a detailed investigation of the 'gas cell' part of the sensor, namely the metallic integrating cylinder. Such an integrating cylinder can be considered as a 2D version of an integrating sphere, implemented on silicon. Theoretical calculations of the integrating cylinder are given, simulation results on the loss, effective path length, and sensitivity are presented, as well as the response time of the sensor. The fabrication process of the sensor is discussed in detail. The details of the dedicated experimental setup to characterize the fabricated sensor are given. In this chapter an external optical source and external detectors are used. The experimental results on CO_2 sensing are presented.

Chapter 5 is devoted to the integration of the optical source and detector with the integrating cylinder. A mid-infrared light-emitting diode (LED) is chosen as the light source, due to its relatively narrow emission spectrum compared to a thermal emitter, such that the need for optical filters can be eliminated without introducing notable cross-sensitivity by other gases. Moreover, LED light sources have the benefits of low cost, ease of integration, and low power consumption. Mid-infrared photodiodes are used as detectors mainly due to their high sensitivity compared with thermal detectors such as thermopile detectors and bolometers. Optical simulations regarding the coupling efficiencies from the LED to the integrating cylinder and from the integrating cylinder to the photodiodes are performed. The process flow of the integration of the LED and photodiodes is also discussed. The design of the transimpedence amplifiers (TIA) to amplify the output signal is also presented. Eventually, the fully integrated optical sensor is characterized and the results are discussed.

Overall conclusions and future perspectives are given in Chapter 6.

1.5 List of publications

1.5.1 Patent

1. G. Roelkens, Joris Roels, R. Baets, Wouter Leten, **X. Jia**, "Gas sensor device and method of manufacturing the same", (patent pending)

1.5.2 Publications in international journals

1. **X. Jia**, J. Roels, R. Baets, G. Roelkens, On-Chip Non-Dispersive Infrared CO2 Sensor Based On an Integrating Cylinder, Sensors, 19(19), p.1-14 doi:10.3390/s19194260 (2019)

2. **X. Jia**, J. Roels, R. Baets, G. Roelkens, A Miniaturised, Fully Integrated On-Chip NDIR CO2 Sensor, under preparation

1.5.3 Publications in international conferences

1. **X. Jia**, G. Roelkens, R. Baets, Roels Joris, A Miniaturized Non-Dispersive Infrared CO2 Sensor Based On a 2D Integrating Cylinder , Optical Sensors and Sensing congress, United States, p.paper STu3C.5 doi:10.1364/sensors.2019.stu3c.5 (2019)

2. **X. Jia**, Joris Roels, R. Baets, G. Roelkens, On-Chip Integrating Cylinder Cavity for Ultra-Compact NDIR CO2 Sensors, Annual Symposium of the IEEE Photonics Society Benelux Chapter, (2019)

3. G. Roelkens, R. Wang, A. Vasiliev, S. Radosavljevic, **X. Jia**, N. Teigell Beneitez, B. Haq, F. Pavanello, M. Muneeb, G. Lepage, P. Verheyen, J. Van Campenhout, S. Sprengel, G. Boehm, M.C. Amann, I. Simonyte, K. Vizbaras, A.Vizbaras, R. Baets, III-V/Si photonic integrated circuits for the mid-infrared, IEEE International Conference on Group IV Photonics (invited), Mexico, p.FE1 doi:10.1109/group4.2018.8478755 (2018)

References

[1] Rajendra K Pachauri and Andy Reisinger. *IPCC fourth assessment report*. IPCC, Geneva, 2007, 2007.

[2] Leif Hockstad and L Hanel. *Inventory of US greenhouse gas emissions and sinks*. Technical report, Environmental System Science Data Infrastructure for a Virtual Ecosystem, 2018.

[3] US DOE. *Carbon Cycling and Biosequestration: Integrating Biology and Climate Through Systems Science*. In Report from the March 2008 workshop, Doe/SC, volume 108, 2008.

[4] S Joshi. *Tailored nanostructures for CO2 gas sensing applications*. 2017.

[5] Surabi Menon, Kenneth L Denman, Guy Brasseur, Amnat Chidthaisong, Philippe Ciais, Peter M Cox, Robert E Dickinson, Didier Hauglustaine, Christoph Heinze, Elisabeth Holland, et al. *Couplings between changes in the climate system and biogeochemistry*. Technical report, Lawrence Berkeley National Lab.(LBNL), Berkeley, CA (United States), 2007.

[6] Corinne Le Quéré, Robert J Andres, T Boden, Thomas Conway, Richard A Houghton, Joanna I House, Gregg Marland, Glen Philip Peters, Guido Van der Werf, Anders Ahlström, et al. *The global carbon budget 1959–2011*. Earth System Science Data Discussions, 5(2):1107–1157, 2012.

[7] Saif Al-Saif, Ruben Alvaro, Juri Manfreda, Kim Kwiatkowski, Don Cates, Mansour Qurashi, and Henrique Rigatto. *A randomized controlled trial of theophylline versus CO2 inhalation for treating apnea of prematurity*. The Journal of pediatrics, 153(4):513–518, 2008.

[8] Plenary Julia First. *Global Warming of 1.5 C An IPCC Special Report on the Impacts of Global Warming of 1.5 C Above Pre-Industrial Levels and Related Global Greenhouse Gas Emission Pathways, in the Context of Strengthening the Global Response to the Threat of Climate Change*. Sustainable Development, and Efforts to Eradicate Poverty. https://www. ipcc. ch/sr15/. Accessed, 1, 2019.

[9] Noah S Diffenbaugh, Deepti Singh, Justin S Mankin, Daniel E Horton, Daniel L Swain, Danielle Touma, Allison Charland, Yunjie Liu, Matz Haugen, Michael Tsiang, et al. *Quantifying the influence of global warming on unprecedented extreme climate events*. Proceedings of the National Academy of Sciences, 114(19):4881–4886, 2017.

[10] Noah S Diffenbaugh and Marshall Burke. *Global warming has increased global economic inequality*. Proceedings of the National Academy of Sciences, 116(20):9808–9813, 2019.

[11] Steven Footitt, Ziyue Huang, Hülya Ölcer-Footitt, Heather Clay, and WE Finch-Savage. *The impact of global warming on germination and seedling emergence in Alliaria petiolata, a woodland species with dormancy loss dependent on low temperature*. Plant Biology, 20(4):682–690, 2018.

[12] Jennifer Law, Sharmi Watkins, David Alexander, et al. *In-flight carbon dioxide exposures and related symptoms: Association, susceptibility, and operational implications*. NASA Technical Paper, 216126:2010, 2010.

[13] Wisconsin Department of Health Services. *CO2 Hazards*. https://www.dhs.wisconsin.gov/chemical/carbondioxide.htm, 2019. Accessed 12 May 2020.

[14] Occupational Safety and Health Administration. *Permissible Exposure Limits*. https://www.osha.gov/dsg/annotated-pels/tablez-1.html, 2017. Accessed 06 June 2020.

[15] Health and Safety Executive. *EH40/2005 Workplace exposure limits*. 2018.

[16] Market Research Future. *Europe Advanced CO2 Sensor Market Analysis—Global Forecast 2016 to 2022*. https://www.marketresearchfuture.com/reports/europe-advanced-co2-sensor-market-2574, 2017. Accessed 15 May 2020.

[17] Nadeem M Khalfe, Kumar Sandip Lahiri, and Kumar Sunil Sawke. *Soft sensor for better control of carbon dioxide removal process in ethylene glycol plant*. Chemical Industry and Chemical Engineering Quarterly, 17(1):17–24, 2011.

[18] Hans-Joachim Leimkühler. *Managing CO2 emissions in the chemical industry*. John Wiley & Sons, 2010.

[19] Gerald Gerlach, Ulrich Guth, and Wolfram Oelßner. *Carbon Dioxide Sensing: Fundamentals, Principles, and Applications*. John Wiley & Sons, 2019.

[20] Suresh Neethirajan, DS Jayas, and Shashikant Sadistap. *Carbon dioxide (CO 2) sensors for the agri-food industry—a review*. Food and Bioprocess Technology, 2(2):115–121, 2009.

[21] Green Car Reports. *1.2 Billion Vehicles On World's Roads Now, 2 Billion by 2023: Report*. https://www.greencarreports.com/news/$1093560_1 - 2 - billion - vehicles - on - worlds - roads - now - 2 - billion - by - 2035 - report$, 2014. $Accessed 10 June 2020$.

[22] ONU Environnement, L KUIJPERS, and D VERDONIK. *Task Force Decision XX/8 report: assessment of alternatives to HCFCs and HFCs and update of the TEAP 2005 supplement report data.* Unep (united nations environment programme), ozone secretariat-Kenya, 2009.

[23] Intergovernmental Panel on Climate Change and Bert Metz. *IPCC/TEAP special report on safeguarding the ozone layer and the global climate system: Issues related to hydrofluorocarbons and perfluorocarbons*. Cambridge University Press, 2005.

[24] Montreal Protocol. *Montreal protocol on substances that deplete the ozone layer*. Washington, DC: US Government Printing Office, 26:128–136, 1987.

[25] M Schulz and D Kourkoulas. *Regulation (EU) No 517/2014 of The European Parliament and of the council of 16 April 2014 on fluorinated greenhouse gases and repealing Regulation (EC) No 842/2006*. Off. J. Eur. Union, 2014(517):L150, 2014.

[26] E Union. *Directive 2006/40/EC of the European Parliament and of the Council of 17 May 2006 relating to emissions from air-conditioning systems in motor vehicles and Amending Council Directive 70/156/EEC*. Off J Eur Union, 1, 2006.

[27] Treehugger. *Honeywell Defends R1234yf Refrigerant Against Daimler*. https://www.treehugger.com/honeywell-defends-ryf-refrigerant-against-daimler-4854288, 2018. Accessed 21 December 2020.

[28] Petter Nekså, Harald Taxt Walnum, and Armin Hafner. *CO2-a refrigerant from the past with prospects of being one of the main refrigerants in the future*. In 9th IIR Gustav Lorentzen conference, pages 2–14, 2010.

[29] Alberto Cavallini and Claudio Zilio. *Carbon dioxide as a natural refrigerant*. International Journal of Low-Carbon Technologies, 2(3):225–249, 2007.

[30] G Hoffmann and W Plehn. *Natural refrigerants for mobile air conditioning in passenger cars*. Dessau: German Federal Environment Agency, Office GFEAP, 2010.

[31] R744.com. *Daimler employs safety system for R1234yf MAC*. https://r744.com/articles/9140/daimler-employs-safety-system-for-r1234yf-mac, 2019. Accessed 21 December 2020.

[32] R744.com. *VW to roll out CO2 MAC in new electric car series*. http://r744.com/articles/8495/vw-to-roll-out-co2-mac-in-new-electric-car-series, 2018. Accessed 21 December 2020.

[33] Dong Junqi, Wang Yibiao, Jia Shiwei, Zhang Xianhui, and Huang Linjie. *Experimental study of R744 heat pump system for electric vehicle application*. Applied Thermal Engineering, 183:116191.

[34] Dandong Wang, Zhenyu Zhang, Binbin Yu, Xinnan Wang, Junye Shi, and Jiangping Chen. *Experimental research on charge determination and accumulator behavior in trans-critical CO2 mobile air-conditioning system*. Energy, 183:106–115, 2019.

[35] R744.com. *Sanden: Electric cars will drive CO2 MAC uptake*. http://www.r744.com/articles/8702/sanden-ev-cars-will-drive-co2-mac-uptake, 2018. Accessed 21 December 2020.

[36] German Association of the Automotive Industry. *Air-conditioning systems and refrigerants*. https://www.vda.de/en/topics/environment-and-climate/development-air-conditioning-systems-and-coolants.html, 2019. Accessed 21 December 2020.

[37] C Malvicino, R Seccardini, M Markowitz, K Schuermanns, A Bergami, C Arnaud, R Haller, C Petitjean, C Strupp, N Lemke, et al. *B-cool project-ford ka and fiat panda r-744 mac systems*. Technical report, SAE Technical Paper, 2009.

[38] Science Focus. *How much does human breathing contribute to climate change?* https://www.sciencefocus.com/planet-earth/how-much-does-human-breathing-contribute-to-climate-change/, 2015. Accessed 22 May 2020.

[39] Piotr Batog and Marek Badura. *Dynamic of changes in carbon dioxide concentration in bedrooms*. Procedia Engineering, 57:175–182, 2013.

[40] ANSI ASHRAE. *ASHRAE Standard 62.1-2016, Ventilation for Acceptable Indoor Air Quality*. American Society of Heating, Refrigerating, and Air-Conditioning Engineers, Inc.: Atlanta, GA, 2016.

[41] HongKong Environmental Protection Department. *Indoor Air Quality*. https://www.epd.gov.hk/epd/english/environmentinhk/air/indoorairquality/airindoorair.html, 2019. Accessed 23 May 2020.

[42] Tyler A Jacobson, Jasdeep S Kler, Michael T Hernke, Rudolf K Braun, Keith C Meyer, and William E Funk. *Direct human health risks of increased atmospheric carbon dioxide*. Nature Sustainability, 2(8):691–701, 2019.

[43] EC Directive. *Directive 2009/125/EC of the European Parliament and of the Council of 21 October 2009, establishing a framework for the setting of ecodesign requirements for energyrelated products (recast)*. Official Journal of the European Communities, 2009.

[44] Mads Mysen, Sveinung Berntsen, Per Nafstad, and Peter G Schild. *Occupancy density and benefits of demand-controlled ventilation in Norwegian primary schools*. Energy and Buildings, 37(12):1234–1240, 2005.

[45] OM PrakaSh SIngh and MB MalarvIlI. *Review of Infrared Carbon-Dioxide Sensors and Capnogram Features for Developing Asthma-Monitoring Device.* Journal of Clinical & Diagnostic Research, 12(10), 2018.

[46] Michael Yaron, Paul Padyk, Molly Hutsinpiller, and Charles B Cairns. *Utility of the expiratory capnogram in the assessment of bronchospasm*. Annals of emergency medicine, 28(4):403–407, 1996.

[47] Apoorva Garg, Muhammad Akbar, Eric Vejerano, Shree Narayanan, Leyla Nazhandali, Linsey C Marr, and Masoud Agah. *Zebra GC: A mini gas chromatography system for trace-level determination of hazardous air pollutants*. Sensors and Actuators B: Chemical, 212:145–154, 2015.

[48] Stefano Zampolli, Ivan Elmi, Gian Carlo Cardinali, Luca Masini, Filippo Bonafè, and Federico Zardi. *Compact-GC platform: A flexible system integration strategy for a completely microsystems-based gas-chromatograph*. Sensors and Actuators B: Chemical, 305:127444, 2020.

[49] Imadeddine Azzouz and Khaldoun Bachari. *MEMS devices for miniaturized gas chromatography*. MEMS sensors—design and application, pages 149–169, 2018.

[50] Haleh Nazemi, Aashish Joseph, Jaewoo Park, and Arezoo Emadi. *Advanced micro-and nano-gas sensor technology: A review*. Sensors, 19(6):1285, 2019.

[51] DS Ballantine Jr, Robert M White, Stephen J Martin, Antonio J Ricco, ET Zellers, GC Frye, and H Wohltjen. *Acoustic wave sensors: theory, design and physicochemical applications*. Elsevier, 1996.

[52] Massimiliano Benetti, Domenico Cannatà, Enrico Verona, Alexandra Palla Papavlu, Valentina Carmen Dinca, Thomas Lippert, Maria Dinescu, and Fabio Di Pietrantonio. *Highly selective surface acoustic wave e-nose implemented by laser direct writing*. Sensors and Actuators B: Chemical, 283:154–162, 2019.

[53] Maurizio Donarelli and Luca Ottaviano. *2D materials for gas sensing applications: A review on graphene oxide, MoS2, WS2 and phosphorene*. Sensors, 18(11):3638, 2018.

[54] Seon Joo Park, Chul Soon Park, and Hyeonseok Yoon. *Chemo-electrical gas sensors based on conducting polymer hybrids*. Polymers, 9(5):155, 2017.

[55] Irina V Zaporotskova, Natalia P Boroznina, Yuri N Parkhomenko, and Lev V Kozhitov. *Carbon nanotubes: Sensor properties. A review*. Modern Electronic Materials, 2(4):95–105, 2016.

[56] Nebiyu A Yebo, Petra Lommens, Zeger Hens, and Roel Baets. *An integrated optic ethanol vapor sensor based on a silicon-on-insulator microring resonator coated with a porous ZnO film*. Optics Express, 18(11):11859–11866, 2010.

[57] Nebiyu A Yebo, Sreeprasanth Pulinthanathu Sree, Elisabeth Levrau, Christophe Detavernier, Zeger Hens, Johan A Martens, and Roel Baets. *Selective and reversible ammonia gas detection with nanoporous film functionalized silicon photonic micro-ring resonator*. Optics express, 20(11):11855–11862, 2012.

[58] Raghi S El Shamy, Mohamed A Swillam, and Diaa A Khalil. *Mid Infrared Integrated MZI Gas Sensor Using Suspended Silicon Waveguide*. Journal of Lightwave Technology, 37(17):4394–4400, 2019.

[59] Giuseppe Antonacci, Jeroen Goyvaerts, Haolan Zhao, Bettina Baumgartner, Bernhard Lendl, and Roel Baets. *Ultra-sensitive refractive index gas sensor with functionalized silicon nitride photonic circuits*. arXiv preprint arXiv:2004.04260, 2020.

[60] Enxiao Luan, Hossam Shoman, Daniel M Ratner, Karen C Cheung, and Lukas Chrostowski. *Silicon photonic biosensors using label-free detection*. Sensors, 18(10):3519, 2018.

[61] Karol Krzempek. *A review of photothermal detection techniques for gas sensing applications*. Applied Sciences, 9(14):2826, 2019.

[62] Anton Vasiliev, Aditya Malik, Muhammad Muneeb, Bart Kuyken, Roel Baets, and Gunther Roelkens. *On-chip mid-infrared photothermal spectroscopy using suspended silicon-on-insulator microring resonators*. ACS Sensors, 1(11):1301–1307, 2016.

[63] Yan Zuo, Yerun Gao, Shiyu Qin, Zhenye Wang, De Zhou, Zhen Li, Yu Yu, Ming Shao, and Xinliang Zhang. *Broadband multi-wavelength optical sensing based on photothermal effect of 2D MXene films*. Nanophotonics, 2019.

[64] Vincenzo Spagnolo, Pietro Patimisco, Simone Borri, Gaetano Scamarcio, Bruce E Bernacki, and Jason Kriesel. *Part-per-trillion level SF 6 detection using a quartz enhanced photoacoustic spectroscopy-based sensor with single-mode fiber-coupled quantum cascade laser excitation*. Optics letters, 37(21):4461–4463, 2012.

[65] JG Coutard, A Berthelot, A Glière, H Lhermet, B Scherer, T Strahl, A Teulle, and T Verdot. *Micro PA detector: pushing the limits of mid IR photoacoustic spectroscopy integrated on silicon*. In Silicon Photonics XV, volume 11285, page 1128513. International Society for Optics and Photonics, 2020.

[66] M Verstuyft, E Akiki, B Walter, M Faucher, M Vanwolleghem, and B Kuyken. *An Integrated Photoacoustic Terahertz Gas Sensor*. In 2019 44th International Conference on Infrared, Millimeter, and Terahertz Waves (IRMMW-THz), pages 1–2. IEEE, 2019.

[67] Alain Gliere, Pierre Barritault, Audrey Berthelot, Christophe Constancias, J-G Coutard, B Desloges, L Duraffourg, J-M Fedeli, Marine Garcia, Olivier Lartigue, et al. *Downsizing and Silicon Integration of Photoacoustic Gas Cells*. International Journal of Thermophysics, 41(2):16, 2020.

[68] Haolan Zhao, Stéphane Clemmen, Ali Raza, and Roel Baets. *Stimulated Raman spectroscopy of analytes evanescently probed by a silicon nitride photonic integrated waveguide*. Optics letters, 43(6):1403–1406, 2018.

[69] Haolan Zhao, Bettina Baumgartner, Ali Raza, Andre Skirtach, Bernhard Lendl, and Roel Baets. *Multiplex volatile organic compound Raman sensing with nanophotonic slot waveguides functionalized with a mesoporous enrichment layer*. Optics Letters, 45(2):447–450, 2020.

[70] Ashim Dhakal, Pieter C Wuytens, Frédéric Peyskens, Karolien Jans, Nicolas Le Thomas, and Roel Baets. *Nanophotonic waveguide enhanced Raman spectroscopy of biological submonolayers*. Acs Photonics, 3(11):2141–2149, 2016.

[71] Ali Raza, Stéphane Clemmen, Pieter Wuytens, Muhammad Muneeb, Michiel Van Daele, Jolien Dendooven, Christophe Detavernier, Andre Skirtach, and Roel Baets. *ALD assisted nanoplasmonic slot waveguide for on-chip enhanced Raman spectroscopy*. APL Photonics, 3(11):116105, 2018.

[72] Pieter C Wuytens, Hans Demol, Nina Turk, Kris Gevaert, Andre G Skirtach, Mohamed Lamkanfi, and Roel Baets. *Gold nanodome SERS platform for label-free detection of protease activity*. Faraday discussions, 205:345–361, 2017.

[73] Frédéric Peyskens, Pieter Wuytens, Ali Raza, Pol Van Dorpe, and Roel Baets. *Waveguide excitation and collection of surface-enhanced Raman scattering from a single plasmonic antenna*. Nanophotonics, 7(7):1299–1306, 2018.

[74] Maximilian Lackner. *Tunable diode laser absorption spectroscopy (TDLAS) in the process industries–a review*. Reviews in Chemical Engineering, 23(2):65–147, 2007.

[75] WE Wang, APM Michel, L Wang, T Tsai, ML Baeck, James A Smith, and Gerard Wysocki. *A quantum cascade laser-based water vapor isotope analyzer for environmental monitoring*. Review of Scientific Instruments, 85(9):093103, 2014.

[76] Lionel Tombez, EJ Zhang, JS Orcutt, Swetha Kamlapurkar, and WMJ Green. *Methane absorption spectroscopy on a silicon photonic chip*. Optica, 4(11):1322–1325, 2017.

[77] Ruijun Wang, Anton Vasiliev, Muhammad Muneeb, Aditya Malik, Stephan Sprengel, Gerhard Boehm, Markus-Christian Amann, Ieva Šimonytė, Augustinas Vizbaras, Kristijonas Vizbaras, et al. *III–V-on-silicon photonic integrated circuits for spectroscopic sensing in the 2–4 μm wavelength range*. Sensors, 17(8):1788, 2017.

[78] Daniel Popa and Florin Udrea. *Towards Integrated Mid-Infrared Gas Sensors*. Sensors, 19(9):2076, 2019.

[79] Alexander Lochbaum, Yuriy Fedoryshyn, Alexander Dorodnyy, Ueli Koch, Christian Hafner, and Juerg Leuthold. *On-chip narrowband thermal emitter for mid-IR optical gas sensing*. ACS photonics, 4(6):1371–1380, 2017.

[80] Andrea De Luca, SZ Ali, and Florin Udrea. *On the reproducibility of CMOS plasmonic mid-IR thermal emitters*. In 2017 International Semiconductor Conference (CAS), pages 101–104. IEEE, 2017.

[81] Desmond Gibson and Calum MacGregor. *A novel solid state non-dispersive infrared CO2 gas sensor compatible with wireless and portable deployment*. Sensors, 13(6):7079–7103, 2013.

[82] Ke Chen, Bo Zhang, Shuai Liu, Feng Jin, Min Guo, Yewei Chen, and Qingxu Yu. *Highly sensitive photoacoustic gas sensor based on multiple reflections on the cell wall*. Sensors and Actuators A: Physical, 290:119–124, 2019.

[83] Qiulin Tan, Xiangdong Pei, Simin Zhu, Dong Sun, Jun Liu, Chenyang Xue, Ting Liang, Wendong Zhang, and Jijun Xiong. *Development of an optical gas leak sensor for detecting ethylene, dimethyl ether and methane*. Sensors, 13(4):4157–4169, 2013.

[84] Jane Hodgkinson, Richard Smith, Wah On Ho, John R Saffell, and Ralph P Tatam. *Non-dispersive infra-red (NDIR) measurement of carbon dioxide at 4.2 μm in a compact and optically efficient sensor*. Sensors and Actuators B: Chemical, 186:580–588, 2013.

[85] N Pelin Ayerden, Mohammadamir Ghaderi, Peter Enoksson, Ger de Graaf, and Reinoud F Wolffenbuttel. *A miniaturized optical gas-composition sensor with integrated sample chamber*. Sensors and Actuators B: Chemical, 236:917–925, 2016.

[86] Lena Simone Fohrmann, Gerrit Sommer, Giampaolo Pitruzzello, Thomas F Krauss, Alexander Yu Petrov, and Manfred Eich. *Integrating cell on chip—Novel waveguide platform employing ultra-long optical paths*. APL photonics, 2(9):096102, 2017.

[87] Adam Sklorz, Anika Schafer, and Walter Lang. *Merging ethylene NDIR gas sensors with preconcentrator-devices for sensitivity enhancement*. Sensors and Actuators B: Chemical, 170:21–27, 2012.

[88] Hehuan Liu, Yunbo Shi, and Tian Wang. *Design of a six-gas NDIR gas sensor using an integrated optical gas chamber*. Optics Express, 28(8):11451–11462, 2020.

[89] Alexander Lochbaum, Alexander Dorodnyy, Ueli Koch, Stefan M Koepfli, Sebastian Volk, Yuriy Fedoryshyn, Vanessa Wood, and Juerg Leuthold. *Compact Mid-Infrared Gas Sensing Enabled by an All-Metamaterial Design*. Nano Letters, 20(6):4169–4176, 2020.

[90] Floria Ottonello Briano. *Mid-infrared photonic devices for on-chip optical gas sensing*. PhD thesis, KTH Royal Institute of Technology, 2019.

2

On-Chip Optical Gas Sensing

2.1 Optical Absorption Spectroscopy

Optical absorption spectroscopy is the technique used to determine the content and concentration of the analyte by means of direct optical absorption. Gas species absorb light at particular wavelengths in the electromagnetic spectrum, resulting in a reduction in the light intensity when the beam passes through the sample. Optical absorption spectroscopy measures this intensity attenuation as a function of wavelength to extract information on the gas species and their concentration.

2.1.1 Absorption spectra and the mid-infrared

Many chemical species absorb light at specific wavelengths in the ultraviolet (UV), visible, near-infrared (near-IR), and mid-infrared (mid-IR) spectral ranges. The absorption is chemical specific and thus this phenomenon can be used for sensing purposes. The mechanisms behind the absorption in different wavelength ranges are different. The absorption of UV or visible radiation originates from the electronic transition of the molecules, in which the outer electrons are excited from the ground state to an excited state upon light absorption. This is also the mechanism giving colors to the chemicals. Near-IR (from $780nm$ to $2.5\mu m$) absorption arises from the excitation of overtones or combination modes of molecular vibrations in the mid-IR range. Such transitions are forbidden by the selection rules of quantum mechanics and therefore the absorption strength in this wavelength range is typically very weak. Unlike UV or visible radiation, mid-IR (from $2.5\mu m$ to $14\mu m$)

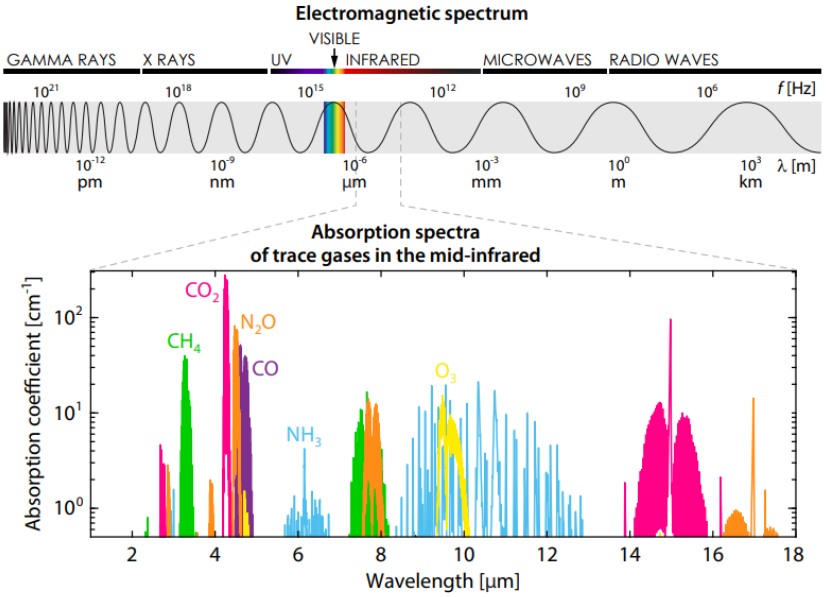

Figure 2.1: The electromagnetic spectrum and the mid-IR 'finger print' region, the absorption spectra of trace gases are for 100% concentration at atmospheric pressure. Adapted from [1].

radiation does not have enough energy for electronic transitions: the absorption of mid-IR radiation stems from the molecular rotational and vibrational (often termed rovibrational) states. The changes in vibrational energy levels give the envelope of the absorption spectrum while the changes in rotational energy levels are superimposed on this envelope as fine lines because the energy difference in rotational energy levels is much smaller than that of vibrational levels.

The absorption from UV to mid-IR has been widely used in optical absorption spectroscopy. UV/visible absorption spectroscopy has been used to measure gaseous species such as ozone, NO_2, and SO_2, as well as the monitoring of nitrate in groundwater [2, 3]. The absorption in the near-IR range is very weak and therefore in principle it is not suitable for sensing. However, the advances in datacom and telecom technologies enrich the availability of high-quality and low-cost optical sources and detectors, which still makes near-IR sensing systems attractive. For instance, on-chip glucose sensing at around $1590nm$ has been reported [4]. Moreover, the overtone bands in the near-IR can overlap significantly at high temperature and high pressure, making the absorption comparable to that in the mid-IR wavelength range. Based on this phenomenon, ammonia sensing at $1512nm$ has been demonstrated [5].

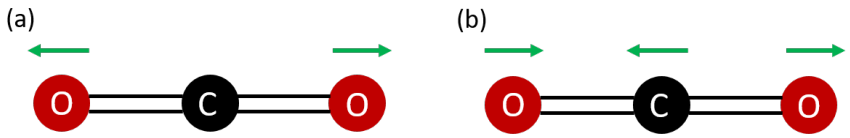

Figure 2.2: (a) Symmetric stretching and (b) antisymmetric stretching of a CO_2 molecule. In symmetric stretching, the two C=O bonds stretch in opposite directions while in antisymmetric stretching one of the C=O bond stretches while the other compresses.

The mid-IR range is of particular interest for sensing applications, as the absorption strength can be significantly larger (up to three orders of magnitude) than that in the near-IR range. Moreover, various commonly-encountered gas species exhibit specific absorption in this wavelength range, therefore the mid-IR is usually called the 'fingerprint region' of the electromagnetic spectrum. Figure 2.1 shows the absorption coefficients for several common gases in the mid-IR range, and more information on other gas species can be accessed via well-known databases such as HITRAN [6].

For a molecule to be infrared active, a change in the dipole moment of the molecule must occur when the molecule vibrate or rotates. This change in dipole moment is induced by the internal motion (vibration and/or rotation) of the atoms. If the incident electromagnetic radiation is at the same frequency with this oscillation the radiation can be absorbed by the molecule. For instance, CO_2 is a centrosymmetric molecule with two C=O bonds and only two vibrational modes are present: symmetric stretching mode and antisymmetric stretching mode, as shown in Figure 2.2. In symmetric stretching, the changes in the electric dipoles of the C=O bonds are the same but in opposite directions, leading to no net change in the dipole moment and thus this vibration is IR inactive. However, this symmetric stretching contributes to the Raman scattering of CO_2 at a wavenumber[1] of $1480cm^{-1}$, which can be used for Raman sensing. In the antisymmetric stretching, one of the C=O bonds stretches while the other compresses, resulting in an overall change in the dipole moment which gives rise to the strong absorption band at $2349cm^{-1}(4.26\mu m)$ as shown in Figure 2.3. This absorption band spans over $80cm^{-1}$ and the absorption coefficient[2] is around $300cm^{-1}$, which is two orders of magnitude higher than the overtone at $2.6\mu m$. Therefore for CO_2 sensing, the wavelength at $4.26\mu m$ is often used.

[1] reciprocal of wavelength, in cm^{-1}
[2] temperature at 296 K and pressure at 101.325 kPa

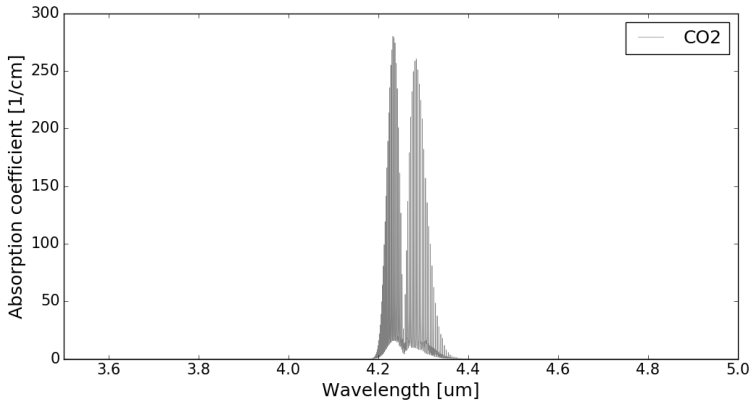

Figure 2.3: Absorption spectrum of 100% CO_2 gas at atmospheric pressure, calculated from the Hitran database [6].

2.1.2 Absorption line shape and line broadening

The shape of an ideal absorption line can be a narrow δ-like function. However several line-broadening mechanisms are present and the absorption lines exhibit a finite linewidth. In general form, the absorption line profile can be described by:

$$k(\nu) = Sg(\nu - \nu_0) \tag{2.1}$$

in which the line strength S is the integrated absorption coefficient given by:

$$S = \int_{-\infty}^{+\infty} k(\nu) d\nu \tag{2.2}$$

and $g(\nu - \nu_0)$ is the line shape function normalized to unity. The width of the line shape is usually quantified by the Full Width at Half Maximum (FWHM). There are two well-known line broadening mechanisms that can alter the absorption line shape: Doppler broadening and pressure/collision broadening. Doppler broadening is caused by the Doppler frequency shift due to the finite molecular velocity distribution at a certain temperature. This broadening effect leads to a Gaussian profile of the absorption line and it is more prominent at low pressures. At atmospheric pressure, the pressure/collision broadening is dominant due to the molecular collisions between the same or different gas species. The resulting line shape profile is Lorentzian and the FWHM is proportional to the pressure of the gas [7]. In general, the line shape of the spectral lines can be described by a Voigt profile, which is the convolution of Gaussian and Lorentzian line shapes.

2.1.3 Beer-Lambert law

Optical absorption spectroscopy is based on the Beer-Lambert law, which states the relationship between the transmitted light intensity and the concentration of the analyte, for monochromatic light:

$$I = I_0 \exp(-\alpha l) \tag{2.3}$$

where I is the intensity of light transmitted through the gas cell, I_0 is the initial light intensity incident on the gas cell, α is the absorption coefficient (in cm^{-1}) of the gas and l is the optical path length (in cm) of the gas cell [8]. The absorption coefficient α can be calculated by multiplying the gas concentration c (in partial pressure of the atmosphere, atm) with the molar specific absorptivity of the gas ϵ (in $cm^{-1}atm^{-1}$). The ratio of the transmitted light intensity and the incident light intensity $\frac{I}{I_0}$ is termed as optical transmittance T. The absorbance A, defined as the fraction of light absorbed by the gas, can be approximated using the Taylor expansion of the exponential function. At low gas concentrations, i.e., when $\alpha l << 1$, the absorbance can be written as:

$$A = 1 - T = \frac{I_0 - I}{I_0} \approx \alpha l \tag{2.4}$$

The absorbance A is unitless but it is often described in 'absorbance units' (AU). The limit of detection (LOD) of the sensing system is quantified as the noise equivalent absorbance (NEA, in AU) or the minimum detectable absorption coefficient (in cm^{-1}), this enables the comparison between different sensing methods without referring to the specific target gas. For gas sensing applications, it is often useful to convert the concentration of target gas to more typical units such as ppm by volume. For this conversion the ideal gas equation $PV = Nk_BT$ is used, where P is the pressure, V is the volume of a closed cell, k_B is the Boltzmann constant and N is the number of molecules.

2.2 Mid-infrared Silicon Photonics

Over the past years, silicon photonics has emerged as an important platform for photonic integrated circuits (PIC) [9]. A PIC consists of various optical elements for light generation, detection and manipulation. While different material platforms have been developed to realize the photonic systems-on-chip, the silicon-on-insulator (SOI) platform is emerging as one of the most popular platforms. The main reason is that the SOI platform is compatible with CMOS/MEMS processes thus the infrastructures in a CMOS/MEMS foundry can be re-used without the need for intensive investment. The SOI platform comprises a silicon device layer (typically 220 nm thick, but can go up to several micrometers), a thermally grown

buried oxide (SiO_2) layer (with a typical thickness of $2\mu m$), and a thick silicon substrate layer. The SOI platform provides a very high refractive index contrast which offers high optical confinement and small bend radii. Therefore an abundance of functionalities can be integrated on a chip with a very small footprint.

Most of the applications of silicon photonics are in telecommunications in the near-IR wavelength range. However, the mid-IR band presents a significant growth opportunity for silicon photonics due to its potential for sensing applications. Mid-IR low-loss waveguides have been demonstrated in the $2\mu m - 4\mu m$ wavelength range on SOI, with performance comparable to their near-IR counterparts [10–14]. Other building blocks for PICs such as grating couplers to couple light in and out of the chip [15, 16], high-Q microring resonators [13], wavelength (de)multiplexers based on arrayed waveguide gratings or planar concave gratings [12, 17], and polarization control devices [18, 19] have also been successfully demonstrated in the IR wavelength range below $4\mu m$ on SOI or on other CMOS/MEMS-compatible platforms.

The SOI platform can be used at wavelengths shorter than $4\mu m$: beyond $4\mu m$, the absorption of the buried oxide layer increases dramatically and the substrate leakage loss increases exponentially, making the waveguiding not practical [20]. However, the wavelength range above $4\mu m$ is of great interest as it contains strong absorption peaks of many important gases such as CO_2, CO, and NH_3, and the absorption coefficients are much larger than the overtones in the near-IR range. To extend the operating wavelength range of silicon photonics without leaving the CMOS foundry, materials other than silicon or silicon oxide can be used. Figure 2.4 shows the transparency windows of a few materials that are compatible with CMOS/MEMS technology. One can see that sapphire and silicon nitride are transparent up to $4.5\mu m$ and $7\mu m$, respectively. They can be used as cladding material due to their relatively low refractive indices ($n_{sapphire} < 1.75$ and $n_{SiN} \approx 2$). Germanium is transparent up to $14.5\mu m$ and it can be used as core material together with silicon cladding due to its high refractive index ($n_{Ge} \approx 4$ and $n_{Si} \approx 3.45$), provided that the (Si) Ge can be grown on silicon with high quality. With these available materials, mid-IR optical sensing has been reported on various platforms such as silicon-on-sapphire for heavy water and CO_2 sensing around $4\mu m$ [21, 22], silicon-on-nitride for CO_2 sensing at $4.26\mu m$ [23], and Germanium-on-silicon [24] for Poly(methyl-methacrylate) (PMMA) polymer sensing at $9\mu m$.

Another approach to extend the SOI platform to the mid-IR wavelength range is to locally remove the buried oxide beneath the silicon waveguide, making the silicon device layer suspended on the buried oxide layer through which the propagation loss due to oxide absorption is greatly reduced. Different geometries have been reported for silicon suspended waveguide structures, including suspended silicon ridge waveguides laterally supported by a thin continuous Si mem-

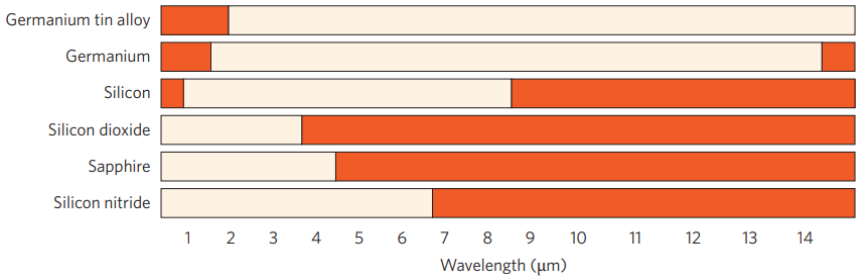

Figure 2.4: Optical transparency window of several common materials used in mid-IR silicon photonics. In the yellow regions the material loss is negligible while the red regions denote heavy material absorption. Adapted from [20].

brane [25, 26], suspended waveguides laterally supported by a sub-wavelength grating [27, 28], suspended photonic crystal waveguides [29], and a strip waveguide supported by a periodic SiO_2 pedestal [30]. Figure 2.5 shows a few examples of such suspended silicon waveguide structures.

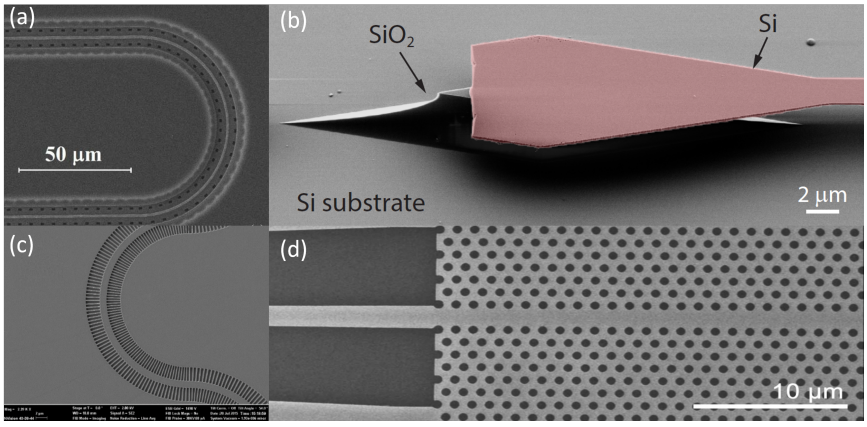

Figure 2.5: Reported suspended waveguide structures for the mid-IR wavelength range. Images taken from [25, 28–30].

2.3 Free-space and guided-wave optical sensing

An optical gas sensing system can either be implemented on-chip by using waveguiding structures such as dielectric waveguides or metallic waveguides, or it can be implemented by using bulk optical components such as beam splitters and folded mirrors in free space, which can also be considered as a light-guiding system. In

the free-space configuration, the light beam undergoes direct interaction with the environment while in the guided-wave configuration the light propagates along the waveguide and interacts with its surroundings. In general form, the transmission T can be written as (Beer-Lambert law):

$$T = \frac{I}{I_0} = \exp(-\alpha_b L)\exp(-\Gamma \epsilon_{gas} c_{gas} L) \tag{2.5}$$

where α_b (in cm^{-1} or m^{-1}) is the attenuation coefficient of the waveguide, or the 'effective' attenuation per unit length in the free-space configuration, c_{gas} is the gas concentration, and ϵ_{gas} is the molar specific absortivity of the gas. Γ is the external confinement factor of the waveguide and is a measure of the overlap between the optical field and the environment. In the free-space configuration, Γ is unity as the whole light beam can interact with the environment. For waveguide-based sensors, the external confinement factor Γ can be calculated by:

$$\Gamma = \frac{\iint_C \mid \overrightarrow{E}(x,y) \mid^2 dxdy}{\iint_\infty \mid \overrightarrow{E}(x,y) \mid^2 dxdy} \tag{2.6}$$

in which the integration domain indices, i.e., C and ∞, stand for cladding cross section and the whole computational domain, respectively. The sensitivity of the sensor can be quantified by the transmission change as a function of the variation in gas concentration:

$$S = \left| \frac{\delta T}{\delta c_{gas}} \right| = T\Gamma c_{gas} L \tag{2.7}$$

We see that the sensitivity is waveguide length dependent. The length of the waveguide can be optimized by taking the derivative of S with respect to waveguide length and then equating it to zero:

$$L_{opt} = \frac{1}{\alpha_b + \Gamma \alpha_{gas} c_{gas}} \tag{2.8}$$

At this optimal waveguide length, the transmission of the waveguide is $1/e$, as can be obtained from Eq. 2.5 and Eq. 2.8. It can be seen from Eq. 2.8 that the optimal length of the waveguide is inversely proportional to the waveguide loss α_b and the external confinement factor Γ. For a free-space sensing system Γ is unity, and the loss per unit length α_b is very low, thus the path length can be made very long to achieve high sensitivity. In a waveguide-based sensor, the loss of the waveguide itself is dominant therefore the waveguide length needs to be optimized accordingly to enhance the sensitivity. To reduce the footprint of the sensor, the waveguide is typically routed into a spiral [4]. The external confinement factor can be increased by careful design of the waveguide [30], by using the TM mode of the waveguide [31], or by using a slot waveguide in which the optical field can be greatly enhanced in the slot region of the waveguide [11, 32].

Another approach to increase the overlap of the light and the environment is to use a hollow-core waveguide. In this case the external confinement factor can be very close to unity. Different hollow-core waveguide structures exist including hollow-core fibers, metallic hollow waveguides and antiresonant reflecting optical waveguides (ARROW). In a hollow-core fiber, a silver (Ag) layer is usually deposited on the inner wall and a dielectric layer of AgI is formed by flowing iodine solution through the fiber [33, 34]. The AgI layer can protect the Ag from oxidation. By controlling the thickness of the AgI dielectric layer, the transmission window of the fiber can be engineered and optimized for a specific wavelength range. Similar to hollow-core fibers, hollow metallic waveguides also utilize reflective metals to guide light: they can either be implemented by coiling a metallic tube [35], or integrated on a metalized substrate [36, 37]. The design of the metallic hollow-core waveguide is very versatile as many metals have strong reflection in the IR wavelength range [38] and an optional dielectric layer can be deposited to tailor the working wavelength. Moreover, hollow-core waveguides can be potentially integrated on silicon substrates, as we will see in Chapter 3. Alternatively, one can use multiple dielectric layer stacks to guide light in the waveguide [39–41]. The light guiding is achieved by confining the leaky modes in a low-index core (air or liquid) by using high-index cladding layers, in which only the wavelengths in antiresonance (hence the name ARROW) will be guided.

2.4 Conclusion

In this Chapter, we discussed the absorption spectra of analytes in the UV/visible, near-IR and mid-IR wavelength ranges and the origins behind them. The mid-IR region is particularly interesting for sensing applications (especially for CO_2 sensing) as it contains strong absorption lines which are orders of magnitudes stronger than the overtones in the near-IR region. Beer-Lambert law was introduced, which is the common working principle for all absorption-based optical sensing techniques. Mid-IR silicon photonics enables the extension of the working wavelength range of the relatively mature silicon photonics technology, making it quite promising for sensing applications. To accommodate silicon photonics for mid-IR sensing applications, either the absorbing SiO_2 layer can be locally removed, or exotic CMOS-compatible material systems can be introduced. Free-space and guided-wave optical sensing were discussed. The latter allows for highly miniaturized optical sensors built on a small chip. For on-chip optical sensors, Beer-Lambert law was revisited by introducing the waveguide loss and the concept of external confinement factor. To increase the sensor sensitivity, a low waveguide propagation loss and a high external confinement factor are desired. Different approaches to enhance the sensor sensitivity by increasing light-matter interaction were reviewed. In the following Chapter, we will explore several pos-

sible sensor configurations that can be used in this thesis work and the optimal configuration will be chosen.

References

[1] Floria Ottonello Briano. *Mid-infrared photonic devices for on-chip optical gas sensing*. PhD thesis, KTH Royal Institute of Technology, 2019.

[2] Sulaiman Khan, David Newport, and Stéphane Le Calvé. *Gas Detection Using Portable Deep-UV Absorption Spectrophotometry: A Review*. Sensors, 19(23):5210, 2019.

[3] Manuela Huebsch, F Grimmeisen, M Zemann, Owen Fenton, Karl G Richards, Philip Jordan, A Sawarieh, P Blum, and N Goldscheider. *Field experiences using UV/VIS sensors for high-resolution monitoring of nitrate in groundwater*. 2015.

[4] Eva Ryckeboer, Ronny Bockstaele, Michal Vanslembrouck, and Roel Baets. *Glucose sensing by waveguide-based absorption spectroscopy on a silicon chip*. Biomedical optics express, 5(5):1636–1648, 2014.

[5] Xinqian Guo, Fei Zheng, Chuanliang Li, Xiaofei Yang, Ning Li, Shuping Liu, Jilin Wei, Xuanbing Qiu, and Qiusheng He. *A portable sensor for in-situ measurement of ammonia based on near-infrared laser absorption spectroscopy*. Optics and Lasers in Engineering, 115:243–248, 2019.

[6] Laurence S Rothman, Iouli E Gordon, Yury Babikov, Alain Barbe, D Chris Benner, Peter F Bernath, Manfred Birk, Luca Bizzocchi, Vincent Boudon, Linda R Brown, et al. *The HITRAN2012 molecular spectroscopic database*. Journal of Quantitative Spectroscopy and Radiative Transfer, 130:4–50, 2013.

[7] Colin N Banwell, Elaine M McCash, et al. *Fundamentals of molecular spectroscopy*, volume 851. McGraw-Hill New York, 1994.

[8] Jane Hodgkinson and Ralph P Tatam. *Optical gas sensing: a review*. Measurement Science and Technology, 24(1):012004, 2012.

[9] Richard Soref. *The past, present, and future of silicon photonics*. IEEE Journal of selected topics in quantum electronics, 12(6):1678–1687, 2006.

[10] Steven A Miller, Mengjie Yu, Xingchen Ji, Austin G Griffith, Jaime Cardenas, Alexander L Gaeta, and Michal Lipson. *Low-loss silicon platform for broadband mid-infrared photonics*. Optica, 4(7):707–712, 2017.

[11] Jordi Soler Penadés, Ali Z Khokhar, Milos Nedeljkovic, and Goran Z Mashanovich. *Low-loss mid-infrared SOI slot waveguides*. IEEE Photonics Technology Letters, 27(11):1197–1199, 2015.

[12] Muhammad Muneeb, Xia Chen, P Verheyen, Guy Lepage, Shibnath Pathak, Eva Ryckeboer, Aditya Malik, Bart Kuyken, Milos Nedeljkovic, Joris Van Campenhout, et al. *Demonstration of Silicon-on-insulator mid-infrared spectrometers operating at 3.8 μm*. Optics Express, 21(10):11659–11669, 2013.

[13] Milan M Milošević, Milos Nedeljkovic, Taha M Ben Masaud, Ehsan Jaberansary, Harold MH Chong, Neil G Emerson, Graham T Reed, and Goran Z Mashanovich. *Silicon waveguides and devices for the mid-infrared*. Applied Physics Letters, 101(12):121105, 2012.

[14] Goran Z Mashanovich, Milan M Milošević, Milos Nedeljkovic, Nathan Owens, Boqian Xiong, Ee Jin Teo, and Youfang Hu. *Low loss silicon waveguides for the mid-infrared*. Optics Express, 19(8):7112–7119, 2011.

[15] Zhenzhou Cheng, Xia Chen, CY Wong, Ke Xu, Christy KY Fung, YM Chen, and Hon Ki Tsang. *Focusing subwavelength grating coupler for mid-infrared suspended membrane waveguide*. Optics letters, 37(7):1217–1219, 2012.

[16] Zhenzhou Cheng, Xia Chen, Chi Yan Wong, Ke Xu, and Hon Ki Tsang. *Broadband focusing grating couplers for suspended-membrane waveguides*. Optics letters, 37(24):5181–5183, 2012.

[17] Aditya Malik, Muhammad Muneeb, Yosuke Shimura, Joris Van Campenhout, Roger Loo, and Gunther Roelkens. *Germanium-on-silicon planar concave grating wavelength (de) multiplexers in the mid-infrared*. Applied Physics Letters, 103(16):161119, 2013.

[18] Ting Hu, Mohamed Saïd Rouifed, Haodong Qiu, Xin Guo, Callum G Littlejohns, Chongyong Liu, and Hong Wang. *A polarization splitter and rotator based on a partially etched grating-assisted coupler*. IEEE Photonics Technology Letters, 28(8):911–914, 2016.

[19] Ting Hu, Haodong Qiu, Zecen Zhang, Xin Guo, Chongyang Liu, Mohamed S Rouifed, Callum G Littlejohns, Graham T Reed, and Hong Wang. *A compact ultrabroadband polarization beam splitter utilizing a hybrid plasmonic Y-branch*. IEEE Photonics Journal, 8(4):1–9, 2016.

[20] Richard Soref. *Mid-infrared photonics in silicon and germanium*. Nature photonics, 4(8):495, 2010.

[21] Neetesh Singh, Alvaro Casas-Bedoya, Darren D Hudson, Andrew Read, Eric Mägi, and Benjamin J Eggleton. *Mid-IR absorption sensing of heavy water using a silicon-on-sapphire waveguide*. Optics letters, 41(24):5776–5779, 2016.

[22] Yuewang Huang, Salih K Kalyoncu, Qiancheng Zhao, Rasul Torun, and Ozdal Boyraz. *Silicon-on-sapphire waveguides design for mid-IR evanescent field absorption gas sensors*. Optics Communications, 313:186–194, 2014.

[23] Christian Ranacher, Cristina Consani, Natalie Vollert, Andreas Tortschanoff, Markus Bergmeister, Thomas Grille, and Bernhard Jakoby. *Characterization of evanescent field gas sensor structures based on silicon photonics*. IEEE Photonics Journal, 10(5):1–14, 2018.

[24] U Griškevičiūtė, RW Millar, K Gallacher, L Baldassarre, M Sorel, M Ortolani, and DJ Paul. *Fingerprint mid-infrared sensing with germanium on silicon waveguides*. In 2019 Conference on Lasers and Electro-Optics (CLEO), pages 1–2. IEEE, 2019.

[25] Zhenzhou Cheng, Xia Chen, Chi Yan Wong, Ke Xu, and Hon Ki Tsang. *Mid-infrared suspended membrane waveguide and ring resonator on silicon-on-insulator*. IEEE photonics journal, 4(5):1510–1519, 2012.

[26] Floria Ottonello-Briano, Carlos Errando-Herranz, and Kristinn B Gylfason. *On-chip dispersion spectroscopy of mid-infrared molecular fingerprints using a microring resonator*. 2019.

[27] J Soler Penadés, C Alonso-Ramos, AZ Khokhar, Milos Nedeljkovic, LA Boodhoo, A Ortega-Moñux, I Molina-Fernández, Pavel Cheben, and GZ Mashanovich. *Suspended SOI waveguide with sub-wavelength grating cladding for mid-infrared*. Optics letters, 39(19):5661–5664, 2014.

[28] J Soler Penades, Alejandro Ortega-Moñux, Milos Nedeljkovic, JG Wangüemert-Pérez, Robert Halir, AZ Khokhar, Carlos Alonso-Ramos, Zhibo Qu, Iñigo Molina-Fernández, Pavel Cheben, et al. *Suspended silicon mid-infrared waveguide devices with subwavelength grating metamaterial cladding*. Optics express, 24(20):22908–22916, 2016.

[29] Christian Reimer, Milos Nedeljkovic, David JM Stothard, Matthieu OS Esnault, Christopher Reardon, Liam O'Faolain, Malcolm Dunn, Goran Z Mashanovich, and Thomas F Krauss. *Mid-infrared photonic crystal waveguides in silicon*. Optics Express, 20(28):29361–29368, 2012.

[30] Floria Ottonello-Briano, Carlos Errando-Herranz, Henrik Rodjegård, Hans Martin, Hans Sohlström, and Kristinn B Gylfason. *Carbon Dioxide Sensing with Low-confinement High-sensitivity Mid-IR Silicon Waveguides*. In CLEO: Science and Innovations, pages STh1F–3. Optical Society of America, 2019.

[31] Yu-Chi Chang, Vincent Paeder, Lubos Hvozdara, Jean-Michel Hartmann, and Hans Peter Herzig. *Low-loss germanium strip waveguides on silicon for the mid-infrared*. Optics letters, 37(14):2883–2885, 2012.

[32] Pao Tai Lin, Sen Wai Kwok, Hao-Yu Greg Lin, Vivek Singh, Lionel C Kimerling, George M Whitesides, and Anu Agarwal. *Mid-infrared spectrometer using opto-nanofluidic slot-waveguide for label-free on-chip chemical sensing*. Nano letters, 14(1):231–238, 2014.

[33] Pietro Patimisco, Vincenzo Spagnolo, Miriam S Vitiello, Gaetano Scamarcio, Carlos M Bledt, and James A Harrington. *Low-loss hollow waveguide fibers for mid-infrared quantum cascade laser sensing applications*. Sensors, 13(1):1329–1340, 2013.

[34] Jason M Kriesel, Nahum Gat, Bruce E Bernacki, Rebecca L Erikson, Bret D Cannon, Tanya L Myers, Carlos M Bledt, and James A Harrington. *Hollow core fiber optics for mid-wave and long-wave infrared spectroscopy*. In Chemical, Biological, Radiological, Nuclear, and Explosives (CBRNE) Sensing XII, volume 8018, page 80180V. International Society for Optics and Photonics, 2011.

[35] Jinyi Li, Zhenhui Du, Zheyuan Zhang, Limei Song, and Qinghua Guo. *Hollow waveguide-enhanced mid-infrared sensor for fast and sensitive ethylene detection*. Sensor Review, 2017.

[36] Andreas Wilk, J Chance Carter, Michael Chrisp, Anastacia M Manuel, Paul Mirkarimi, Jennifer B Alameda, and Boris Mizaikoff. *Substrate-integrated hollow waveguides: a new level of integration in mid-infrared gas sensing*. Analytical chemistry, 85(23):11205–11210, 2013.

[37] Martin De Biasio, Raimund Leitner, Christoph Krall, Matic Krivec, Andreas Wilk, Boris Mizaikoff, Roland Waldner, Frans Starmans, and Dieter Maier. *Ethylene gas sensing using non-dispersive infrared spectroscopy*. In 2016 IEEE SENSORS, pages 1–3. IEEE, 2016.

[38] Edward D Palik. *Handbook of optical constants of solids*, volume 3. Academic press, 1998.

[39] Philip Measor, Brian S Phillips, Aiqing Chen, Aaron R Hawkins, and Holger Schmidt. *Tailorable integrated optofluidic filters for biomolecular detection*. Lab on a chip, 11(5):899–904, 2011.

[40] Thomas Wall, Johnny McMurray, Gopikrishnan Meena, Vahid Ganjalizadeh, Holger Schmidt, and Aaron R Hawkins. *Optofluidic lab-on-a-chip fluorescence sensor using integrated buried ARROW (bARROW) waveguides*. Micromachines, 8(8):252, 2017.

[41] Jeffrey E Melzer, Wesley Y Kendall, and James A Harrington. *High-index-contrast multilayer hollow waveguides for mid-IR laser delivery*. In Optical Fibers and Sensors for Medical Diagnostics and Treatment Applications XVI, volume 9702, page 97020K. International Society for Optics and Photonics, 2016.

3

NDIR CO_2 Sensor Configurations

3.1 Introduction

In this Chapter, three possible configurations to realize an on-chip NDIR CO_2 sensor are proposed, including sensors based on a multi-mode slotted silicon waveguide, sensors based on a metallic hollow waveguide, and sensors based on a metallic integrating cylinder. The multi-mode slotted waveguide approach can be implemented on the SOI platform and therefore a compact and low-cost CO_2 sensor can be potentially obtained using silicon photonics technology. The hollow metallic waveguide approach uses metallic waveguide instead of dielectric waveguide for wave/light guiding and for gas sensing. It can also be fabricated using CMOS/MEMS-compatible technologies, resulting in potential mass production of the sensor at low cost. The idea of the integrating cylinder arises by asking ourselves the question "can we make the sensor even smaller than that using the metallic waveguide?". The working principle of the integrating cylinder resembles that of an integrating sphere, which is widely employed in photometric applications. In what follows, the three approaches will be explored and compared. Simulations are carried out at both system and component level to address the design considerations such as waveguide loss and source/detector coupling efficiencies. The simulation results are used to calculate the power budgets of these three approaches. Finally, based on the power budget calculation together with other factors such as manufacturing complexity and cost, the optimal approach is chosen and fixed for further exploration.

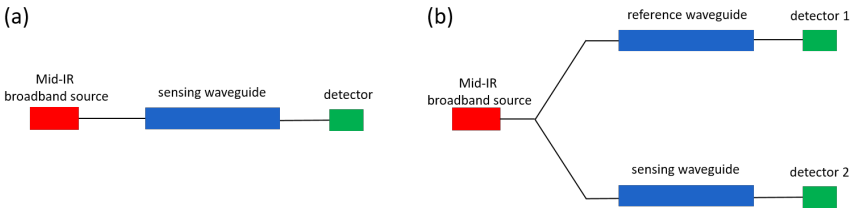

Figure 3.1: Schematic of the NDIR sensor system. (a) Single-beam configuration. (b) Dual-beam configuration.

3.2 Sensor system

The simplest implementation of an on-chip NDIR CO_2 sensor system is a single-beam configuration as shown in Figure 3.1(a). The sensor consists of a broadband source, a sensing waveguide, and a detector. The main drawback of this configuration is that any light intensity variations originating from factors other than CO_2 absorption, such as source power fluctuations and waveguide aging, are also measured. It is therefore impossible to distinguish between the actual signal and the false signals. A dual-beam configuration can be used to eliminate these types of noise, in which part of the light from the source is directed to the reference arm and measured. A second detector is used to monitor the variations due to e.g. source intensity fluctuations, therefore auto-calibration of the sensor can be achieved. The reference arm can be implemented using a physical reference waveguide isolated from the ambient, therefore the reference signal will not change when there is a change in the CO_2 concentration. Alternatively, one can use a reference wavelength (eg. $3.9\mu m$ for CO_2 sensing) which does not overlap with the absorption band of CO_2 or any commonly encountered molecules, thus the need for the reference waveguide can be eliminated. In the dual-beam configuration, the optical power at the sensing arm and the reference arm, not taking into account the noise, can be written as:

$$\begin{aligned} P_{sens} &= P_{in}\exp(-\alpha_{WG}L)\exp(-\epsilon c\Gamma L) \\ P_{ref} &= P_{in}\exp(-\alpha_{WG}L) \end{aligned} \tag{3.1}$$

where P_{in} is the incident power, α_{WG} is the waveguide propagation loss, L is the waveguide length, ϵ is the molar absorption coefficient, Γ is the confinement factor in air of the guided mode, and c is the CO_2 concentration. The optical power change due to variations of CO_2 concentration can be calculated by:

$$\begin{aligned} \Delta P = P(c+\Delta c) - P(c) &= P_{in}\exp(-\alpha_{WG}L)\exp(-\epsilon c\Gamma L)(1-\exp(-\epsilon\Delta c\Gamma L)) \\ &\approx P_{in}\exp(-\alpha_{WG}L)(\epsilon c\Gamma L) \end{aligned} \tag{3.2}$$

The CO_2 concentration change can thus be related to the optical power change by:

$$\Delta c = \frac{\Delta P \exp(\alpha_{WG} L)}{P_{in} \epsilon \Gamma L} \tag{3.3}$$

For a certain detector, the minimum optical power change can be detected (termed as noise equivalent power, or NEP) is fixed. Therefore to increase the sensitivity of the sensor (i.e. to measure a lower CO_2 concentration change), the following approaches can be explored:

- Increase the confinement factor in air Γ of the waveguide
- Decrease the waveguide loss α_{WG}
- Increase the optical power P_{in} in the waveguide

In the following sections, these three approaches for increasing the sensor sensitivity will be discussed for the proposed sensor configurations, namely sensor configurations based on a multi-slotted silicon waveguide, a hollow metallic waveguide and a metallic integrating cylinder. The corresponding integration modalities of the optical source and detector will also be discussed. The major sub-components of the three sensor configurations will be investigated by numerical simulations, the simulated parameters (propagation losses, coupling efficiencies, etc.) are used to calculate and compare the power budgets of the three sensor configurations.

3.3 Multi-slot waveguide

In an integrated optical gas sensor, the design of the waveguide is crucial to ensure high sensing performance. A simple strip waveguide implemented on the SOI platform can be used for absorption-based optical sensing [1]. However, the high refractive index contrast between the core material (Si) and the cladding material (SiO_2 or air) results in strong confinement of the optical field in the high-refractive index core region. Therefore, the evanescent field available for sensing is usually quite limited, leading to poor sensitivity of the sensor. In this context, the slot waveguide is more suitable for sensing applications, as it provides a high optical field confinement in the slot region where the analyte to be detected is concentrated [2, 3]. The multi-slot waveguide has been proposed to further enhance the optical confinement in the low-index slot regions and to increase sensitivity of the sensor [4–6]. The concept of a multi-slot waveguide is similar with a slot waveguide, except that multiple slots are formed in the waveguide in between the periodic thin silicon strips. A 3D schematic of such a multi-slot waveguide is depicted in Figure 3.2. When the dimensions of the silicon strips and the slots are much smaller than a wavelength, the multi-slot waveguide core will act as an effective medium for the optical field [6]. The buried oxide (BOX) layer beneath the silicon waveguide

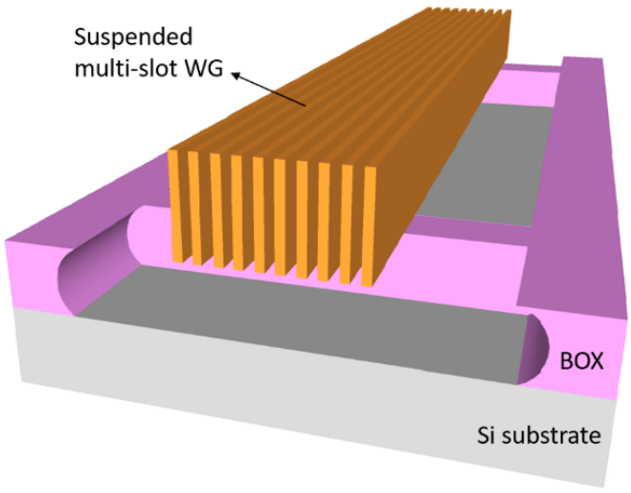

Figure 3.2: Schematic of a multi-slot silicon waveguide, the buried oxide (BOX) layer is partly under-etched to reduce the absorption loss of the optical mode, periodic SiO_2 pillars are formed for mechanical support.

is partially under-etched to reduce the absorption loss of the waveguide, as SiO_2 has a significant absorption at wavelengths beyond $4\mu m$. To provide mechanical support for the multi-slot waveguide, periodic SiO_2 pillars are formed by selective etching of the BOX layer. The advantage of this approach is that the waveguide can be implemented on the SOI platform without leaving the CMOS/MEMS foundry, resulting in potential mass production with extremely low cost.

3.3.1 Waveguide design

Waveguide simulation

In the multi-slot waveguide proposed in this thesis work, the silicon strips are 300nm wide, separated by slots that are 200nm wide. To increase the coupling efficiency from a surface-emitting LED or a thermal light source, a large waveguide core is preferred. We set the height of the silicon strips to be $5\mu m$, due to the limited aspect ratio of deep reactive ion etching (with a typical aspect ratio of ~ 20). For a wavelength of $4.26\mu m$, the waveguide is highly multi-modal and the large waveguide core makes it easier to couple light from a surface-emitting LED or a thermal light source, which will be elaborated in the next section. Figure 3.3(a) shows the cross-section of the waveguide structure with 10 silicon strips. The multi-slot waveguide is simulated using a full vectorial finite difference eigenmode solver (Lumerical MODE solutions). The electric field profiles of the fundamental TE and TM modes of the multi-slot waveguide are depicted in Figure

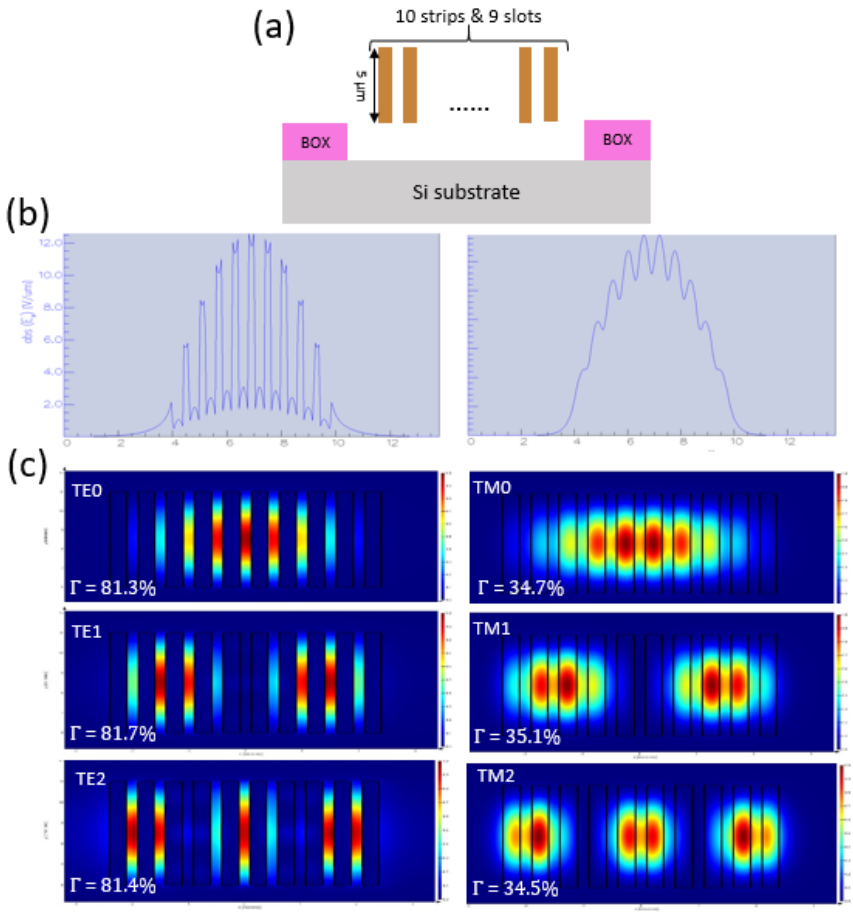

Figure 3.3: (a) Cross-section of the multi-slot waveguide. (b) Horizontal components of the electric fields of the fundamental TE and TM modes in the middle of the waveguide. (c) 2D field profiles of the first three TE and TM modes.

3.3(b). It can be seen that due to the boundary conditions of Maxwell's equations, the electric fields have peaks in the low-index (air) slots region for the TE mode, and have dips for the TM mode. Figure 3.3(c) shows the modal profiles of the first three quasi-TE and quasi-TM eigenmodes of the waveguide at $4.26\mu m$, with their corresponding confinement factors in air (Γ). The confinement factors in air for the quasi-TE and quasi-TM polarizations are about 80% and 35%, respectively. The propagation loss of the multi-slot waveguide originates from several contributions and can be reduced by the following approaches:

- Material absorption. The absorption loss of SiO_2 above $4\mu m$ plays an important role for the propagation loss of the multi-slot waveguide. Calcula-

tions show that the absorption loss of bulk SiO_2 at $4.26\mu m$ is about 18dB/cm[1]. Therefore, the SiO_2 underneath the silicon waveguide is partly under-etched to reduce the absorption loss of SiO_2.

- Substrate leakage loss. The leakage loss from the waveguide to the substrate is negligible for a standard silicon wire waveguide ($450nm \times 220nm$) due to the high confinement of the optical mode. For the multi-slot waveguide proposed in this work, the optical modes are less confined (which is beneficial for sensing applications) due to the presence of the sub-wavelength slots. This may increase the leakage loss if the thickness of the BOX layer is not chosen properly, especially for the poorly-confined higher order modes. Simulation shows that the leakage loss can be minimized by using a BOX thickness of above $5\mu m$.

- Sidewall scattering loss. The scattering at the waveguide sidewalls is an important contribution of the waveguide loss and it stems from the Rayleigh scattering due to the sidewall roughness of the waveguide after etching [8]. The scattering loss for the multi-slot waveguide is higher than that of a standard Si wire waveguide as more sidewalls are felt by the guided modes. However, since the strength of Rayleigh scattering is inversely proportional to the fourth power of the wavelength ($\sim \frac{1}{\lambda^4}$), the scattering loss is expected to be smaller for longer wavelengths such as $4.26\mu m$. Furthermore, the waveguide perturbation caused by the sidewall roughness of the multi-slot waveguide can introduce mutual coupling between different guided modes, as a result, the overall propagation loss can be reduced.

- BOX pillar loss. As shown in Figure 3.2, the suspended multi-slot waveguide needs to be supported by periodic SiO_2 pillars. The field profile of a certain guided mode in the supported and un-supported region are different, leading to scattering losses at the BOX pillar. To estimate this loss, the field profiles of the eigenmodes in the supported region and un-supported region are simulated in Lumerical MODE, and the scattering loss for each mode is determined by calculating the overlap integral of each mode in the supported and un-supported regions. Simulation shows that for a SiO_2 pillar that is $5\mu m$ wide (in longitudinal direction), the loss is about 0.3dB/pillar, assuming that all guided modes carry equal optical power. This is however an overestimation, since light can also be scattered to other guides modes.

[1] Calculated from [7].

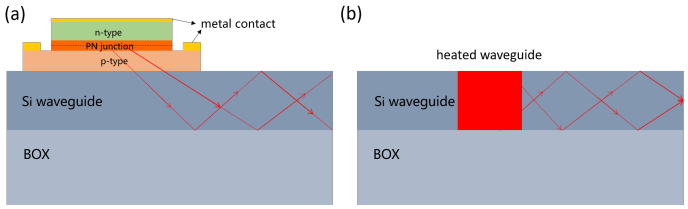

Figure 3.4: Two types of optical sources for the multi-slot waveguide. (a) Mid-IR III-V LED heterogeneously integrated on the silicon waveguide. (b) Thermal source realized by heating the (doped) waveguide to a target temperature.

3.3.2 Optical source and detector

3.3.2.1 Optical source

As shown in Figure 3.4, two types of optical sources are envisioned for the multi-slot waveguide: either a mid-IR III-V LED is heterogeneously integrated onto the silicon waveguide circuit using die-to-wafer bonding or transfer printing, or a thermal (black body) source can be integrated by locally doping the silicon waveguide and heat it to a target temperature.

Mid-IR III-V LED

Mid-IR LEDs offer superior power spectral density compared to thermal sources as the emission spectrum is narrow (relative to a thermal emitter) and can be better matched to the gas absorption band. The emission wavelength of the III-V mid-IR LEDs can be tuned by engineering the composition of certain elements in the III-V semiconductor alloys, provided that the alloys can be lattice-matched to a certain substrate in order to minimize the defects. Figure 3.5(a) shows the bandgap energy and the lattice constants of various III-V semiconductors. It can be seen that for LEDs to emit at $4.26\mu m$ wavelength range (bandgap energy $E_g \sim 0.3eV$), a narrow-bandgap material system based on antimonide semiconductors such as GaSb, AlSb, InSb and their alloys has to be used. Figure 3.5(b) shows the layer stack of one possible implementation of such a mid-IR LED emitting at $4.26\mu m$, with the layer stack and the thicknesses extrapolated from [9]. The epi-layers consist of a homogeneous p-i-n diode based on AlInSb, a GaSb buffer layer, and a GaAs substrate layer. The LED can be integrated with the photonic waveguide circuits using transfer printing [10]. In this regard, a release layer of AlGaAs can be grown in between the GaAs substrate and the GaSb buffer layer.

To estimate the coupling efficiency from the transfer-printed LED to the silicon waveguide, a 3D ray tracing approach (in OpticStudio) is used as the thickness of the LED ($\sim 6\mu m$) is much larger than a wavelength (in the material). The simulation setup is as the following:

- Simulation is performed using the non-sequential mode of OpticStudio, as

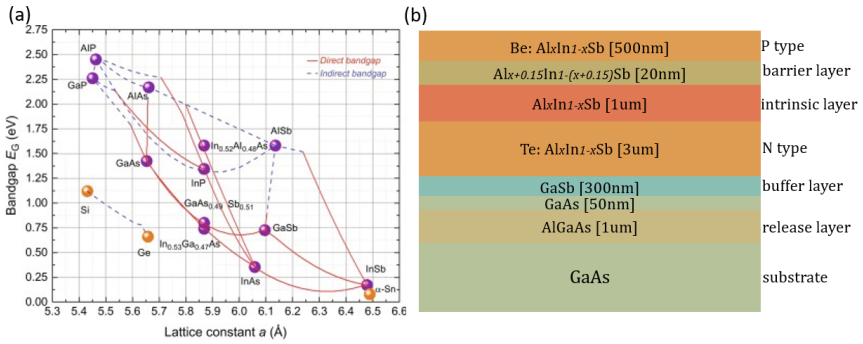

Figure 3.5: (a) Bandgap energy and lattice constants of the III-V semiconductor alloys. (b) Layer stack of the transfer-printable mid-IR LED proposed in this work, extrapolated from [9].

it allows for multiple reflections of the light rays at a certain interface.

- The refractive index (RI) of the active region ($Al_xIn_{1-x}Sb$) is calculated from[2] the Ravindra relation [11]: $n = 4.084 - 0.62E_g = 3.9$. We assume one single RI for the LED because the change in the RI due to doping is very small and the layers are thin compared to the wavelength. The RI of silicon is set to be 3.42.
- The absorption coefficient of the LED is set to be $3000cm^{-1}$, which is a reasonable assumption for AlInSb alloys with low Al composition [12].
- A gold mirror is placed on the top surface of the LED, as the top surface can be fully metallized to realize the top contact.
- A rectangular volume source emitting at $4.26\mu m$ is placed at the center of the LED, with isotropic emission in all directions. A rectangular power detector is placed at the cross-section of the silicon waveguide to record the power coupled to the waveguide.

In the simulation, a total number of 100,000 rays are emitted from the LED, and the optical power is equally distributed in each ray. The coupling efficiency from the LED to the silicon waveguide is simulated to be about 10%(in one direction).

Thermal source

The thermal (black body) source approach is conceptually more novel and it has the advantage of lower cost and easier mass manufacturability. The thermal source can be implemented by locally doping part of the silicon waveguide (or alternatively a cavity is etched and filled with a material that has a good emissivity in

[2] Alternatively it can be calculated from $n = 3.96 - 0.91x$, with 3.96 being the RI of InSb and $x = 6.1\%$ for light emission at $4.3\mu m$ [9]

the $4\mu m$ region) and then heat it to a target temperature by electrical current. It should be placed on a freestanding membrane to increase the thermal isolation and hence limit the power consumption. The working temperature of the thermal source should ensure sufficient light in the required wavelength range while still be acceptable as operating temperature for the electrical connections.
To model the incoherent radiation from the thermal source, a dipole source is used in the finite-difference time-domain simulation (in Lumerical FDTD solver). A series of simulations are carried out to calculate the coupling from the thermal source to all the guided modes of the silicon waveguide, in each simulation the dipole source is placed at one position of the waveguide cross section. At each position, the transmission from the dipole source to the waveguide is averaged over 3 dipole orientations (x, y and z). As the thermal source is a homogeneous radiator, the coupling efficiency is averaged over the dipole positions (i.e. number of dipoles). The simulated coupling efficiency from the thermal source to the waveguide is about 30% (in one direction). The difference in the coupling efficiencies between the thermal source (30%) and the transfer-printable LED (10%) is because the thermal source can be integrated 'in' the silicon waveguide, therefore the emitted light can be captured by the waveguide due to the high refractive index contrast between silicon and air. While in the LED case, the relatively high refractive index contrast between the III-V materials (3.9) and silicon (3.4) makes it more difficult for light to be coupled into the waveguide, leading to a lower coupling efficiency.

3.3.2.2 Optical detector

At the detector side, thermal detectors such as thermopiles and microbolometers are used. These devices can be operated over a broad temperature range. Moreover, they can be fabricated using silicon-based MEMS/CMOS technologies and can be monolithically integrated on the silicon waveguide circuit. In a thermopile detector, the thermoelectric effect is used as temperature readout. Two dissimilar materials are connected to form a thermocouple, and an electrical potential is generated when a temperature gradient is applied between the hot side and the cold side. The output impedance of the thermometer can be increased by using many thermocouples in series. The microbolometer employs an electrical resistance thermometer to measure the temperature of the radiation absorber, which can be achieved by partially doping the silicon waveguide. Waveguide-integrated microbolometers have been demonstrated on the SOI platform [13]. While these devices are typically less sensitive than semiconductor based devices, they perform better at higher temperatures, which is key for many applications (eg. automotive). For the power budget calculation, we simply assume the coupling efficiency from the silicon waveguide to the thermal detector to be 100%, as the microbolometer can be potentially integrated with the silicon waveguide.

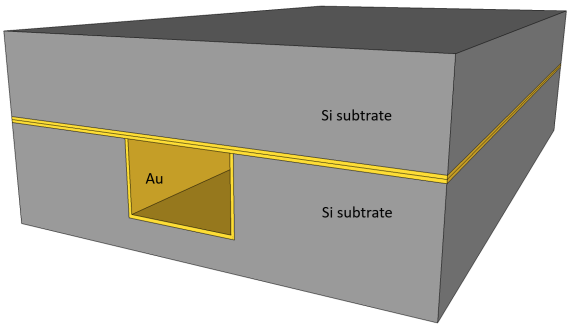

Figure 3.6: Schematic of the metallic hollow waveguide, the waveguide is formed by bonding two metalized silicon substrates. The waveguide is etched on one substrate and the other one is just a planar substrate.

3.3.2.3 Transition loss

The use of a high index contrast (un-slotted) silicon waveguide allows for an efficient coupling of the radiation from both the III-V LED and the thermal source into the waveguide. However, the un-slotted silicon waveguide has to be transitioned to the multi-slot waveguide for optimal sensing, which leads to optical losses. To estimate this transition loss, the eigenmodes of the slotted waveguide region and the un-slotted waveguide region are calculated. Then the overlap integrals of each guided mode in the two regions are calculated to determine the transition loss for each mode, and the transition loss is then averaged over all guided modes assuming all guided modes carrying equal power. The simulated transition loss from the un-slotted waveguide to the slotted waveguide is $\sim 44\%$. One should note that this simulated transition loss is higher than the actual loss, as a certain guided mode in the un-slotted waveguide can couple to other guided modes in the slotted waveguide when the transition happens, which can not be considered as a transition loss.

3.4 Metallic hollow waveguide

The metallic hollow waveguide approach uses a metallic waveguide for sensing. Figure 3.6 shows the schematic of such a metallic hollow waveguide. In the hollow waveguide, light is guided by the reflective mirrors deposited on the sidewalls. Therefore all the light can be used for gas sensing ($\Gamma = 1$). Hollow waveguide structures such as hollow core fibers have been extensively used for sensing applications, as discussed in Chapter 2. In this thesis, we aim for a hollow metallic waveguide that can be integrated on a silicon chip using MEMS compatible technologies.

3.4.1 Waveguide design

The theory of the hollow metallic waveguide has been well-developed from the viewpoint of both wave and ray optics [14–16]. In general, the propagation loss of the hollow metallic waveguide depends on two factors: the dimensions of the waveguide and the reflectance of the mirrors on the sidewalls, and this dependency is given by [16]:

$$\alpha = (\frac{u_{mn}}{2\pi})^2 \frac{\lambda^2}{a^3} \frac{n}{n^2 + k^2} \tag{3.4}$$

where α is the attenuation coefficient; u_{mn} is a mode-dependent parameter; a is the dimension of the cross section (circle or square) of the waveguide core; n and k are the refractive index and the extinction coefficient of the metal film, respectively, which determine the reflectance of the metallic mirror. One can see that the waveguide loss α scales with $\frac{1}{a^3}$, therefore to reduce the propagation loss of the waveguide, large waveguide dimensions are needed. It has been demonstrated that the propagation loss can be lower than 1dB/m at $1.55\mu m$ for a hollow waveguide with a core size of 1mm [17]. For the on-chip hollow core waveguide proposed in this work, we limit the height (etch depth of the Si substrate) of the core to be below $400\mu m$ to provide a high rigidity of the chip, as the thickness of the silicon wafer used in this work is about $700\mu m$. For such large core dimensions, the waveguide is highly multi-modal, and the waveguide can be easily simulated using less computation-intensive techniques such as ray tracing. Figure 3.7(a) shows the simulated propagation loss for a hollow waveguide with various widths. The height of the waveguide is fixed at $300\mu m$, and the simulation setup is depicted in the inset. In this simulation, an isotropic point source (S) emitting at $4.26\mu m$ is placed at the center of the cross section of the waveguide, and two rectangular power detectors (P_1, P_2) are placed in the waveguide with a separation distance of L. The inner walls of the hollow waveguide are covered by a thin layer (thickness = $1\mu m$) of gold, with the optical constants at $4.26\mu m$ given by Table 3.1. The waveguide loss is calculated by Loss[dB] $= -10\log(\frac{P_2}{P_1})/L$. For a square waveguide that is $300\mu m \times 300\mu m$, the propagation loss is about 2.3dB/cm. One should note that the simulated propagation loss is also related to the cone angle of the rays emitted from the source, as shown in Figure 3.7(b). The increased propagation loss for larger cone angles corresponds to the higher losses for higher order modes.

In the proposed hollow waveguide, we use gold as a mirror. The choice of gold over other metals originates from the fact that gold has a very high reflectance in the $4\mu m$ wavelength range, therefore the propagation loss can be minimized. The reflectance of a metal film depends on the wavelength of the incident light, the polarization state of the incident light, and the angle of incidence. At normal incidence, the reflectance of a metal film can be calculated from the optical con-

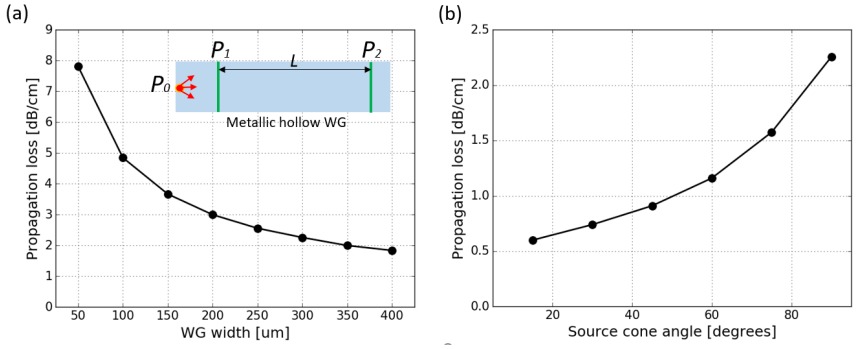

Figure 3.7: Metallic hollow core waveguide simulation. (a) Propagation loss of the hollow waveguide with various widths, the height of the waveguide is $300\mu m$, an isotropic point source (at $4.26\mu m$) is used and gold coatings are applied on the sidewalls as reflective mirrors. (b) Propagation loss for various cone angles of the source for a $300\mu m \times 300\mu m$ square waveguide, a cone angle of 90° corresponds to half a sphere.

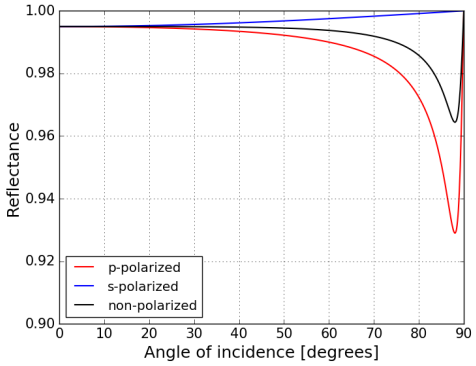

Figure 3.8: Reflectance of gold at $4.26\mu m$ against angle of incidence.

stants [18]:

$$R = \frac{(n-1)^2 + k^2}{(n+1)^2 + k^2} \tag{3.5}$$

At oblique incidence, polarization becomes important and the average reflectance decreases as the incident angle increases, Figure 3.8 shows the reflectance of gold at $4.26\mu m$ as a function of incidence angle, the dip in the reflectance of the p-polarization corresponds to the Brewster's angle.

Table 3.1 lists the optical constants (at $4.26\mu m$) of several common metals [19, 20] and the calculated reflectance using Eq.3.5. It can be seen that gold has the highest reflectance ($\sim 99.5\%$) among gold, silver, aluminium and copper. Another advantage of using gold as a reflector is that gold is chemically inert and stable,

leading to a better long-term stability of the sensor.

Metal	n	k	R
Au	1.0723	29.143	0.995
Ag	1.9658	31.121	0.992
Al	7.3795	40.921	0.983
Cu	1.4247	30.636	0.994

Table 3.1: Optical constants and calculated reflectance of gold, silver, aluminum, and copper at $4.26\mu m$.

3.4.2 Optical source and detectors

For the hollow waveguide, off-the-shelf mid-IR LED and photodiode bare chips can be used as source and detectors, and these bare chips can be very cheap when purchased in a large volume. The LED and photodiode chips can be integrated with the hollow waveguide with the following processes: (1) a trench is formed on a planar silicon substrate by selective silicon etching using potassium hydroxide (KOH) or Tetramethyl ammonium hydroxide (TMAH); (2) gold is deposited on this planar substrate as well as on the other substrate containing the hollow waveguide structures[3]; (3) the LED/photodiode chip is then bonded in the trench (with emission/detection sides facing up) by flip-chip bonding; (4) the substrate containing the hollow core waveguide structures is flip-chip bonded with the planar substrate (with LED and photodiode on-chip). A detailed explanation of the integration procedures will be given in Chapter 5. Figure 3.9 shows the schematic of the hollow waveguide structure with an integrated LED (or photodiode).

The coupling efficiency from the LED to the hollow waveguide (η_{LED}) and from the waveguide to the photodiode (η_{PD}) are simulated with 3D ray tracing in OpticStudio. The simulation gives a coupling efficiency $\eta_{LED} = 8\%$ and $\eta_{PD} = 30\%$, the details of this simulation will be elaborated in Chapter 5.

3.5 Metallic integrating cylinder

The integrating cylinder can be considered as a '2D' version of an integrating sphere. In an integrating sphere, the incident light from the entrance port is uniformly scattered/diffused by the white diffusely reflective coating on the interior of the sphere. Light rays incident on any point of the inner surface are reflected multiple times before reaching the exit ports, leading to a long optical path length and hence the integrating sphere can be used for sensing applications [21–23]. The

[3]The fabrication process of the waveguide structures will be elaborated in Chapter 4

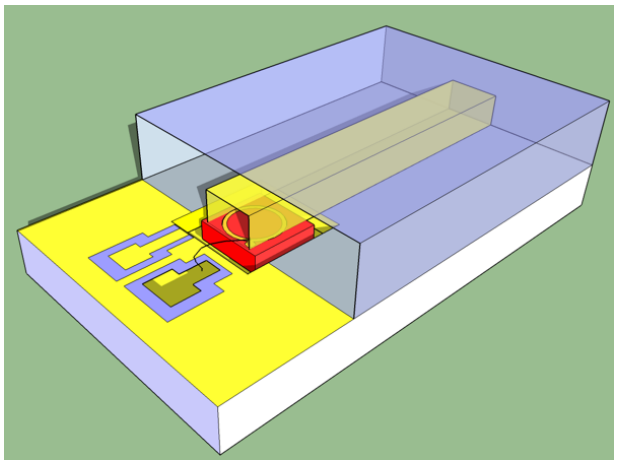

Figure 3.9: Hollow core waveguide with an LED (or a photodiode) integrated on-chip. The LED and photodiode can be integrated on-chip using the same processes.

implementation of the integrating cylinder proposed in this work is similar to that of an on-chip hollow waveguide: instead of using a long channel-like waveguide, a cylindrical cavity with rough sidewalls is used for light guiding. A schematic of the on-chip integrating cylinder is depicted in Figure 3.10.

3.5.1 Integrating cylinder analysis and simulation

The integrating cylinder consists of a hollow gold-coated cylindrical cavity along with hollow metallic waveguides, one at the input and two at the output, realized by Deep Reactive Ion Etching (DRIE) and wafer bonding. The theoretical analysis and numerical simulation of the integrating cylinder will be presented in detail in Chapter 4. Here we present some main results from the ray tracing simulation of the integrating cylinder:

- The total loss (in dB) from the input waveguide to one of the output waveguides and the equivalent path length of the integrating cylinder scale with the radius of the cylinder (nearly) linearly, and it is larger for smaller input/output waveguide widths.
- The sensitivity of the integrating cylinder, defined as the transmission difference with/without the presence of an absorbing medium (eg. CO_2), is maximized for a certain cylinder radius and waveguide width combination.
- For a cylinder radius of 2mm and a waveguide width of $200\mu m$, the sensitivity is maximized. The corresponding total loss and equivalent path length are 7.4dB and 3.5cm, respectively.

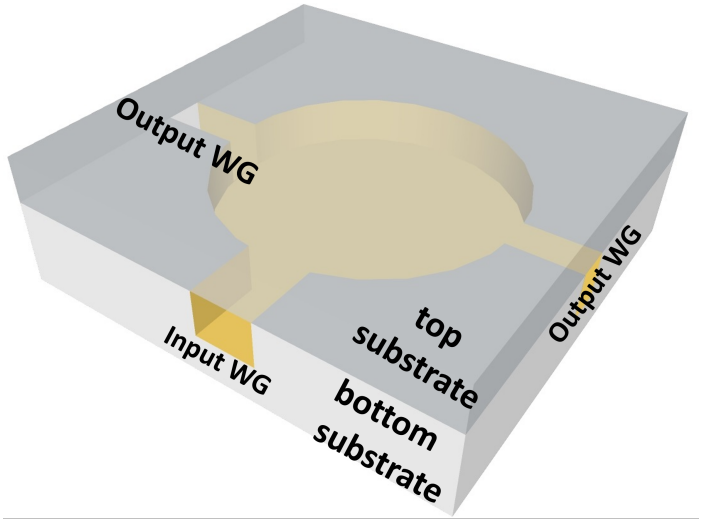

Figure 3.10: Schematic of the integrating cylinder.

3.5.2 Optical source and detectors

For the integrating cylinder, the same off-the-shelf LED and photodiode bare chips can be used as source and detectors. The same processing procedures can be applied to integrate the LED/photodiodes on-chip, therefore, the coupling efficiencies for the source and detector are the same (also see Chapter 5).

3.6 Comparison

In the above sections, the three approaches to implement the on-chip NDIR CO_2 sensor have been introduced, and the waveguide losses and the source/detector coupling efficiencies have been investigated by numerical simulations. In what follows, the three approaches will be compared in terms of power budget considerations, fabrication complexity, and the envisioned cost of the sensor. Finally the optimal approach will be chosen for further exploration in the following chapters.

3.6.1 Power budget considerations

In this section, we will calculate the power budget for the three sensor configurations, using the parameters extracted from optical simulations. We assume a 50ppm detection limit for the sensor, which is similar to most of the state-of-the-art commercial sensors as introduced in section 1.3. A few remarks for the power budget calculations:

1. In the calculation we do not consider the additional noise produced by the electronic read-out circuitry, but limit the power budget to the optical link.

2. The absorption coefficient of 50ppm CO_2 is averaged over the absorption band ($4.2 - 4.35\mu m$) according to the Hitran database [24].

3. For the multi-slot waveguide approach, both a transfer-printable mid-IR LED and a waveguide-integrated thermal source will be considered as the optical source. While for the hollow waveguide and integrating cylinder approaches, a LED bare chip which can be flip-chip bonded on the silicon substrate is considered.

4. The noise equivalent power (or NEP, see Chapter 5) of the thermopile detector used in the multi-slot waveguide approach is calculated according to a state-of-the-art thermopile detector (MLX 90632, from Melexis). The NEP of the photodiode detector is calculated using the normalized detectivity D^* of a high-performance photodiode (PD42BS, from Mid-IR Diode Optopair Group) with a sensitive area S using the following formula:

$$NEP = \frac{\sqrt{S}}{D^*} \tag{3.6}$$

5. As the propagation loss of the multi-slot waveguide is dominated by the fabrication process (sidewall roughness), an exact value of the propagation loss is not available at the moment. We assume a 2 dB/cm propagation loss for the multi-slot waveguide, which is obtained from [25].

6. For the integrating cylinder, the propagation loss is calculated by dividing the total loss w.r.t the effective path length (further elaborated in Chapter 4).

7. The optimal waveguide length (1/e transmission) is determined by Eq. 2.8.

8. Other parameters such as propagation loss of the hollow waveguide, confinement factor in air, and source/detector coupling efficiencies are all obtained from the numerical simulations as discussed in the previous sections.

The power budget calculation yields the required source power such that a change in the transmitted power due to 50ppm CO_2 concentration change is three times larger than the noise produced in the detector. Table 3.2 shows the power budget calculation for the three proposed sensor configurations.

It can be seen that in terms of power budget, the hollow waveguide and the integrating cylinder are the most attractive approaches, the required source power for those two options are nearly identical, about $3.3\mu W$. This level of output power from a mid-IR LED is achievable, as the typical power for a LED bare chip

	Multi-slot WG (LED/thermal)	Hollow WG	Integrating cylinder	unit
Noise equivalent power of detector	0.25	0.01	0.01	$nW/\sqrt{Hz}$
Integration time	1	1	1	s
Min detectable power change (3NEP)	0.75	0.03	0.03	nW
Required resolution	50	50	50	ppm
Absorption coefficient for 50ppm CO_2 averaged over $4.2-4.35\mu m$	1.2e-3	1.2e-3	1.2e-3	cm^{-1}
WG propagation loss	2.0	2.3	2.2	dB/cm
Optimal WG length (1/e transmission)	2.2	1.9	3.5	cm
WG transition loss	3	-	-	dB
Total loss	10.35	4.35	7.4	dB
Transmission of sensing path	0.1	0.37	0.18	-
Confinement factor in air	0.6	1.0	1.0	-
Effective path length	1.3	1.9	3.5	cm
Absorbance of CO_2 over L_{eff} (50ppm)	1.6e-3	2.3e-3	4.2e-3	-
Source coupling efficiency	0.1/0.3	0.08	0.08	-
Detector coupling efficiency	1.0	0.43	0.43	-
Required power in $4.2-4.35\mu m$ range	46.8/15.6	1.0	1.1	μW
Estimated fraction of source power in $4.2-4.35\mu m$ range	0.3/0.04	0.3	0.3	-
Required source output power	156/390	3.3	3.7	μW

Table 3.2: Power budget breakdown for the three sensor configurations.

is about[4] $10\mu W$ when the LED works in quasi-CW mode (50% duty cycle). And the output peak power can be $20\times$ larger when pulsed mode (0.1% duty cycle)

[4]LED43 from IBSG: http://www.ibsg-st-petersburg.com/

is used, which gives a larger margin for the additional noise introduced by the electronic read-out circuits. On the other hand, the multi-slot waveguide approach requires a much larger ($50\times$ or $100\times$) source power to achieve the same limit of detection.

3.6.2 Fabrication complexity and footprint

As we are targeting a miniaturized gas sensor that can be manufactured in a large volume with low cost, the fabrication complexity of the sensor is of paramount importance. Wafer-level fabrication of the sensor using CMOS/MEMS compatible technologies will finally yield low cost sensors. In this respect, we rule out the multi-slot waveguide approach as the slots and beams of the multi-slot waveguide require very high aspect ratio etching which is difficult to yield. Moreover, stiction between the silicon beams of the multi-slot waveguide has been observed during the removal of the SiO_2 layer [25], which limits the fabrication yield. The hollow waveguide-based sensor and the integrating cylinder-based sensor rival each other in terms of fabrication complexity. The fabrication process involves optical lithography, deep reactive ion etching of silicon, metal deposition, and wafer bonding, which are all wafer-level processes that have been well-developed and widely applied in the semiconductor industry. However, the footprint of the sensor implemented with the integrating cylinder is smaller than that of the hollow waveguide, as the latter requires large waveguide bends to fit cm-long waveguide on a small chip area. Therefore, the integrating cylinder approach is now chosen as the optimal approach to realize an on-chip CO_2 sensor and will be explored further in the following chapters.

3.7 Conclusion

In this chapter, the system-level sensor configuration was firstly introduced, a dual-path configuration is chosen in which the reference path is used to mitigate the measurement errors due to common noise sources such as source power fluctuations and waveguide aging. Then we gave an overview of the three sensor configurations proposed in this thesis work: sensors based on a multi-slot waveguide, a metallic hollow waveguide, and a metallic integrating cylinder. We explored the design considerations and some key aspects of the three approaches such as waveguide loss and source/detector coupling efficiencies via numerical simulations. The simulation results were used for power budget calculations to determine the required optical power at the source side. The power budget calculations reveal that the hollow waveguide approach and the integrating cylinder approach require similar output power from the mid-IR LED, while the required source power for the multi-slot waveguide approach is much higher because of the assumed use of a

Si thermopile detector or bolometer. In addition, the complex fabrication of the multi-slot waveguide makes it not practical to realize a low-cost sensor with high yield. On the other hand, both the hollow waveguide and the integrating cylinder can be fabricated on wafer level, giving them the potential for mass production at low cost. In terms of the footprint of the sensor, the sensor based on integrating cylinder is smaller than the sensor based on hollow waveguide. Based on the above-mentioned reasons, **the integrating cylinder approach is now chosen as the optimal approach to realize a compact and low-cost CO_2 sensor, and it will be further discussed in the following chapters.**

References

[1] Eva Ryckeboer, Ronny Bockstaele, Michal Vanslembrouck, and Roel Baets. *Glucose sensing by waveguide-based absorption spectroscopy on a silicon chip*. Biomedical optics express, 5(5):1636–1648, 2014.

[2] Vilson R Almeida, Qianfan Xu, Carlos A Barrios, and Michal Lipson. *Guiding and confining light in void nanostructure*. Optics letters, 29(11):1209–1211, 2004.

[3] Muddassir Iqbal, Zheng Zheng, and Jiansheng Liu. *Light confinement in low contrast slot waveguide structures investigated*. In 2008 International Conference on Microwave and Millimeter Wave Technology, volume 2, pages 878–881. IEEE, 2008.

[4] Ralf Siebert and Jörg Müller. *Infrared integrated optical evanescent field sensor for gas analysis: part I: system design*. Sensors and Actuators A: Physical, 119(1):138–149, 2005.

[5] Haishan Sun, Antao Chen, and Larry R Dalton. *Enhanced evanescent confinement in multiple-slot waveguides and its application in biochemical sensing*. IEEE Photonics Journal, 1(1):48–57, 2009.

[6] Iman Khodadad, Nigel Clarke, Mohammadreza Khorasaninejad, Dale Henneke, and Simarjeet S Saini. *Optimization of multiple-slot waveguides for biochemical sensing*. Applied optics, 53(23):5169–5178, 2014.

[7] Edward D Palik. *Handbook of optical constants of solids*, volume 3. Academic press, 1998.

[8] Patrick Ferrand and R Romestain. *Optical losses in porous silicon waveguides in the near-infrared: Effects of scattering*. Applied Physics Letters, 77(22):3535–3537, 2000.

[9] MK Haigh, GR Nash, SJ Smith, L Buckle, MT Emeny, and T Ashley. *Mid-infrared Al x In 1- x Sb light-emitting diodes*. Applied physics letters, 90(23):231116, 2007.

[10] Andreas De Groote, JD Peters, ML Davenport, MJR Heck, Roel Baets, Günther Roelkens, and JE Bowers. *Heterogeneously integrated III–V-on-silicon multibandgap superluminescent light-emitting diode with 290 nm optical bandwidth*. Optics letters, 39(16):4784–4787, 2014.

[11] SK Tripathy. *Refractive indices of semiconductors from energy gaps*. Optical materials, 46:240–246, 2015.

[12] Sadao Adachi. *Optical dispersion relations for GaP, GaAs, GaSb, InP, InAs, InSb, Al x Ga1- x As, and In1- x Ga x As y P1- y*. Journal of Applied Physics, 66(12):6030–6040, 1989.

[13] Wei Cao, Ali Z Khokhar, Goran Z Mashanovich, Otto L Muskens, Milos Nedeljkovic, Ahmed M Osman, Jordi Soler Penades, Zhibo Qu, and Yangbo Wu. *Mid-Infrared Silicon Waveguide-Based Bolometer*. In 2019 IEEE 16th International Conference on Group IV Photonics (GFP), volume 1949, pages 1–2. IEEE, 2019.

[14] Enrique AJ Marcatili and RA Schmeltzer. *Hollow metallic and dielectric waveguides for long distance optical transmission and lasers*. Bell System Technical Journal, 43(4):1783–1809, 1964.

[15] James A Harrington. *A review of IR transmitting, hollow waveguides*. Fiber & Integrated Optics, 19(3):211–227, 2000.

[16] Mitsunobu Miyagi and Shojiro Kawakami. *Design theory of dielectric-coated circular metallic waveguides for infrared transmission*. Journal of Lightwave Technology, 2(2):116–126, 1984.

[17] Jinming Wang, Shuangxi Xing, Haofeng Wang, Yan Wang, Wei Wang, Hui Suo, and Chun Zhao. *Design and fabrication of gas sensing hollow core waveguides in near infrared*. Optics Communications, 285(5):621–624, 2012.

[18] Michael Bass et al. *Handbook of optics.* McGraw-Hill,, 2000.

[19] Shaista Babar and JH Weaver. *Optical constants of Cu, Ag, and Au revisited*. Applied Optics, 54(3):477–481, 2015.

[20] Aleksandar D Rakić. *Algorithm for the determination of intrinsic optical constants of metal films: application to aluminum*. Applied optics, 34(22):4755–4767, 1995.

[21] Eamonn Hawe, Elfed Lewis, and Colin Fitzpatrick. *Hazardous gas detection with an integrating sphere in the near-infrared*. In J. Phys. Conf. Ser., volume 15, pages 250–255, 2005.

[22] E Hawe, C Fitzpatrick, P Chambers, G Dooly, and E Lewis. *Hazardous gas detection using an integrating sphere as a multipass gas absorption cell*. Sensors and Actuators A: Physical, 141(2):414–421, 2008.

[23] E Hawe, P Chambers, C Fitzpatrick, and E Lewis. *CO2 monitoring and detection using an integrating sphere as a multipass absorption cell*. Measurement Science and Technology, 18(10):3187, 2007.

[24] Laurence S Rothman, Iouli E Gordon, Yury Babikov, Alain Barbe, D Chris Benner, Peter F Bernath, Manfred Birk, Luca Bizzocchi, Vincent Boudon, Linda R Brown, et al. *The HITRAN2012 molecular spectroscopic database*. Journal of Quantitative Spectroscopy and Radiative Transfer, 130:4–50, 2013.

[25] Ralf Siebert and Jörg Müller. *Infrared integrated optical evanescent field sensor for gas analysis: Part II. Fabrication*. Sensors and Actuators A: Physical, 119(2):584–592, 2005.

4

On-Chip CO_2 Sensing Based on Integrating Cylinder

In Chapter 3, the optimal approach to realize an on-chip CO_2 sensor has been chosen, namely the sensor based on an integrating cylinder. The goal of this chapter is to provide a comprehensive analysis of the integrating cylinder. First, a theoretical analysis is given, followed by detailed numerical simulations regarding the total transmission loss, equivalent optical path length, and the response time. The design parameters are then optimized by maximizing the sensitivity of the integrating cylinder with 3D ray tracing simulations. The fabrication process of the integrating cylinder will be discussed in detail, together with the proof-of-concept experimental results of CO_2 sensing. This chapter is based on our published article [1], with proper extension and supplement.

4.1 Introduction

The concept of the integrating cylinder is inspired by the integrating sphere. In an integrating sphere, the incident light is diffusely reflected by the coatings on the inner walls of the sphere, leading to a uniform intensity distribution within the sphere. Therefore the power collected by the detector does not depend on the relative positions of the source and the detector provided there is no substantial direct light path between the source and detector. As the incident light experiences multiple reflections before it reaches the detector, the optical path length is effectively

enhanced. The average path length travelled by a photon within the integrating sphere is given by:

$$L_{eff} = \frac{2}{3} \cdot M \cdot D \tag{4.1}$$

with D being the diameter of the sphere, which is typically on the order of a few centimeters. M is the sphere multiplier, which accounts for the enhancement of the optical path length due to multiple reflections inside the sphere [2]. The multiplier M can be calculated by the following equation:

$$M = \frac{\rho}{1 - \rho(1 - f)} \tag{4.2}$$

where ρ is the reflectance of the sphere's internal surface, and f is the port fraction, which is the ratio of the area of the port openings to the total internal surface area. It can be seen that to increase the optical path length for a given sphere with a certain diameter, the reflectance ρ of the inner surface has to be high and the port fraction f has to be small. It has been demonstrated that the multiplier M can be as high as 50 for a standard integrating sphere (diameter = 5cm) with 98% inner surface reflectance, and the effective path length can exceed two meters [3]. Due to this very long optical path length, the integrating sphere is ideal for gas sensing applications, especially for gas species with low absorption coefficients such as CO and NO_2. Optical sensing of various gas species have been demonstrated using an integrating sphere, with the optical path length ranging from 40cm to 5m [4–7].
The concept of the integrating sphere has been taken into the silicon photonics world to realize a 2D integrating cell with a long path length on a small chip area [8]. The integrating cell is implemented on the SOI platform, where high-reflectivity mirrors based on photonic crystals are used to confine the guided mode in the silicon slab. In the 2D integrating cell, the propagation of the slab mode follows a random path and experiences multiple reflections before escaping from the cell, just as in the 3D integrating sphere. An optical path length of 25cm is achieved on a chip area of $\sim 10mm^2$, due to the high reflectivity ($> 99\%$) of the photonic crystal mirrors. Such a 2D integrating cell can be used for evanescent gas sensing, however, the effective interaction length between the slab mode and the ambient can be significantly smaller due to the high confinement of the slab mode. Moreover, the fabrication of the high-quality photonic crystal mirrors requires E-beam lithography, which hinders the application of the integrating cell in the low-cost gas sensing market.
In this chapter, we will take the concept of the 2D integrating cell a step further, by using a hollow metallic cylinder as the wave/light guide. In the integrating cylinder, the light is confined in the cylinder by the highly reflective mirrors coated on the inner surfaces. The hollow cylinder enables a total ($\Gamma = 1$) interaction between the guided light and the absorbing medium (eg. CO_2 gas), hence the effective interaction length is not compromised. Furthermore, the integrating cylinder can be

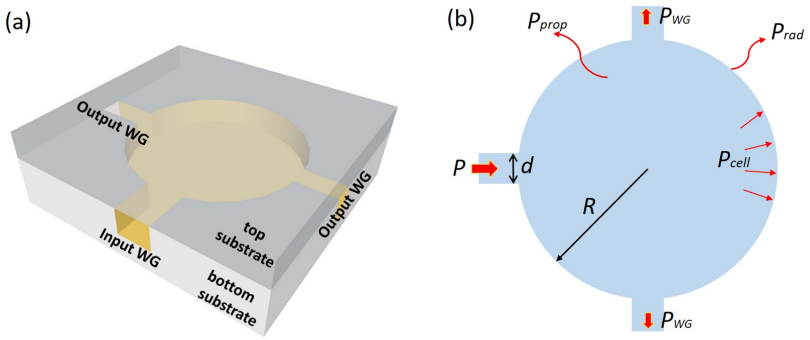

Figure 4.1: (a) 3D schematic of the integrating cylinder with access waveguides. The integrating cylinder is formed by wafer bonding of two silicon substrates. (b) 2D analysis of the integrating cylinder, with R being the radius of the circle and d being the width of all access waveguides. P is the input power, P_{WG}, P_{rad} and P_{prop} are the power coupled to the output waveguides, the power absorbed/radiated at the cavity sidewall, and the power lost during propagation in the cavity, respectively.

fabricated using wafer-level processes such as deep reactive ion etching and wafer bonding, which gives the advantage of potential high-volume production with low cost.

4.2 Theoretical analysis

Figure 4.1(a) shows a 3D schematic of the integrating cylinder, which consists of a hollow metallic cylindrical cavity with one input waveguide and two output waveguides. To confine the light in the cavity, a thin layer of gold is coated on the inner surfaces to form the high-reflectivity mirrors. The incident light is launched into the integrating cylinder from the input waveguide and it is extracted from the output waveguides. The two output waveguides can act as the sensing path and the reference path with the addition of two external optical filters. Similar to an integrating sphere, the incident light experiences multiple reflections in the cavity, leading to a long effective path length. For the analysis of the integrating cylinder, we assume the incident light is randomly reflected on the sidewall, which can be achieved by deliberately applying a random roughness on the sidewalls. Since the incident light is just specularly reflected on the parallel top and bottom surfaces (coated with gold), we can reduce the analysis of the integrating cylinder from 3D to 2D, as shown in Figure 4.1(b). With the assumption that the light incident on the sidewall is randomly reflected, the average path length of the light beam between

two consecutive reflections on the circle, is given by [9]:

$$L_{avg} = \frac{4}{\pi} \cdot R \tag{4.3}$$

where R is the radius of the circle. When incident light with power P is launched into the integrating cylinder from the input waveguide, it can be "lost" through three mechanisms: (1) extraction loss from the access waveguides (P_{WG}); (2) radiation/absorption loss upon incidence on the sidewalls (P_{rad}); (3) propagation loss in the cavity slab (P_{prop}). At steady state, the energy in the cavity is uniformly distributed. When we define the optical power incident on the sidewall as P_{cell}, the three loss mechanisms can be described by [8]:

$$P_{WG} = \beta P_{cell} \tag{4.4}$$

$$P_{rad} = \gamma P_{cell} \tag{4.5}$$

$$P_{prop} = \eta P_{cell} \tag{4.6}$$

with β being the extraction coefficient for each of the waveguides, and it's given by the ratio of the waveguide width (d) and the circumference of the circle:

$$\beta = \frac{d}{2\pi R} \tag{4.7}$$

γ is the fraction of power radiated/absorbed at the sidewall, and it is related to the reflectivity ρ of the sidewall mirror by:

$$\gamma = 1 - \rho \tag{4.8}$$

η is the loss factor of the light propagating in the cavity slab between two consecutive reflections on the sidewalls. It is either due to the waveguide loss α_{prop}, or due to the CO_2 absorption, characterized by the absorption coefficient α_{CO2}. η can be written as:

$$\begin{aligned} \eta &= 1 - \exp(-L_{avg}(\alpha_{prop} + \alpha_{CO_2})) \\ &\approx L_{avg}(\alpha_{prop} + \alpha_{CO2}) \end{aligned} \tag{4.9}$$

The summation of all losses equals the input power because of energy conservation:

$$P = 3P_{WG} + P_{prop} + P_{rad} \tag{4.10}$$

The fraction of power coupled to the waveguide P_{WG} can thus be related to the input power P using equations (4.4)–(4.6) and equation (4.10):

$$P_{WG} = \frac{\beta}{3\beta + \gamma + \eta} P \tag{4.11}$$

The transmission from the input waveguide to one of the output waveguides can therefore be calculated by:

$$\begin{aligned} T &= \frac{P_{WG}}{P} = \frac{\beta}{3\beta+\gamma+\eta} \\ &= \frac{\beta}{3\beta+1-\rho+\frac{4}{\pi}R(\alpha_{prop}+\alpha_{CO2})} \end{aligned} \tag{4.12}$$

The term $\frac{4}{\pi}R$ is the average distance between two consecutive reflections, as shown in Equation 4.3.

The sensitivity S of the integrating cylinder is defined as the transmission change induced by CO_2 absorption, and it is can be obtained by taking the partial derivative of the transmission T w.r.t α_{CO_2}:

$$S = -\frac{\partial T}{\partial \alpha_{CO_2}} = \frac{\frac{2}{\pi}\beta R}{(3\beta+1-\rho+\frac{4}{\pi}R(\alpha_{prop}+\alpha_{CO_2}))^2} \tag{4.13}$$

The sensitivity S can be maximized as a function of R (assuming a fixed β) when

$$3\beta + 1 - \rho = \frac{4}{\pi}R(\alpha_{prop} + \alpha_{CO_2}) \tag{4.14}$$

In Eq. 4.14, the term on the left-hand side can be considered as the "extraction" from the integrating cylinder, which consists of extraction by the access waveguides and the radiation/absorption loss from the sidewalls as the reflectivity ρ is less than 1. The term on the right-hand side is the absorption in the integrating cylinder, which consists of waveguide loss and CO_2 absorption loss. It can be seen from equation 4.13 that the integrating cylinder is most sensitive when the "extraction" equals "absorption", i.e., when critical coupling occurs inside the cavity. The optimal radius can be calculated by solving equation 4.14, which gives:

$$R_{opt} = \frac{3\beta + 1 - \rho}{\frac{4}{\pi}(\alpha_{prop} + \alpha_{CO_2})} \tag{4.15}$$

Since $1 - \rho << 3\beta$ in our design (β is of the order 0.03, while the reflectivity ρ is about 0.995 [10]), by substituting equation 4.15 into equation 4.12 we find the total transmission loss from the input to the output at optimal radius:

$$\begin{aligned} Loss(dB) &= -10\log T \\ &= -10\log(\tfrac{\beta}{2(3\beta+1-\rho)}) \\ &\approx 10\log 6 \\ &= 7.8dB \end{aligned} \tag{4.16}$$

One can see that the total transmission loss is constant (7.8 dB) at the optimal cylinder radius. This is because at critical coupling, "absorption" equals "extraction", adding 3dB to the loss, and in the "extraction" part, power is equally coupled into 3 access waveguides, which gives another 4.8dB loss (33%), so the

total transmission loss is 7.8 dB at the optimal radius. In order to calculate the equivalent optical path length, i.e., the effective path length of the beam from the input waveguide to the output waveguide, we write the transmission from the input to the output with/without CO_2 as:

$$\begin{array}{lcl} T_{prop+CO_2} & = & \frac{1}{3}\exp(-(\alpha_{prop}+\alpha_{CO_2})L_{eq}) \\ T_{prop} & = & \frac{1}{3}\exp(-\alpha_{prop}L_{eq}) \end{array} \tag{4.17}$$

The factor $\frac{1}{3}$ is because the extracted power is equally coupled into 3 access waveguides. We take the ratio on both sides of Equation (4.17), and since $\alpha_{CO_2}L_{eq} << 1$, in first order approximation:

$$\begin{array}{lcl} \frac{T_{prop+CO_2}}{T_{prop}} & = & \exp(-\alpha_{CO_2}L_{eq}) \\ & \approx & 1-\alpha_{CO_2}L_{eq} \end{array} \tag{4.18}$$

On the other hand, $\frac{T_{prop+CO_2}}{T_{prop}}$ can be also calculated from Equation (4.12),

$$\frac{T_{prop+CO_2}}{T_{prop}} = \frac{3\beta+1-\rho+\frac{4}{\pi}R\alpha_{prop}}{3\beta+1-\rho+\frac{4}{\pi}R(\alpha_{prop}+\alpha_{CO2})} \tag{4.19}$$

The equivalent path length L_{eq} can thus be calculated by equating Equations (4.18) and (4.19):

$$L_{eq} = \frac{\frac{4}{\pi}R}{3\beta+1-\rho+\frac{4}{\pi}R(\alpha_{prop}+\alpha_{CO_2})} \tag{4.20}$$

We notice that the numerator is the average path length between two consecutive reflections given by Equation (4.3), and the denominator is the summation of the coefficients of all losses. We substitute Equation (4.15) into Equation (4.20) and we can calculate the equivalent path length at optimal radius:

$$L_{eq,opt} = \frac{1}{2(\alpha_{prop}+\alpha_{CO_2})} \tag{4.21}$$

4.3 Simulations

As the dimensions of the integrating cylinder ($\sim 300\mu m$ in height) is much larger than a wavelength ($\sim 4\mu m$), we can use ray tracing to simulate the integrating cylinder. A commercial ray tracing software *OpticStudio* capable of doing 3D ray tracing is used. In the simulation, we use the non-sequential system module of *OpticStudio* since it allows multiple reflections to be accounted at a certain interface.

4.3.1 Total loss

In OpticStudio, a cylindrical cavity with three access waveguides (one input and two outputs) is constructed. We fix the height of the cylinder and the waveguides at $300\mu m$, which is also the etch depth of the silicon wafer when the device is being fabricated. The lengths of the access waveguides are 1mm and they have equal widths d. A gold coating is applied on the inner surfaces of the cavity and the waveguides to model the reflective mirrors. An isotropic point source emitting un-polarized monochromatic light at $4.26\mu m$ is placed at the center of the input waveguide, and two rectangular detectors are placed at the input waveguide (D_1) and one of the output waveguides (D_2). Figure 4.2(a) shows a 2D schematic of the simulation setup. A total number of 100,000 rays carrying a total power of P_0 is launched from the point source into the input waveguide, with the energy equally distributed in each ray. To model the random reflections of the incident light on the sidewalls, we implemented a Lambertian scatterer on the sidewall of the cavity. The probability of the directions of the reflected light follows a Lambertian distribution, and the reflectance on the sidewalls is determined by the incident angle of the light. In the simulation, the power at the two detectors are recorded as P_1 and P_2, and the propagation loss from the input waveguide to the output waveguide can be calculated by:

$$\text{Total loss [dB]} = -10 \cdot \log(\frac{P_2}{P_1}) \tag{4.22}$$

Figure 4.2(b) shows the total transmission loss from the input waveguide to the output waveguide for various cylinder radii (R) and access waveguide widths d. It can be seen that the total loss increases as the cylinder radius increases or as the access waveguide width decreases. This dependency stems from the fact that light is trapped in the cylinder for a longer time and experiences more reflections, and the reflection losses from each reflection accumulate to give an overall larger transmission loss.

4.3.2 Equivalent path length

The equivalent path length is the average path length the incident light experiences from the input waveguide to the output waveguide. To simulate the equivalent path length of the integrating cylinder, we applied a volume absorbing medium with an absorption coefficient α_{CO_2} in the cavity. Two simulations with/without the absorbing medium need to be executed to determine the equivalent path length L_{eq}, which can be obtained from Eq. 4.18:

$$L_{eq}(cm) = -\ln \frac{T_{prop+CO_2}}{T_{prop}} / \alpha_{CO_2} \tag{4.23}$$

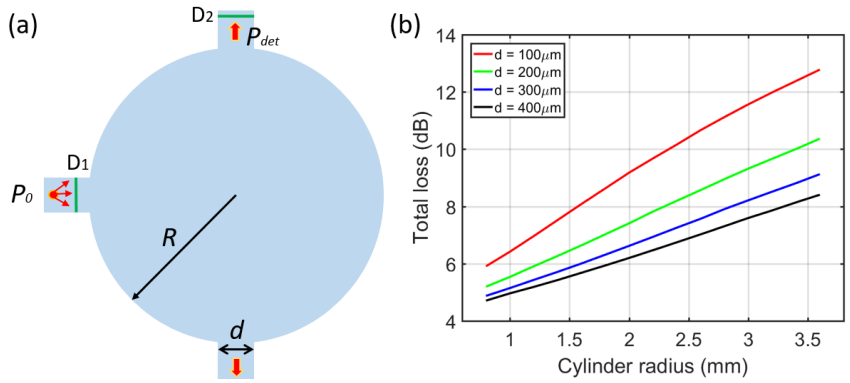

Figure 4.2: (a) 2D schematic of the simulation setup. An isotropic source is used to launch the rays, and two detectors are placed at the input/output waveguides to calculate the transmission. (b) Total transmission loss from the input waveguide to the output waveguide for various cylinder radius and waveguide width combinations.

with $T_{prop+CO_2}$ and T_{prop} being the transmission (P_2/P_1) from the input waveguide to the output waveguide with/without the absorbing medium, respectively.

The simulated equivalent path length for various cylinder radius and waveguide width combinations is shown in Figure 4.3. One can see that the equivalent path length follows the same trends as the total loss, as the same argument applies when the cylinder radius increases or the width of the access waveguide decreases: the incident light stays in the cavity for a longer time and experiences more reflections, leading to a longer path length.

4.3.3 Design optimization

To optimize the design parameters of the integrating cylinder, namely to find a cylinder radius and waveguide width combination for which the sensitivity S (defined as the transmission change for a CO_2 concentration change) is maximized, we plot the sensitivity S for various cylinder radii and access waveguide widths in Figure 4.4. In this simulation, we set the absorption coefficient of the absorbing medium $\alpha_{CO_2} = 0.03/cm$, which is equivalent to the absorption of 1000ppm CO_2 averaged over $4.2-4.35\mu m$. It can be seen that for a certain waveguide width d, the sensitivity S first increases and then decreases as the cylinder radius R is increased. We define the optimal radius R_{opt} as the cylinder radius when the sensitivity S is maximized. The optimal radii for different access waveguide widths is summarized in Table 4.1.

We can see from Table 4.1 that the total transmission loss as well as the equivalent path length are almost constant at the optimal cylinder radius, which agrees with theory. For an integrating cylinder with a radius $R = 2mm$ and an access

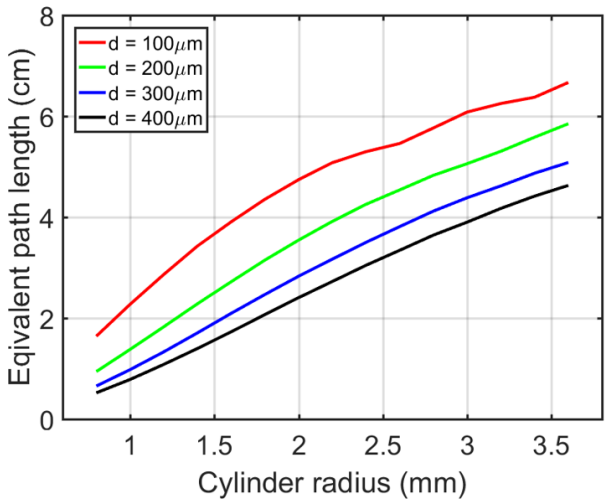

Figure 4.3: Equivalent path length from the input waveguide to the output waveguide for various cylinder radius and waveguide width combinations.

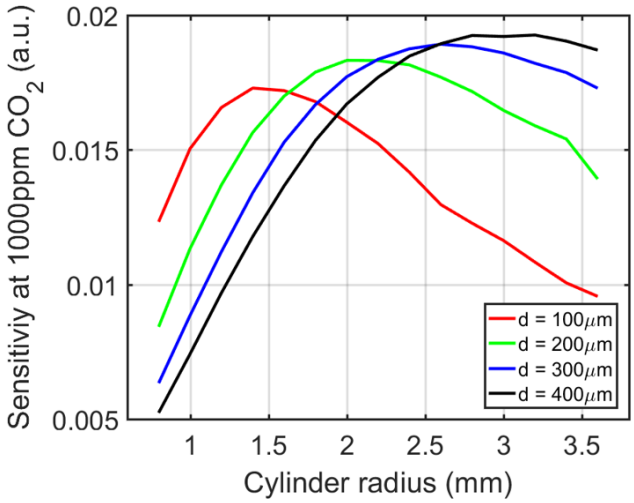

Figure 4.4: Sensitivity (in absorbance unit, or AU) due to the absorption of 1000 *ppm CO_2, for various cylinder radius and access waveguide width combinations.*

d [μm]	R_{opt} [mm]	TL [dB]	L_{eq} [cm]
100	1.4	7.5	3.4
200	2.0	7.4	3.5
300	2.6	7.6	3.8
400	3.0	7.6	3.9

Table 4.1: Optimal cylinder radius and access waveguide width combinations, and the corresponding equivalent path length and total transmission loss.

waveguide width $d = 200\mu m$, the equivalent path length is about 3.5 cm, and the total transmission loss from the input waveguide to the output waveguide is about 7.4dB.

4.3.4 Sidewall roughness and source emission pattern

In the simulations presented in previous sections, a lambertian scatterer is applied to model the roughness on the sidewalls. The lambertian angular distribution of the reflected light on the sidewalls is an ideal approximation and the simulation results agree well with the theory. In reality, the sidewall scattering is implemented by deliberately roughening the sidewalls with a random function (as we will see in the next sections), therefore the angular distribution of the directions of the reflected light can be different from a lambertian distribution. To study the angular distribution of the directions of the reflected light over a rough surface, the simulation as shown in Figure 4.5 is performed:

- In the simulation, a parallel beam is incident on a flat surface, the surface is either roughened with a random function, or a lambertian reflector is applied on the surface.
- The amplitude of the roughness on the rough surface is determined by its root-mean-square (rms) value, the correlation length of the roughness is fixed at $30\mu m$.
- A polar detector is used to record the angular distribution of the directions of the reflected light.

The angular distributions of the directions of the reflected light from a rough surface and from a lambertian surface are shown in Figure 4.6. It can be seen that the incident light is reflected into certain discrete directions at a rough surface, while the directions of reflection from a lambertian surface follows a lambertian distribution. Moreover, in the roughened surface case, the angular distributions for smaller ($5\mu m$ and $10\mu m$) roughness amplitudes are 'more lambertian' than larger ($15\mu m$) amplitudes. Although the reflection pattern is not perfectly lambertian, the multiple reflections in the cylinder averages it out a bit. The angular distribu-

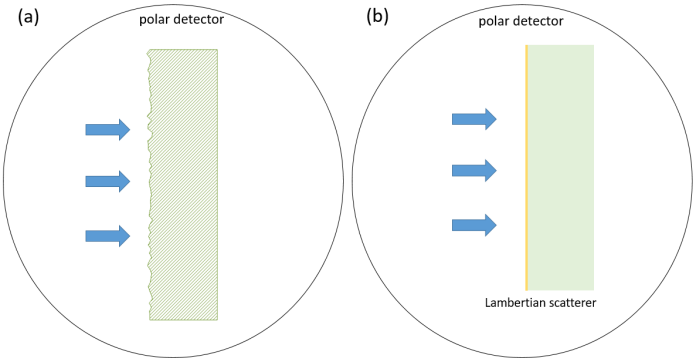

Figure 4.5: Simulation setup to study the angular distributions of the reflected light over (a) a roughened surface; (b) a lambertian surface.

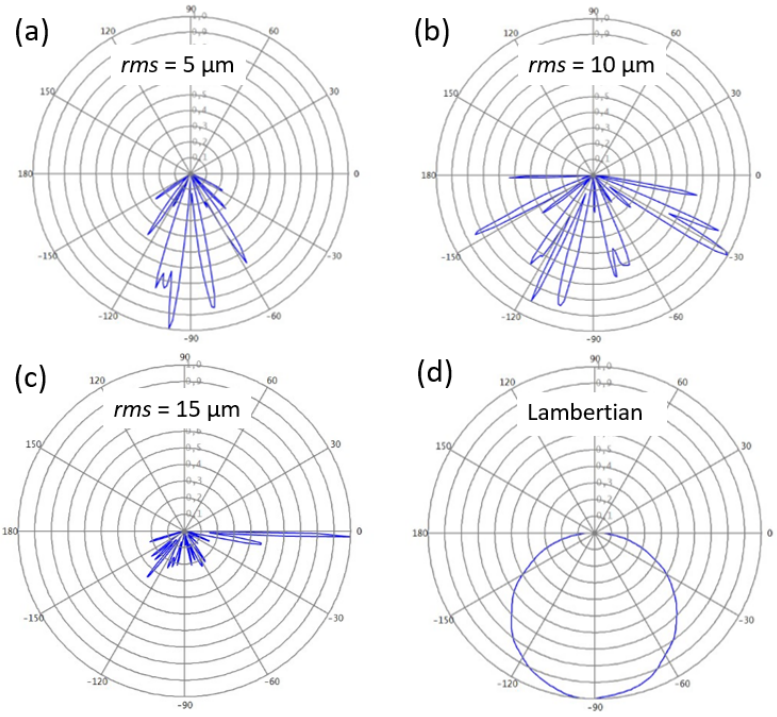

Figure 4.6: (a)-(c) Angular distributions of the directions of the reflected light over a rough surface with various roughness amplitudes. (d) Angular distribution of the directions of the reflected over a lambertian surface.

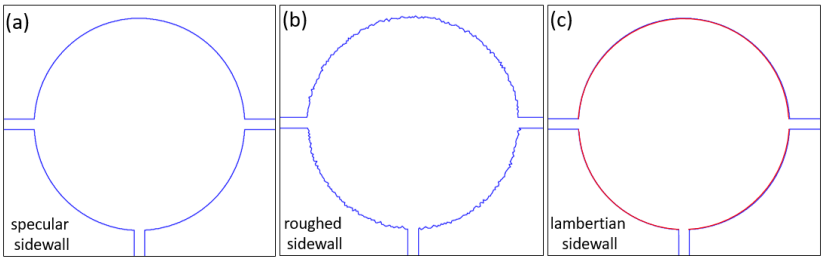

Figure 4.7: Three types of integrating cylinders. (a) A specular cylinder. (b) A roughened cylinder. (c) A lambertian cylinder.

tion of the directions of the reflected light will ultimately influence the propagation loss and the sensitivity of the sensor, as the reflectance at the gold surface is also angle dependent as can be seen in Figure 3.8. To investigate the impact of the angular distribution of the reflected light on the sensitivity of the sensor, three configurations are compared: a specular integrating cylinder, a roughened integrating cylinder, and a lambertian integrating cylinder, as shown in Figure 4.7. In a specular cylinder, no roughness is applied on the sidewalls, therefore the incident light on the sidewalls is reflected specularly. In a roughened cylinder, the sidewalls of the cylinder is deliberately roughened with a random function, yet the incident light is still specularly reflected locally. In a lambertian cylinder, a lambertian scatterer is applied on the sidewalls and the directions of the reflected light follows a lambertian distribution. Another important factor determining the sensitivity is the emission pattern of the light source. Ideally the sensitivity of the sensor should not depend on the emission pattern of the light source, as the emission pattern can change over time which introduces error in the measurement. For instance, in a fully integrated sensor with an on-chip mid-IR LED, the emission pattern from an LED can change with temperature due to the temperature dependence of the refractive indices of the semiconductor materials. In the simulations presented in previous sections, a point source emitting uniformly in a half sphere (i.e. 180° cone) is used. To investigate how the emission pattern of the light source can influence the sensitivity, three types of sources are used for all three cylinder configurations: a uniform point source emitting in a 180° cone, a uniform point source emitting in a 120° cone, and a lambertian point source. The simulated sensitivity of the three types of integrating cylinder for the three types of source emission patterns are shown in Figure 4.8. One can see that the sensitivity of the specular cylinder strongly depends on the emission pattern of the light source, while for the roughened cylinder, the dependence is much smaller. In the lambertian cylinder, although the sensitivity is smaller, there is negligible dependence on the emission pattern of the light source. The reason behind this phenomenon is that the lambertian scatterer on the sidewalls reflects the incident light in all directions, as can be

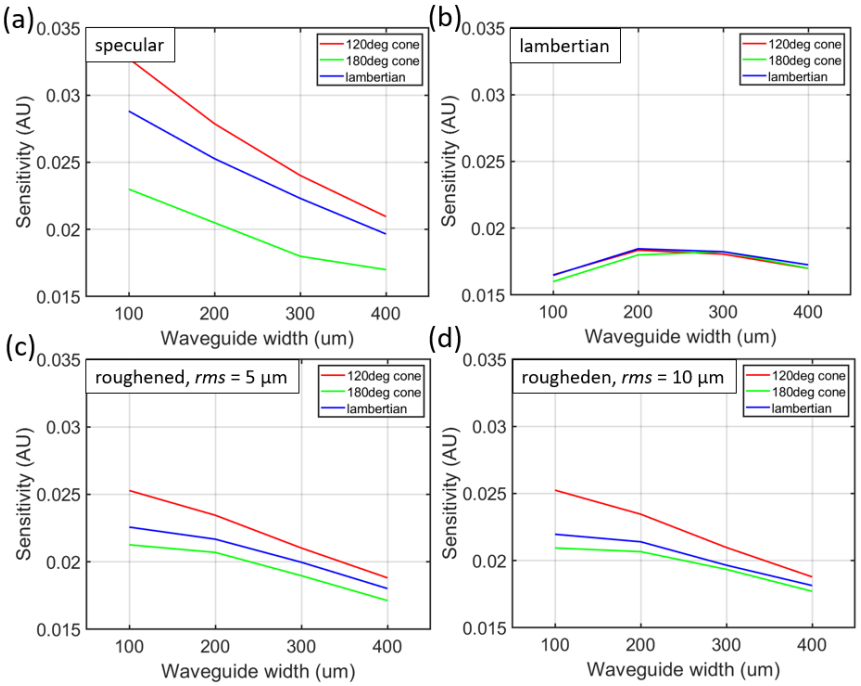

Figure 4.8: Sensitivity of the integrating cylinder for 1000 ppm CO_2. (a) A specular cylinder. (b) A lambertian cylinder. (c) A roughened cylinder with roughness amplitude of $rm = 5\mu m$. (d) A roughened cylinder with roughness amplitude of $rm = 10\mu m$.

seen from Figure 4.6(d). Therefore the optical energy in the cylinder is uniformly distributed, leading to the independence on the source emission patterns. Yet in the specular or roughened cylinder, the incident light is only reflected into one single direction or limited number of directions (as shown in Figure 4.6(a-c)), making the sensitivity less immune to emission pattern variations of the light source. One can also see from Figure 4.8(c) and (d) that in the roughened cylinder case, the emission pattern dependence of the sensitivity is a bit smaller when we change the roughness amplitude from $5\mu m$ to $10\mu m$, due to a 'more lambertian' reflection pattern for a $10\mu m$ roughness amplitude (Figure 4.6(a) and (b)). As discussed earlier, the emission pattern variations of the light source can introduce errors in the measurement. In this regard, the sidewalls of the integrating cylinder should be roughened in a way that the roughness profile produces a 'more lambertian' reflection pattern.

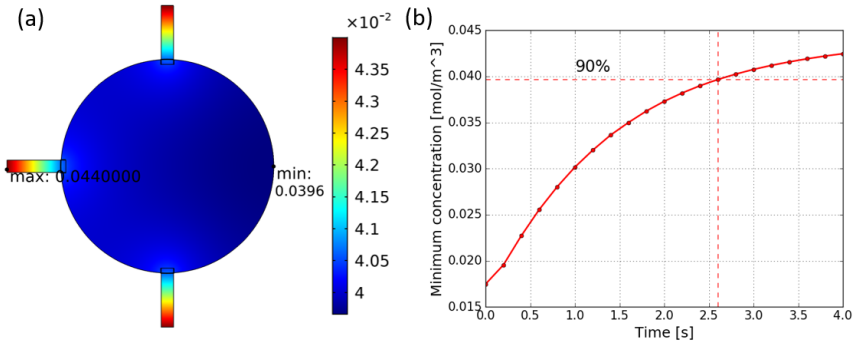

Figure 4.9: (a) CO_2 concentration distribution inside the integrating cylinder at $t = 2.5s$. (b) Time-dependent CO_2 concentration at the right edge of the integrating cylinder.

4.3.5 Response time simulation

The response time of the integrating cylinder is determined by the gas diffusion process, where CO_2 gas has to diffuse from the access waveguides into the cylinder. In many applications, the response time of a sensing system is defined as the time needed to reach 90% of the total response, which can be approximated by the diffusion time at which the minimum concentration in the cylinder reaches 90% of the set concentration. The CO_2 diffusion process inside the integrating cylinder is modeled using a multiphysics solver COMSOL, by numerically solving the diffusion equation:

$$\frac{\partial c}{t} + \nabla \cdot J = R \tag{4.24}$$

in which c is the concentration of the target gas, R is the net source, and J is the total diffusive flux, which can be approximated by Fick's first law [11]: $J = -D\nabla c$, with D being the mass diffusivity of the gas(CO_2 in this case). In this simulation, an integrating cylinder with a radius of $R = 2mm$ and access waveguide width of $d = 200\mu m$ is used. The initial CO_2 concentration inside the cylinder is set to be $0.0176mol/m^3$ ($\sim$ 400 ppm), and three CO_2 sources with a concentration of $0.044mol/m^3$ ($\sim$ 1000 ppm) are placed at the opening of the 3 access waveguides. The diffusivity of CO_2 in air is about $0.16cm^2/s$ (1 atm, 300K) [12]. In the simulation, no convection is activated and the molecular movement is only due to gas diffusion. Figure 4.9(a) shows the CO_2 concentration distribution inside the integrating cylinder at $t = 2.5s$. We can see that the lowest CO_2 concentration appears at the right edge of the cylinder, which is logical as this is the furthest point from the CO_2 sources. The time-dependent CO_2 concentration at this point is depicted in Figure 4.9(b), it can be seen that the time needed for the CO_2 concentration at this point to reach 90% of the source level is approximately 2.6 seconds.

4.4 Device fabrication

The fabrication of the integrating cylinder starts with two blank silicon substrates. The cylindrical cavity with the access waveguides is etched by Deep Reactive Ion Etching (DRIE) on the bottom substrate. Then a thin layer of gold is deposited on both surfaces by sputtering to form the reflective mirrors. Finally, the two substrates are bonded using gold-to-gold direct bonding. The fabrication process flow of the integrating cylinder is depicted in Figure 4.10.

4.4.1 Deep reactive ion etching and sidewall scattering

Deep reactive ion etching (DRIE) is a highly anisotropic etching technique that is widely applied in the semiconductor industry. It is typically used to achieve deep trenches or holes with steep (nearly vertical) sidewalls on silicon wafers. Two major technologies exist to realize DRIE: the cryogenic process [13] and the Bosch process [14]. In the cryogenic process, the substrate is cooled down to a very low temperature ($< -100°$), at which the chemical reaction resulting in isotropic etching is significantly slowed down, while the incoming ions can still bombard and etch the surfaces that are facing the incoming ions. Therefore a very steep sidewall can be obtained with this process. The Bosch DRIE process is also known as the time-multiplexed or pulsed etching process. It utilizes the concurrence of two alternating phases: (1) nearly-isotropic etching phase, which uses ion plasma to etch the substance as in standard reactive ion etching; (2) passivation phase, in which a chemically inert layer is deposited on the substrate. The passivation layer on the sidewalls of the trench/hole protects it from further etching by the ions in the etching phase, while the passivation layer at the bottom of the trench/hole can still be bombarded and sputtered off by the directional ions, thus the bottom of the trench is exposed for further etching. For the DRIE of silicon, source gases such as sulfur hexafluoride (SF_6) and octafluorocyclobutane (C_4F_8) are often used for etching and passivation, respectively [15].
For the fabrication of the integrating cylinder, the Bosch DRIE process is used for

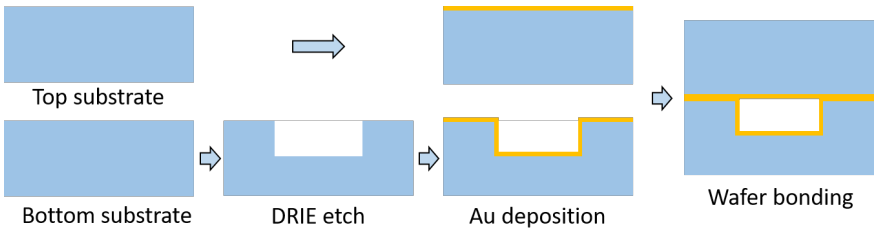

Figure 4.10: Fabrication process flow of the on-chip integrating cylinder.

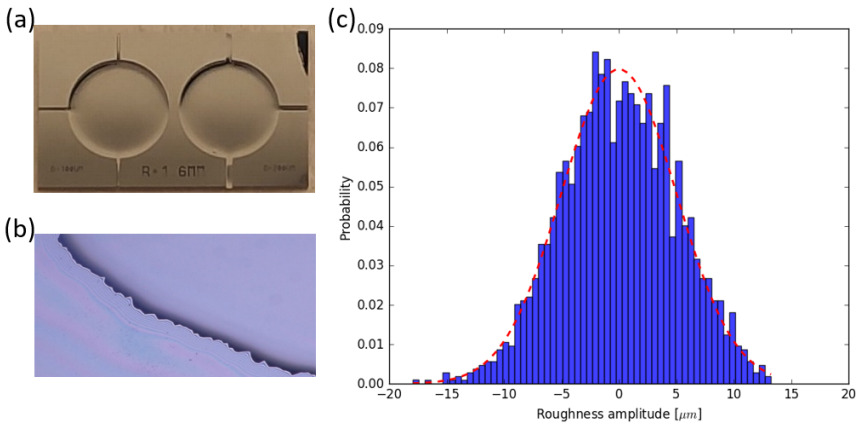

Figure 4.11: (a) Silicon chip after DRIE, the chips consists of two cylinders. (b) Microscope image of the roughness on the sidewalls. (c) Amplitude distribution of the sidewall roughness.

silicon etching. As there is no DRIE tool in our research group, the DRIE of the silicon wafers is outsourced to *Vmicro*[1] in France. The silicon substrate consisting of two integrating cylinders after dicing is shown in Figure 4.11(a). The thickness of the silicon substrate is $750\mu m$ and we choose an etching depth of $300\mu m$ to provide enough rigidity. The roughness of the sidewalls after etching is about 160nm, which is much smaller ($< \frac{\lambda}{10}$) than a wavelength ($4.26\mu m$), therefore the incident light can be considered specularly reflected in the access waveguides.

On the sidewalls of the integrating cylinder, we deliberately roughen the sidewalls to scatter the incident light randomly in the cylindrical cavity, the roughness is implemented during lithography mask design. A microscope image of the roughness on the sidewall can be seen in Figure 4.11(b). Figure 4.11(c) shows the amplitude distribution of the roughness function, the amplitude of the roughness has a Gaussian distribution, with a root-mean-square (rms) value of $\sim 5\mu m$, the correlation length of the roughness is about $50\mu m$.

4.4.2 Gold deposition

Thermal evaporation and sputtering deposition are two common techniques that can be used to deposit high-quality metal films on a substrate. In this work we use sputtering deposition as it provides better step coverage for the vertical sidewalls of the integrating cylinder and the access waveguides. To determine the minimum thickness of the gold coating on the sidewalls, a 3D ray tracing simulation on the propagation loss of the hollow waveguide ($300\mu m \times 300\mu m$) is performed. The

[1] https://vmicro.fr/

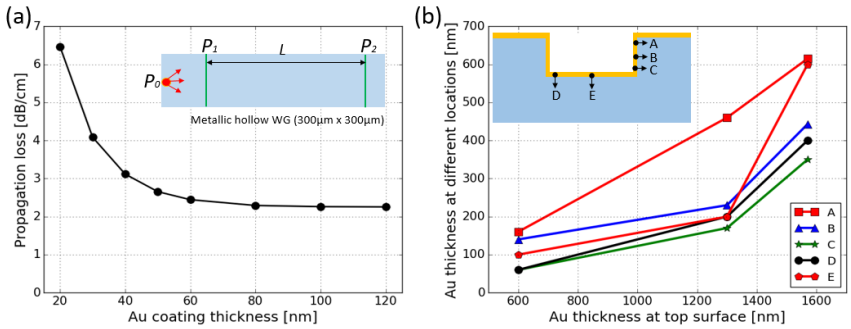

Figure 4.12: (a) Propagation loss of the hollow waveguide at $4.26\mu m$ as a function of the gold coating thickness on the sidewalls. (b) Thickness of gold at different locations of the hollow waveguide in the gold sputtering test.

simulation setup is similar with the one in section 3.4.1. An isotropic point source is used in the simulation and the propagation loss is calculated against the thickness of the gold coating, shown in Figure 4.12(a). It can be seen that in order to provide a high reflectivity, the thickness of the gold film on the sidewalls of the hollow waveguide should be at least 80nm. To determine the minimum thickness of gold that needs to be sputtered, we did several gold sputtering tests (using Univex 450, from Leybold) with a hollow waveguide that is $300\mu m \times 300\mu m$. In each sputtering test, the thicknesses of gold at 5 locations of the waveguide are measured, as shown in Figure 4.12(b). We see that the thicknesses of gold on the sidewalls are substantially smaller than the thickness on the top surface. The minimal thickness of the sputtered gold needs to be $\sim$700nm for the sidewalls to be covered with thick enough gold (80nm). Therefore, for the gold deposition of the integrating cylinder, we choose the thickness of Ti/Au (Ti for better adhesion) to be 50nm/$1\mu m$ to make sure that the gold film can function as a high-relectivity mirror.

4.4.3 Wafer bonding

Various wafer bonding techniques have been explored in both academia and industry, including thermo-compression bonding [16], solder bonding [17], eutectic bonding [18], and anodic bonding [19]. A comprehensive review of wafer bonding techniques can be found elsewhere [20, 21]. For the fabrication of the integrating cylinder, we use gold-gold thermo-compression bonding, in which heat and pressure are applied on the two substrates and bonding is achieved by the diffusion of gold atoms. The principal advantage of gold thermo-compression bonding is that it requires relatively low temperatures and pressures to achieve high bonding strength, as gold is highly resistant to oxidation and corrosion [22]. Since the bond-

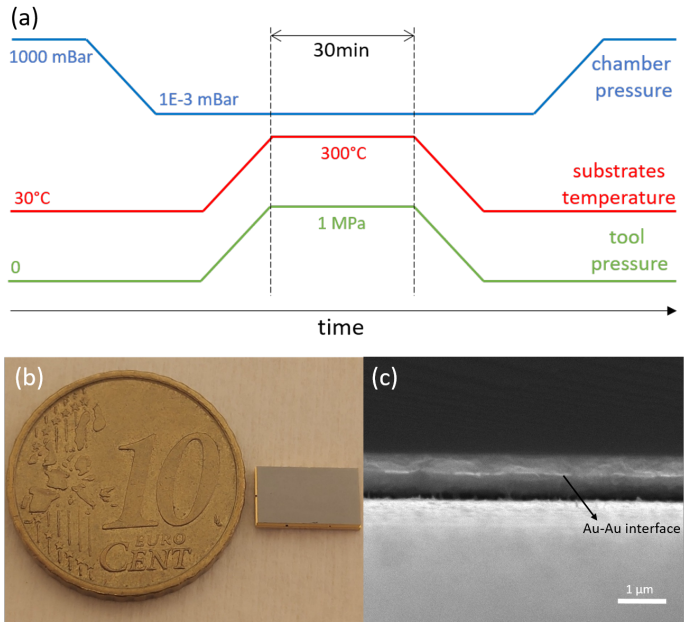

Figure 4.13: (a) Bonding recipe. (b) Fabricated chip with a EURO 10 cent coin, the chip consists of two integrating cylinders. (c) Scanning electron microscope (SEM) image of the gold-gold interface after bonding.

ing strength strongly depends on the quality of the surfaces, the two substrates are cleaned and activated with an Argon plasma treatment before bonding (pressure = 53 mTorr, power = 100 W, duration = 60 s). During bonding (SB6, from SUSS Microtech), the chamber is first pumped down to vacuum (1e-3 mBar) to clean the chamber, then the two substrates are brought into contact and they are heated to 300 °C. A high pressure of $\sim$ 1MPa is applied on the substrates to overcome the surface asperities. The chamber pressure, substrates temperature and the tool pressure profiles are shown in Figure 4.13 (a), the duration of the bonding is 30 min. A picture of the fabricated chip consisting of two integrating cylinders can be seen in Figure 4.13(b) and the SEM image of the bonding interface is shown in Figure 4.13(c).

4.5 Experimental settings

In this section, the characterization of the fabricated integrating cylinder will be discussed. First, the details of the experimental setup are presented, together with the characterization procedure. Then an Allan deviation measurement is performed to determine the system noise and the detection limit. Finally, the proof-

of-concept CO_2 sensing results with the integrated cylinder are presented, together with the response time measurement of the integrating cylinder.

4.5.1 Experimental setup

To experimentally evaluate the fabricated integrating cylinder, the experimental setup as shown in Figure 4.14 is built. The setup consists of two paths, one for the sensing arm and one for the reference arm. The light emitted from the optical source is butt-coupled into the input waveguide of the integrating cylinder via a multimode fiber (CIR500/550, Artphotonics). The distance from the fiber to the input waveguide is $\sim 50\mu m$. We use a multimode fiber with a large core size ($\sim 500\mu m$) to collect more power from the optical source. At the sensing arm, light from the output waveguide of the integrating cylinder is collimated and re-focused onto a photodiode by two identical lenses (C037TME-E, Thorlabs), with a band pass optical filter sandwiched in between. Since the lens-filter-lens system sits very close to the integrating cylinder, which will be filled with CO_2 gas for the sensing measurement, any gas diffusion into the gaps between the filter and the

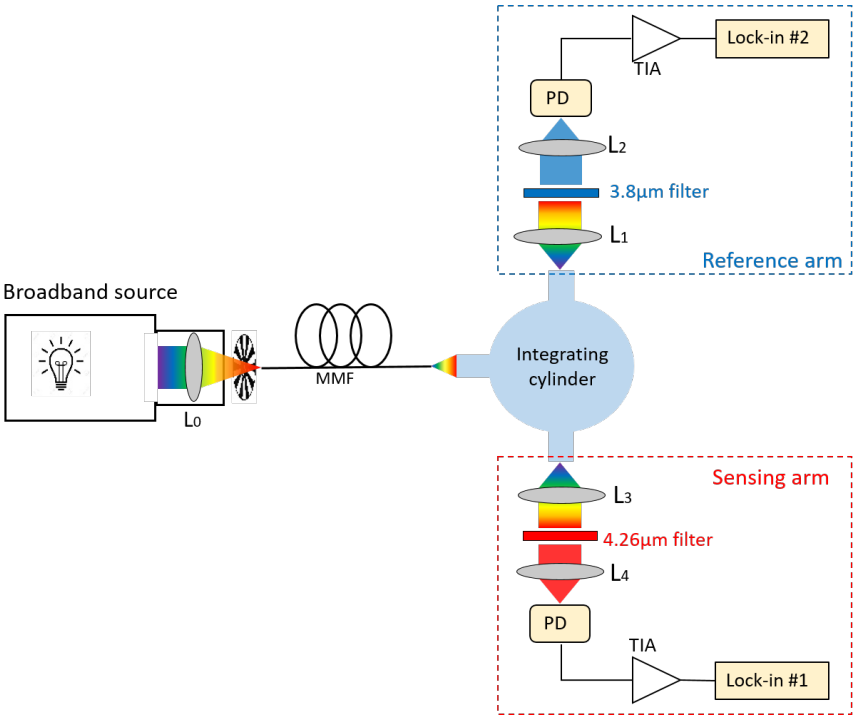

Figure 4.14: Schematic of the experimental setup. L: lens, MMF: multimode fiber, PD: photodiode, TIA: trans-impedance amplifier.

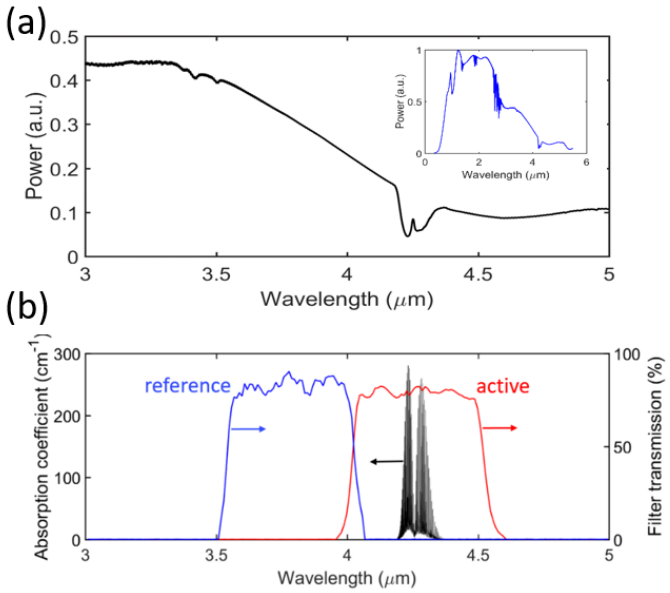

Figure 4.15: (a) Emission spectrum of the source in the $3-5\mu m$ wavelength range, the whole emission spectrum is shown in the inset. (b) Transmission spectra of the active and reference filters, superimposed on the CO_2 absorption spectrum in 3–5μm wavelength range [23].

lenses will lead to measurement errors. To prevent this error, the gaps between the filter and the lenses are sealed with rubber O-rings and isolated from the ambient. The signal from the photodiode is amplified by a trans-impedance amplifier (TIA) and then fed into a lock-in amplifier (SR830, Stanford Research System) for data acquisition and readout. The light is modulated by an optical chopper (MC1F10 blade with MC2000 controller, Thorlabs) placed between the source and the multimode fiber. We set the modulation frequency at 635Hz to avoid any interference or noise pickup from the overtones of the power grid. The duty cycle of the modulation is 50%. The reference arm only differs from the sensing arm in the optical filter, the two arms are otherwise identical. The two lock-in amplifiers are triggered by the optical chopper and are synchronized during the measurement.

4.5.2 Source and optical filters

We use a stabilized broadband optical source (SLS202, Thorlabs) in the setup. The source is a Tungsten halogen light bulb with internal electronic feedback loop to stabilize the output intensity. The working temperature of the source is 1900K, which gives a black body emission spectrum from 450nm to 5500nm, with the

peak wavelength at 1500nm. An additional collimation package (SLS202C, Thorlabs) is used to further collimate and clean the beam. The total output power of the collimated beam is $\sim 15mW$, with a stability $< 0.05\%$. A lens (LA5315-E, Thorlabs) is mounted at the end of the collimation package to focus the beam onto the multimode fiber. The emission spectrum of the source in the $3-5\mu m$ range is shown in Figure 4.15(a), with the whole spectrum shown in the inset. The dip around $4.26\mu m$ in the spectrum is due to the absorption of CO_2 in the atmosphere ($\sim$400ppm).

At the sensing arm, we use a band pass filter with pass band centered at $\lambda_0 = 4.25$ μm, hence the light absorption by CO_2 at $\sim 4.26\mu m$ can be interrogated. The pass band of the reference filter is centered at $\lambda_0 = 3.75\mu m$, with no overlap with the CO_2 absorption band. Therefore the signal at the reference arm will not change due to CO_2 absorption. The transmission spectra of the sensing and reference filters are shown in Figure 4.15(b), with the absorption spectrum of CO_2 superimposed in the figure.

4.5.3 Photodiodes and transimpedance amplifiers

At the detector side, two identical commercial InAsSb photodiodes (P13023-013CA, Hamamatsu) are used for the sensing and reference arms. We use the photovoltaic (unbiased) mode of the photodiode, which is the preferred operation mode for low frequency measurement and low light level detection. The photodiode is soldered on a custom PCB board which is mounted on the cage system together with the lenses and the optical filter. The photodiode works at room temperature (uncooled), and its major specifications are summarized in Table 4.2.

Peak sensitivity wavelength λ_p	Cut-off wavelength λ_c	Photo-sensitivity S	Detectivity D^* $\lambda = \lambda_p$	Noise equilalent power NEP $\lambda = \lambda_p$	Rise time
4.1 μm	5.3 μm	4.5 mA/W	1e9 $cm \cdot \sqrt{Hz}/W$	7e-11 $W/\sqrt{Hz}$	15 ns

Table 4.2: Specifications of the photodiodes used in the experimental setup.

We designed (with the help of Jasper Jans) a two-stage transimpedance amplifier (TIA) to convert the photo-current from the photodiode into a 'photo-voltage'. The circuit of the TIA is schematically shown in Figure 4.16 (a). The TIA is designed to amplify a photo-current of 10nA to a voltage of 100mV, with a transimpedance gain of $10^7\Omega$. We set the bandwidth of the TIA to be only 2kHz, considering the relatively low modulation frequency (635Hz) of the optical source. An electronic circuit simulator LTspice (Analog Devices) is used for the simulation of the TIA.

The simulated transient response and the frequency response are shown in Figure 4.16(b-c).

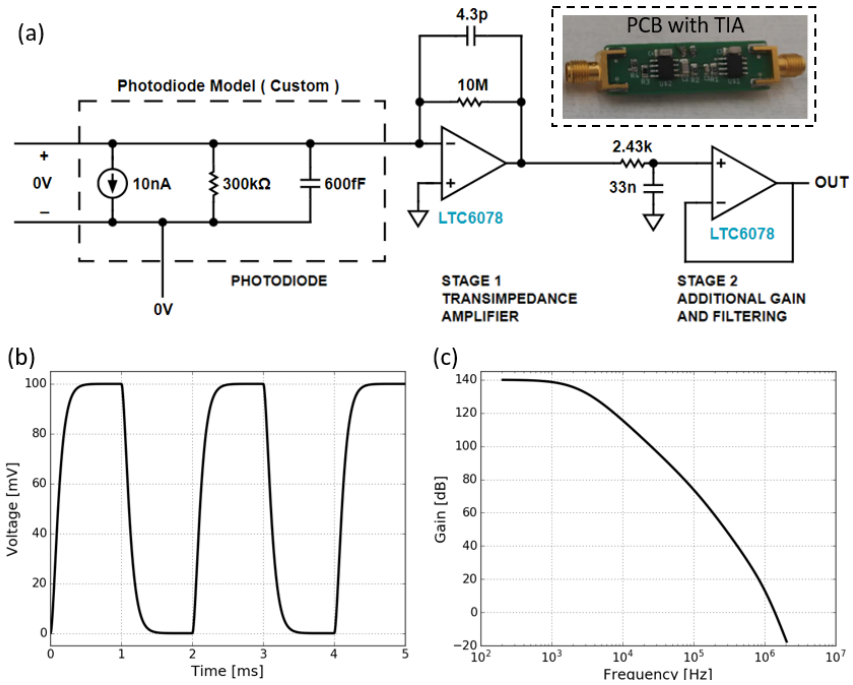

Figure 4.16: (a) Circuit schematic of the designed TIA, the soldered PCB with the TIA is shown in the inset. (b) The simulated transient response of the TIA. (c) The simulated AC response of the TIA.

4.5.4 Gas generation

CO_2 gas is supplied from certified gas cylinders (Praxair inc.), and nitrogen is used as a carrier and diluting gas to generate the sample gas with various concentrations of CO_2. The concentration of CO_2 in the diluted gas mixture can be calculated by:

$$C_{CO_2}(ppm) = \frac{F_{CO_2} \cdot 10^6}{F_{CO_2} + F_{N_2}} \times C_{cylinder} \tag{4.25}$$

where F_{CO_2} and F_{N_2} are the flow rates of CO_2 and nitrogen, respectively. The flow rates are controlled by two mass flow controllers (M13212646C, Bronkhorst). $C_{cylinder}$ is the CO_2 concentration in the gas cylinder. For the generation of the sample gas with CO_2 concentration larger than 1000ppm, a gas cylinder with 50% CO_2 is used. And a gas cylinder with 1000ppm CO_2 is used to generate the sample

gas with CO_2 concentration lower than 1000ppm. A gas tube made of Polyvinylidene Fluoride (PVDF) is used to deliver the gas mixture to the integrating cylinder. The diluted gas mixture is fed into the integrating cylinder by bringing the gas tube in close proximity to the integrating cylinder (not shown in the setup).

4.6 Proof-of-concept experimental results

As discussed in section 2.1.3, the signal (i.e. absorbance of CO_2) can be related to the transmission change by:

$$S = 1 - T = 1 - \frac{I_A}{I_{0A}} \tag{4.26}$$

in which the subscript 0 denotes the signal without the presence of CO_2 and A denotes the active (sensing) channel. The limit of detection (LOD) of the sensing system can be described by the minimum detectable transmission change $\frac{\Delta I_A}{I_{0A}}$. Although quite stable, the source power fluctuations and particularly the source drift can contribute to the transmission change, leading to an error in the measurement. To eliminate this error caused by source fluctuations and drift, the signal at the reference channel I_R is constantly measured and used as a substitute for I_{0A}. The imbalance between the two channels can be corrected by the factor $\frac{I_{R0}}{I_{A0}}$, which can be obtained by flushing the integrating cylinder with pure N_2 at the beginning of the measurement. The normalized absorbance signal can thus be written as:

$$S_{norm} = 1 - \frac{I_{R0}}{I_{A0}} \frac{I_A}{I_R} \tag{4.27}$$

With this formula, the common-mode noise and source fluctuations at both arms can be eliminated. We use the quantity S_{norm} as a figure of merit to evaluate the performance of the sensing system based on the integrating cylinder in all following measurement results.

4.6.1 Allan deviation measurement

The measurement resolution of any practical measurement system is ultimately limited by the noise in the system and the drift of the system, and this limitation can be characterized by means of the Allan deviation measurement [24]. The Allan deviation measurement offers a quantitative description of the variability of the measured quantity averaged over different time intervals, which enables the quantification and differentiation of the various noise processes present in the measurement system. The Allan deviation is a two-sample deviation by averaging the differences between two adjacent values of a time-series measured signal. The

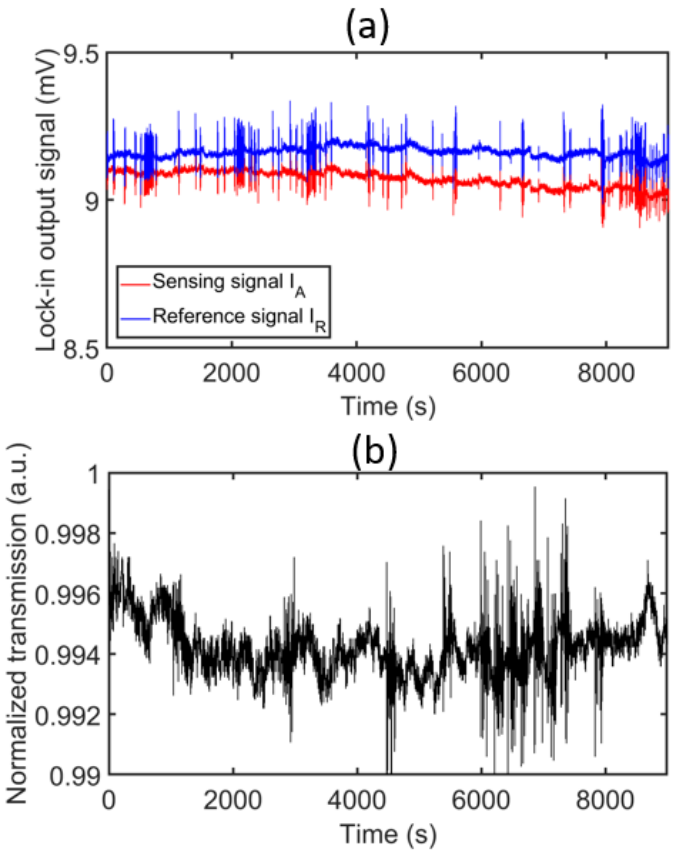

Figure 4.17: (a) Baseline of the sensing I_{A0} and reference signals I_{R0}, measured over a period of ∼3 hours, with 100ms lock-in integration time. (b) Normalized signal I_{A0}/I_{R0}.

Allan deviation is mathematically given by [25]:

$$\sigma_y(\tau) = \sqrt{\frac{1}{2\tau^2}\langle (x_{n+2} - 2x_{n+1} + x_n)^2 \rangle} \tag{4.28}$$

where τ is the averaging time period, and x is the measurement quantity. Using this equation, we can calculate the Allan deviation of the normalized signal and determine the optimal integration time of the lock-in amplifiers.

To determine the Allan deviation of the system, we measured the sensing signal and the reference signal over a period of ∼3 hours. During the measurement the integrating cylinder is constantly purged with pure nitrogen at a flow rate of 2L/min. Figure 4.17(a) shows the signals at the two arms as a function of time, the time interval (i.e. the integration time of the lock-in amplifier) between two consecutive data points is 100ms. One can see that both the sensing signal and

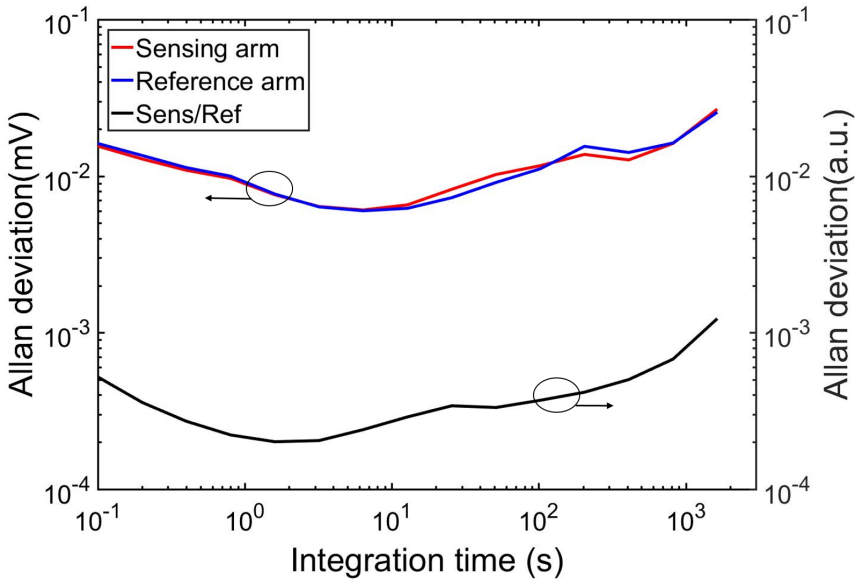

Figure 4.18: Allan deviation of the sensing and reference signals, as well as the normalized signal (in pure N_2 environment).

the reference signal are relatively stable, except that some (common) sharp peaks ($\sim 0.2mV$) are present occasionally. This is probably due to the vibrations of the setup (especially the fiber tip) caused by opening/closing the doors when people are entering/exiting the laboratory. The ratio of the sensing signal and the reference signal is plotted in Figure 4.17(b), which represents the normalized absorbance signal S_{norm} at zero CO_2. We see the sharp peak variations occurring at the same time with the sensing/reference signals, which means the common mode noise cannot be completely eliminated due to the imperfect matching between the two arms. Furthermore, large scale variations over long time period in the normalized signal is visible, which can be attributed to the source power fluctuations/drift (the temperature stability of the source is $\pm 15K$), or the temperature change in the laboratory.

Using these data, the Allan deviations of the sensing/reference signals as well as the normalized signal are calculated and plotted in Figure 4.18. One can see that as expected, the Allan deviation first decreases as the integration time increases. The minimum deviation of the normalized signal is about 2×10^{-4} AU, which is also the detection limit of the system (1σ). The Allan deviation increases at longer integration time intervals, which is due to the drift of the source and/or the changes in the detector performance. The optimal integration time (i.e. when Allan deviation of the normalized signal is at its minimum) is approximately 2

seconds. In all following measurements, we use an integration time of 1 second, which is restricted by the limited resolution of the time constant of the lock-in amplifier. From Figure 4.18, it is also possible to compare the detection limit when only the sensing arm is used and when both arms are used. The minimum deviation of the sensing signal is around $6 \times 10^{-3} mV$ (at 10s integration time), and its mean is about $10mV$ (from Figure 4.17), resulting a detection limit of $6 \times 10^{-3} mV / 10mV = 6 \times 10^{-4}$ AU. With the addition of the reference arm, the detection limit is reduced to $2 \times 10^{-4}/1 = 2 \times 10^{-4}$, which is $3\times$ smaller than that just using the sensing arm.

4.6.2 CO_2 sensing measurement

The response of the integrating cylinder to a change of CO_2 concentration is measured by feeding the integrating cylinder with a series of sample gases containing various concentrations of CO_2. At the beginning of the measurement, the integrating cylinder is purged with pure N_2 to determine the baseline of the normalized signal (I_{R0}/I_{A0}). During the measurement, the sensing signal I_A and the reference signal I_R are recorded for a period of 5 min at each concentration step. Figure 4.19(a) shows the two signals as the CO_2 concentration is varied. The letters from A to L correspond to different CO_2 concentrations which are listed on the right side of the figure. It can be seen that the reference signal stays relatively stable while the sensing signal decreases when the CO_2 concentration increases. Furthermore, we can see that the fringes on the two signals are strongly correlated, which is due to the common mode noise on both arms. These fringes can be eliminated by normalizing the sensing signal w.r.t the reference signal $\frac{I_A}{I_R}$, which is shown in Figure 4.19(b). The normalized absorbance S_{norm} for each CO_2 concentration can be calculated using Eq.4.27, with the correction factor I_{R0}/I_{A0} determined at zero CO_2 concentration. Figure 4.20 shows the calculated normalized absorbance at different CO_2 concentration levels. The absorbance is also simulated by propagating the spectrum of the source (shown in Figure 4.15(a)) through the active filter shown in Figure 4.15(b)) and then through different concentrations of CO_2 (with absorption spectrum shown in Figure 4.15(b)). A path length of 3.5 cm (as obtained from Table 4.1) is used in this simulation. It can be seen that the agreement between the measurement and the simulation is reasonably good. The response of the integrating cylinder at 100 ppm CO_2 is shown in the inset of Figure 4.20, where 10 measurements are superimposed over one figure. One can see there is a clear and repeatable step response. The normalized absorbance of 100 ppm CO_2 is about 9×10^{-4} AU, which is approximately three times of the signal deviation ($3 \cdot 2.5 \times 10^{-4} = 7.5 \times 10^{-4}$AU) as obtained from the Allan deviation plot.

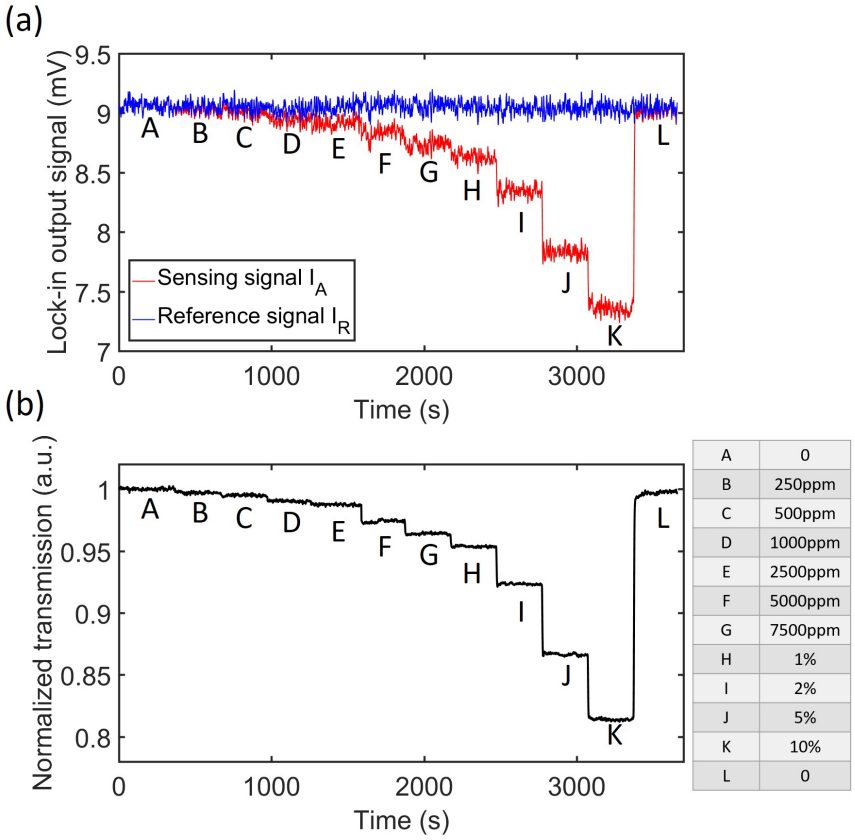

Figure 4.19: (a) Response of both sensing signal and reference signal to CO_2 concentration steps. (b) Normalized transmission, obtained by dividing the sensing signal with the reference signal. The CO_2 concentration steps are listed on the right side.

4.6.3 Response Time

The response time of a gas sensor is of great importance for applications such as leak detection in MAC systems, and real-time CO_2 concentration measurement can be possible with a fast response time. In industry, the response time is usually defined as the time needed for a sensor to reach 90% (T_{90}) of its total response when a step CO_2 concentration change is applied to the sensor. The response time of the integrating cylinder is measured using the same setup as shown in Figure 4.14. The integrating cylinder is first purged with a sample gas containing a high CO_2 concentration (50%), and the evolution of the sensing signal is recorded when the reading becomes stable. Then the gas flow is abruptly shut off and the CO_2 concentration in the integrating cylinder reaches ambient level (∼400 ppm) due

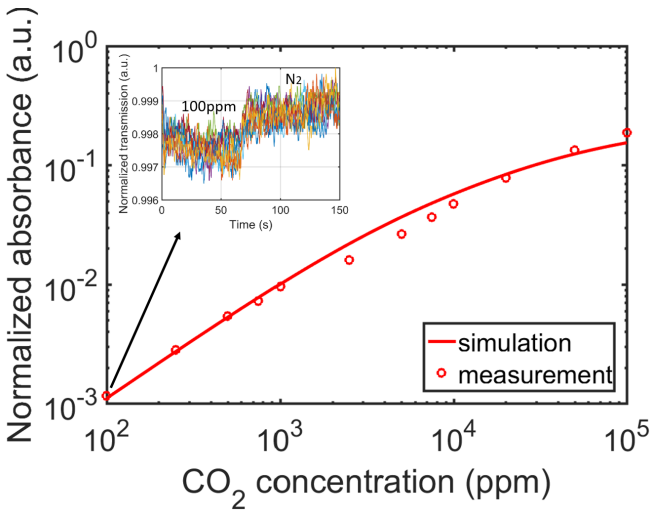

Figure 4.20: Normalized absorbance of the integrating cylinder at different CO_2 concentrations. The response at CO_2 = 100 ppm is in the inset, with 10 measurements superimposed in one figure.

to gas diffusion. Figure 4.21 shows the sensing signal as a function of time. In this measurement we use an integration time of 100ms to resolve the step of the signal. We can see that the integrating cylinder has a response time (T_{90}) of only 2.8 seconds, which is consistent with the simulation. The fast response time is primarily due to the small footprint of the integrating cylinder.

4.7 Conclusions

In this chapter, a detailed analysis and characterization of the integrating cylinder were presented. The integrating cylinder can be considered as a 2D version of the integrating sphere, implemented on a silicon chip. The multiple reflections of the incident light in the cylinder and the high-reflectivity mirror coated on the inner surfaces allow a long path length to be folded on a small chip area. The mathematical description of the integrating cylinder was given, showing that the sensitivity, defined as the transmission change due to CO_2 absorption, can be maximized for a certain cylinder radius R and access width d combination. 3D ray tracing simulation was performed to confirm the theoretical analysis. Simulations show that for an integrating cylinder with optimal design parameters (eg. radius $R = 2mm$ and access waveguide width $d = 200\mu m$), the equivalent path length and the total loss are 3.5cm and 7.4dB, respectively. The gas diffusion in the integrating cylinder was also modeled with finite difference element method, yielding a response

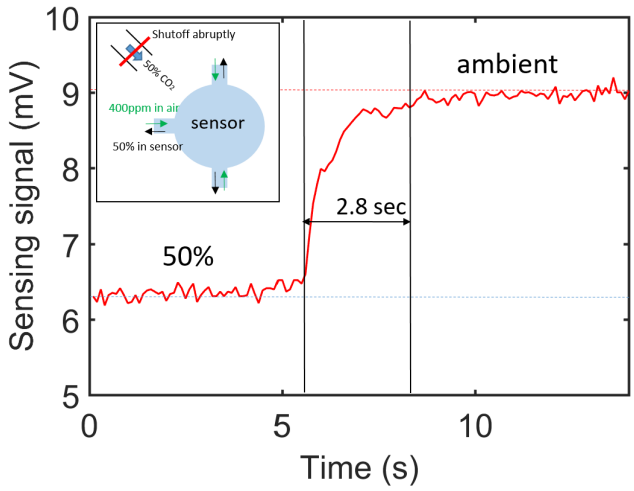

Figure 4.21: Response time measurement of the integrating cylinder, the integration time of the lock-in amplifier is 100ms. The gas flow mechanism when the 50% CO_2 is abruptly shut off is shown in the inset.

time of 2.6 seconds of the integrating cylinder. The fabrication process flow of the integrating cylinder was introduced, involving DRIE, gold deposition, and wafer bonding. These processes are all wafer-level techniques that are widely used in the semiconductor industry, making it possible for the mass production of the integrating cylinder with extremely low cost. The fabricated integrating cylinder was characterized using a dedicated gas sensing setup. An Allan deviation measurement was performed to determine the noise and stability of the sensing system. It was shown that by using the reference arm to eliminate the common mode noise, a minimum transmission change of $\sim 2 \times 10^{-4}$AU can be obtained using an lock-in integration time of 2 seconds. Further analysis revealed that this is $\sim 3\times$ better than just using the sensing arm. A CO_2 sensing measurement using the integrating cylinder was performed, showing a detection limit of $\sim$100ppm, which is consistent with the detection limit predicted by the Allan deviation plot. The detection limit is primarily limited by the drift of the source and the imperfect matching between the two arms. The response time of the integrating cylinder was measured by abruptly shutting off the high-concentration CO_2 gas flow. The response time of the integrating cylinder is approximately 3 seconds, which is attributed to the small footprint of the integrating cylinder.

References

[1] Xiaoning Jia, Joris Roels, Roel Baets, and Gunther Roelkens. *On-Chip Non-Dispersive Infrared CO2 Sensor Based On an Integrating Cylinder*. Sensors, 19(19):4260, 2019.

[2] J Beaulieu. *A guide to integrating sphere theory and applications*. Tech. rep., Labsphere, Inc., 1999.

[3] Mikael Lassen, David Balslev-Clausen, Anders Brusch, and Jan C Petersen. *A versatile integrating sphere based photoacoustic sensor for trace gas monitoring*. Optics Express, 22(10):11660–11669, 2014.

[4] E Hawe, P Chambers, C Fitzpatrick, and E Lewis. *CO2 monitoring and detection using an integrating sphere as a multipass absorption cell*. Measurement Science and Technology, 18(10):3187, 2007.

[5] E Hawe, C Fitzpatrick, P Chambers, G Dooly, and E Lewis. *Hazardous gas detection using an integrating sphere as a multipass gas absorption cell*. Sensors and Actuators A: Physical, 141(2):414–421, 2008.

[6] Jane Hodgkinson, Dackson Masiyano, and Ralph P Tatam. *Using integrating spheres as absorption cells: path-length distribution and application of Beer's law*. Applied optics, 48(30):5748–5758, 2009.

[7] Sé bastien Tranchart, Ikhlef Hadj Bachir, and Jean-Luc Destombes. *Sensitive trace gas detection with near-infrared laser diodes and an integrating sphere*. Applied optics, 35(36):7070–7074, 1996.

[8] Lena Simone Fohrmann, Gerrit Sommer, Giampaolo Pitruzzello, Thomas F Krauss, Alexander Yu Petrov, and Manfred Eich. *Integrating cell on chip—Novel waveguide platform employing ultra-long optical paths*. APL photonics, 2(9):096102, 2017.

[9] Eric Weisstein. *Circle line picking*. https://mathworld.wolfram.com/CircleLinePicking.html, 2020. Accessed 25 June 2020.

[10] Shaista Babar and JH Weaver. *Optical constants of Cu, Ag, and Au revisited*. Applied Optics, 54(3):477–481, 2015.

[11] Adolf Fick. *Ueber diffusion*. Annalen der Physik, 170(1):59–86, 1855.

[12] Eldor Paul. *Soil microbiology, ecology and biochemistry*. Academic press, 2014.

[13] Shinichi Tachi, Kazunori Tsujimoto, and Sadayuki Okudaira. *Low-temperature reactive ion etching and microwave plasma etching of silicon*. Applied physics letters, 52(8):616–618, 1988.

[14] Franz Laermer and Andrea Schilp. *Method of anisotropically etching silicon*, March 26 1996. US Patent 5,501,893.

[15] Jayalakshmi Parasuraman, Anand Summanwar, Frédéric Marty, Philippe Basset, Dan E Angelescu, and Tarik Bourouina. *Deep reactive ion etching of sub-micrometer trenches with ultra high aspect ratio*. Microelectronic engineering, 113:35–39, 2014.

[16] Jongseok Kim, Sangwook Kwon, Youngteak Hong, Insang Song, and Byeongkwon Ju. *A thermocompressive bonding method using a pure sputtered Au layer and its wafer scale package application*. Journal of Vacuum Science & Technology B: Microelectronics and Nanometer Structures Processing, Measurement, and Phenomena, 26(4):1363–1367, 2008.

[17] Abhijat Goyal, J Cheong, and S Tadigadapa. *Tin-based solder bonding for MEMS fabrication and packaging applications*. Journal of Micromechanics and Microengineering, 14(6):819, 2004.

[18] Qian Wang, Sung-Hoon Choa, Woonbae Kim, Junsik Hwang, Sukjin Ham, and Changyoul Moon. *Application of Au-Sn eutectic bonding in hermetic radio-frequency microelectromechanical system wafer level packaging*. Journal of electronic materials, 35(3):425–432, 2006.

[19] Shuji Tanaka. *Wafer-level hermetic MEMS packaging by anodic bonding and its reliability issues*. Microelectronics Reliability, 54(5):875–881, 2014.

[20] Reza Ghodssi and Pinyen Lin. *MEMS materials and processes handbook*, volume 1. Springer Science & Business Media, 2011.

[21] U Gösele and Q-Y Tong. *Semiconductor wafer bonding*. Annual review of materials science, 28(1):215–241, 1998.

[22] Yutaka Kunimune, Ken Okumura, Eiji Higurashi, Tadatomo Suga, and Kei Hagiwara. *Room-temperature wafer bonding using smooth gold thin films for wafer-level MEMS packaging*. In 2016 International Conference on Electronics Packaging (ICEP), pages 439–442. IEEE, 2016.

[23] Laurence S Rothman, Iouli E Gordon, Yury Babikov, Alain Barbe, D Chris Benner, Peter F Bernath, Manfred Birk, Luca Bizzocchi, Vincent Boudon, Linda R Brown, et al. *The HITRAN2012 molecular spectroscopic database*. Journal of Quantitative Spectroscopy and Radiative Transfer, 130:4–50, 2013.

[24] David W Allan. *Should the classical variance be used as a basic measure in standards metrology?* IEEE Transactions on instrumentation and measurement, (2):646–654, 1987.

[25] DV Land, AP Levick, and JW Hand. *The use of the Allan deviation for the measurement of the noise and drift performance of microwave radiometers*. Measurement Science and Technology, 18(7):1917, 2007.

5

Fully Integrated NDIR CO_2 Sensor

5.1 Introduction

In Chapter 4, the integrating cylinder has been investigated both numerically and experimentally. A fully integrated NDIR CO_2 sensor based on the integrating cylinder will be explored in this chapter. For the fully integrated sensor, we use a mid-IR LED and photodiode (PD) optopair as the optical source and detector. The LED-PD optopair provides the advantages of a large overlap between the emission spectrum of the LED and the absorption spectrum of CO_2. The responsivity of the LED and photodiode is higher than its thermal counterparts (e.g. a micro-light bulb and a thermopile detector), thus a lower limit of detection can be potentially achieved. In what follows, the path towards a fully integrated NDIR CO_2 sensor will be elaborated. First, 3D ray tracing simulations of the coupling efficiencies from the LED to the input waveguide of the integrating cylinder and from the output waveguide to the photodiodes are discussed. The fabrication process of the fully integrated sensor will be discussed in detail, including the integration process of the LED/PD on the bottom silicon substrate, as well as the integration process of the bottom substrate (containing the LED and PDs) and the top substrate (containing the integrating cylinder). Finally, the fabricated sensor will be evaluated experimentally. Experimental results on CO_2 sensing, response time, cross-sensitivity to water vapor, and long term stability will be presented.

5.2 LED and photodiode optopairs

An LED-photodiode optopair consists of an LED and a photodiode that are spectrally matched. Traditionally, NDIR sensors are based on thermal light sources and broadband detectors, together with narrow band optical filters with the pass band overlapping with the absorption band of the analyte of interest. The development of mid-IR LEDs and photodiodes has advanced optical sensing dramatically, due to their compactness and better power efficiency. The use of an optopair eliminates the need for mechanical modulators and optical filters, which allows to reduce the cost of the sensor system. LED/PD combinations have been widely used for sensing applications such as in CH_4 sensing at $3.4\mu m$ [1], CO sensing at $4.6\mu m$ [2], NO_2 sensing at $6.3\mu m$ [3, 4], and CO_2 sensing at $4.25\mu m$ [5–7]. These sensors consist of packaged LED/PD chips and co-assembled discrete gas cells, which provides a rugged construction and robust operation. However, it also compromises the cost and compactness of the sensor.

5.2.1 Mid-IR III-V LEDs

The advancement of the mid-IR LEDs is primarily driven by the growing need for low-cost optical sensors in the mid-IR spectral range, which contains strong absorption bands of many gas species as shown in Figure 2.1. Compared to thermal optical sources, mid-IR LEDs offer higher power spectral density, and they are superior to laser-based systems in terms of cost and complexity. As already discussed in Chapter 2, the emission wavelength of the III-V mid-IR LEDs can be matched to the absorption band of the analyte by engineering the composition of the III-V semiconductor layer stack. Mid-IR LEDs emitting at $4\mu m$ wavelength range typically use antimony-based material systems (e.g. InAsSbP, InGaAsSb and InAsSb). The material of the active layer can be ternary(e.g. InAsSb [8]), quaternary (eg. InAsSbP [9]), or quintenary (e.g. AlGaInAsSb [6]) semiconductor alloys. The use of multi-element alloys provides additional degrees of freedom to control the electro-physical properties, which offers a new approach to control the optical confinement and carrier leakage [6, 9].

However, the narrow band gap ($0.29eV$ for $4.3\mu m$) of these semiconductors imposes limitations on the efficiency of the LED. It has been demonstrated that the Auger recombination[1] increases when the band gap of the III-V semiconductor is decreased [10, 11], which limits the internal efficiency of the mid-IR LEDs. Moreover, current crowding effects are more pronounced for LEDs working at longer wavelengths. To minimize the overlap between the top metal contact and the top

[1] Auger recombination is a non-radiative process involving three carriers. When an electron and a hole recombine, instead of emitting a photon, the energy is transferred to a third particle: either an electron is raised higher into the conduction band or a hole is pushed deeper into the valence band, its energy is ultimately lost to thermal vibrations.

surface (hence maximizing the extraction efficiency), a top-emitting mid-IR LED is usually fabricated as a planar mesa with lateral current injection geometry. The lateral current injection creates current crowding near the metal contact edge, thus the effective emitting area is decreased. This effect is more pronounced in LEDs emitting at longer wavelengths due to the low junction resistance of narrow band gap materials [12, 13]. Moreover, the local heating and the temperature gradient generated by the current crowding effect increases the Auger recombination and thus the internal efficiency of the LED is decreased [14, 15]. For the reasons mentioned above, the internal efficiency of a mid-IR LED is only a few percent and continuous wave (CW) operation is often forbidden. In addition to the low internal efficiencies, mid-IR LEDs also suffer from low extraction efficiencies. The high refractive indices of the narrow band gap III-V materials ($n > 3.5$) leads to a small critical angle and therefore the numerical aperture for light to escape is limited. The extraction efficiency from one side of the chip can be approximated by $\eta_{ext} = 1/n(n+1)^2$ [16], which is only about 1.4% for a III-V material with $n = 3.5$. As both the internal efficiency and the extraction efficiency are relatively low, the output power from a typical mid-IR LED is only on the order of $10\mu W$.

5.2.1.1 LED used in this thesis work

In this thesis work, we use the LED bare chips provided by IBSG [17]. A picture of the LED bare chips and the layer structure are shown in Figure 5.1. The LED chips have a top ring contact and a planar bottom contact, with which the chips can be integrated on the silicon substrate with flip-chip bonding. The main specifications of the LED are summarized in Table 5.1, in which QCW stands for Quasi-CW mode of the LED (repetition rate = 0.5 kHz, pulse duration = 1 ms, duty cycle = 50%).

L,W,H [μm]	Emitting area [μm]	λ_{peak} [μm]	FWHM [μm]	P_{QCW} [μW]
400,400,250	300x300	4.15	0.8	10

Table 5.1: Major specifications of the LED used in this work.

5.2.2 Mid-IR photodiode

5.2.2.1 Performance metrics

Responsivity and quantum efficiency

The responsivity of the photodiode is a quantity to measure the effectiveness of the conversion of light power into electrical current, and it is defined as the ratio of the photocurrent I_P to the optical power P of the incident light at a given wavelength:

$$R_\lambda = \frac{I_P}{P}[A/W] \tag{5.1}$$

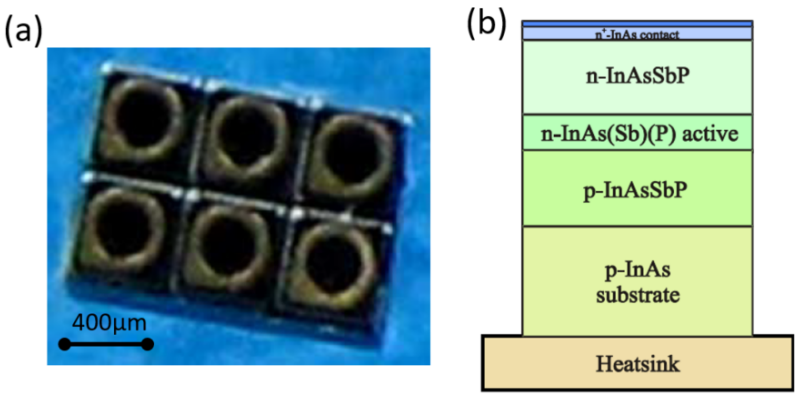

Figure 5.1: (a) Picture of the LED bare chips, the LED has a top ring contact and a planar bottom contact. (b) Layer stack of the LED. Pictures from [17].

The responsivity varies with the wavelength of the incident light as well as the applied bias voltage and temperature. Responsivity increases slightly with the applied reverse bias voltage due to improved charge collection efficiency in the photodiode, while the temperature dependence of the responsivity is due to the change in band-gap with temperature variations. The quantum efficiency η of the photodiode is defined as the fraction of the incident photons that contribute to electrons in the photocurrent, it is related to responsivity by:

$$\eta = 1.24 \frac{R_\lambda}{\lambda} \tag{5.2}$$

with R_λ being the responsivity in A/W and λ being the wavelength in μm.

Noise equivalent power

The noise equivalent power (NEP) is defined as the input optical power that results in a signal-to-noise ratio (SNR) of 1 in a 1 Hz bandwidth. It is a measure of the minimal detectable power of the photodiode, i.e., the weakest optical signal that can be detected. The NEP is defined as:

$$NEP = \frac{I_{tn}}{R_\lambda} [W/\sqrt{Hz}] \tag{5.3}$$

where I_{tn} is the total noise current of the photodiode. The minimum detectable optical power change in a certain bandwidth (BW) can therefore be calculated by:

$$P_{min} = NEP \cdot \sqrt{BW} \tag{5.4}$$

Specific detectivity

To compare the sensitivities of photodiodes with different areas, the specific detectivity D^* is often used. D^* is defined as the photo sensitivity per unit area of the photodiode, and it can be derived from the NEP by:

$$D^* = \frac{\sqrt{A}}{NEP}[\frac{cm\sqrt{Hz}}{W}] \tag{5.5}$$

where A is the active area of the photodiode.

5.2.2.2 Photodiode equivalent circuit

From an electronics point of view, the photodiode can be modeled by the equivalent circuit as shown in Figure 5.2. The photocurrent I_{ph} is the current generated by the incident light. Apart from this photocurrent, a dark current I_d is also generated by the thermal excitation of carriers in the absence of light. The magnitude of the dark current depends not only on the dimensions of the active area (a larger active area gives a larger dark current), but also on the working temperature of the photodiode: a higher temperature leads to a larger dark current. The dark current is virtually zero when the photodiode is not biased. Moreover, the dark current in infrared photodiodes are typically larger than their visible and near-infrared counterparts, as the the carrier excitation requires less energy for smaller band gaps. For instance, the dark current of the mid-IR phododiode used in this thesis work is $400\mu A$ (bias voltage = -0.5V, T = 20°) [18], while the typical dark current for a photodiode with peak responsivity at $1.5\mu m$ is only $0.1nA$ (bias voltage = -5V, T = 25°) [19]. This large dark current of mid-IR photodiodes imposes a disturbing shot noise current and also increases the noise floor.

Shunt resistance R_{sh} is another important parameter of the photodiode, and it is defined as the resistance of the p-n junction when the photodiode is zero-biased. The shunt resistance can be determined by calculating the first derivative of the bias voltage w.r.t the current for a small bias voltage:

$$R_{sh} = \frac{\delta V}{\delta I}|_{V\sim 0} \tag{5.6}$$

The actual values of shunt resistance range from several Ω to a few $G\Omega$, depending on the operating wavelength range. Due to the small band gap of the semiconductor materials in the mid-IR photodiodes, the shunt resistance is typically on the order of tens of Ω, which is many orders of magnitude smaller than the photodiodes working at visible or near-infrared wavelength range [20]. This relatively small shunt resistance produces a large Johnson noise (as per Eq. 5.9), thus limiting its sensitivity, and it also imposes challenges on the design of the amplifiers [20].

Apart from the resistive characteristics of the p-n junction, it also has a parasitic junction capacitance C_j: a capacitor is formed by the p- and n-region of the photodiode, separated by the depletion region. The presence of the junction capacitance

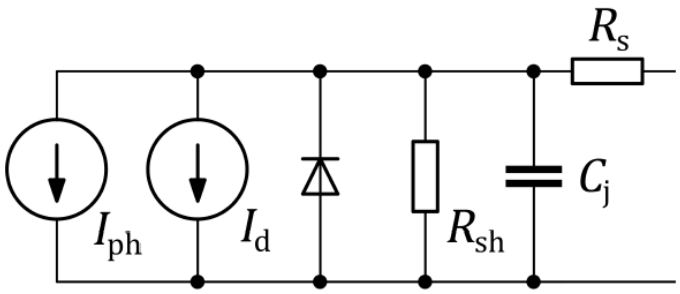

Figure 5.2: Equivalent circuit of a photodiode [21], I_{ph} is the photocurrent, I_d is the dark current, C_j is the junction capacitance, R_{sh} is the shunt resistance and R_s is the series resistance.

limits the response speed of the photodiode by the resistance-capacitance (RC) time constant, and the bandwidth of the photodiode is given by:

$$f_{BW} = \frac{1}{2\pi R_{tot} C_j} \tag{5.7}$$

where R_{tot} is the summation of the series resistance and the load resistance. The series resistance R_s comes from the contact resistance between the metal electrodes and the photodiode contact layers. It can also come from electrical connections such as wire bonds.

5.2.2.3 Noise characteristics

In a photodiode, the limit of light detection is determined by its noise characteristics. The noise of a photodiode takes three forms: $1/f$ noise, shot noise and Johnson noise.

$1/f$ noise

The mechanisms that produce $1/f$ noise are poorly understood. The noise power of $1/f$ noise is inversely proportional to the modulation frequency f, and its magnitude is typically much smaller than shot noise except at very low modulation frequencies (lower than a few hundred Hz). To reduce the $1/f$ noise, the photodiode should work at a reasonably high frequency, usually as high as a few KHz, which should reduce the contribution of $1/f$ noise to a small amount.

Shot noise

Shot noise is associated with the particle nature of light and of electrical current, and it is related to the fluctuations in both the photocurrent and the dark current, resulting from the statistical uncertainty in photon arrival rate and electron generation rate. The magnitude of the shot noise is expressed as the root mean square

(rms) noise current:

$$I_{sn} = \sqrt{2q(I_P + I_D)BW} \tag{5.8}$$

where q is the electron charge, I_P and I_D are the photo current and dark current, respectively, and BW is the noise measurement bandwidth.

Johnson noise

Johnson noise, also known as thermal noise, originates from the thermal generation of charge carriers. All resistive materials have Johnson noise associated with them, and the magnitude of the Johnson noise current is given by:

$$I_{jn} = \sqrt{\frac{4k_BTBW}{R_{sh}}} \tag{5.9}$$

in which k_B is the Boltzmann constant, T is the absolute temperature, and R_{sh} is the shunt resistance of the photodiode. The total noise current (in Eq. 5.3) generated in a photodiode is then given by:

$$I_{tn} = \sqrt{I_{sn}^2 + I_{jn}^2} \tag{5.10}$$

5.2.2.4 Photodiode operation mode

As shown in Figure 5.3, a photodiode usually operates either in the photoconductive mode, or in the photovoltaic mode. In photoconductive mode, the photodiode is reverse-biased, which increases the width of the depletion region and therefore the junction capacitance is decreased. The application of a reverse bias can greatly improve the response speed (bandwidth) and linearity of the photodiode, thus the photoconductive mode is often used for high speed applications. Shot noise is the dominating noise source when the photodiode operates in photoconductive mode, especially for mid-IR photodiodes. When a reverse bias voltage is applied, the relatively large dark current generates a high shot noise as per Eq.5.8, making low-level light detection unsuitable. In photovoltaic mode, a zero bias voltage is applied across the photodiode, which minimizes the dark and the noise currents. Therefore it's preferred for ultra low-level light detection and low frequency operation. Johnson noise is the dominant noise in photovoltaic operation mode. For mid-IR photodiodes, the Johnson noise is more pronounced as the shunt resistance is typically only a few tens of Ohms, due to the small band gaps of the semiconductor materials. To determine the optimal operation mode (photoconductive *vs.* photovotaic) of the photodiode, the magnitude of the shot noise, Johnson noise, and the total noise current of the photodiode at both operation modes are calculated. In this calculation, we use the following parameters of the photodiode (also listed in the next section): shunt resistance of 30Ω, dark current of $2050\mu A$, and a responsivity of $2.5A/W$. We assume an optical power of $10nW$ for the incident light and set the bandwidth of the system to be 1Hz, and we assume the dark current at the photovoltaic mode is zero. The calculated noise contributions and the

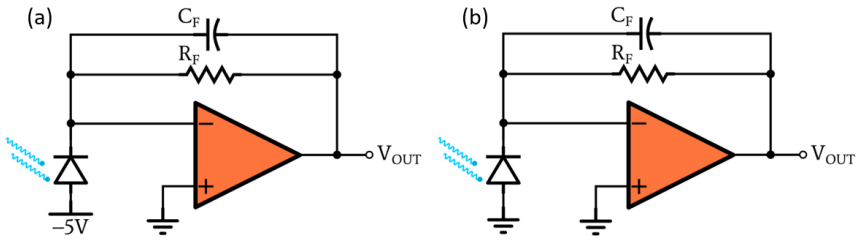

Figure 5.3: (a) Photodiode working at photoconductive mode. (b) Photodiode working at photovoltaic mode. Figures taken from [22].

total noise current when the photodiode works in the photoconductive and photovoltaic modes are listed in Table 5.2. It can be seen that the total noise current in the photoconductive mode is about 50% higher than that of the photovoltaic mode, therefore we choose the photovoltaic mode as the operation mode of the photodiode.

	photoconductive mode	photovoltaic mode
shot noise [A]	2.56e-11	8.95e-14
Johnson noise [A]	2.34e-11	2.34e-11
total noise [A]	3.5e-11	2.34e-11

Table 5.2: Noise contributions and the total noise current when the photodiode works at photoconductive and photovoltaic modes.

5.2.2.5 Photodiodes used in this thesis work

In this thesis work, two different photodiodes are used. For the sensing channel of the CO_2 sensor, mid-IR photodiode bare chips (PD42) provided by the Mid-IR Diode Optopair Group [23] are used. These photodiodes have a spectral response centered at $4.15\mu m$. For the reference channel of the sensor, the spectral response of the photodiodes should not overlap with the absorption band of CO_2 at $4.2\mu m$. In this regard we choose the photodiode bare chips (PD36) provided by IBSG [18]. The photodiodes have a spectral response with a cut-off wavelength at $\sim 4\mu m$. The dimensions (L, W, H) of the photodiodes at the sensing channel and the reference channel are both $500\mu m, 500\mu m, 200\mu m$. Figure 5.4 shows the microscope images of the sensing and the reference photodiodes, the sensing photodiode PD42 has a grid top contact and the reference photodiode PD36 has a point top contact. Both the photodiodes have a planar bottom contact. The major specifications of the two photodiodes are summarized in Table 5.3.

The normalized spectral responses of the sensing photodiode and the reference

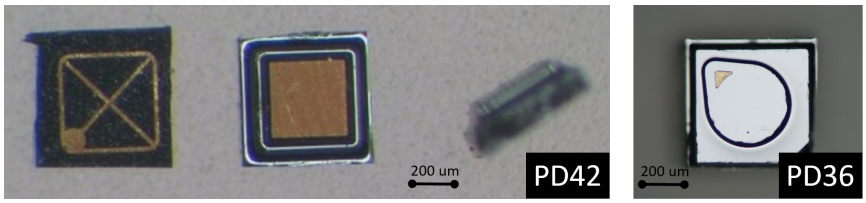

Figure 5.4: Microscope images of the sensing photodiode PD42 and the reference photodiode PD36.

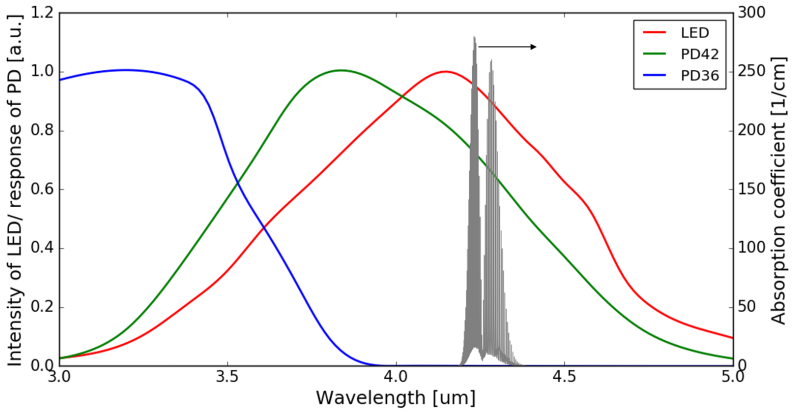

Figure 5.5: Normalized emission spectrum of the LED [17] and spectral responses of the photodiodes [18, 23], with the absorption spectrum of CO_2 in the $3\mu m - 5\mu m$ wavelength range [24].

photodiode are shown in Figure 5.5, with the emission spectrum of the LED and the absorption spectrum of CO_2 at $4.2\mu m$ interposed on top. It can be seen that the spectral response of the sensing photodiode (PD42) overlaps with the emission spectrum of the LED and the CO_2 absorption band, while there is no overlap between the spectral response of the reference photodiode (PD36) and the CO_2 absorption band.

PD	$\lambda_{peak}[\mu m]$	$R_{\lambda,max}[A/W]$	$D^*[cm \cdot Hz^{1/2} \cdot W^{-1}]$	NEP$[W \cdot Hz^{-1/2}]$	$R_{sh}[\Omega]$	C_j [pF]	$I_D[\mu A]$(V = -0.5V)
PD42BS	4.15	2.5	5e9	1.0e-11	30	170	2050
PD36-03	3.3	1.1	4e9	1.3e-11	300	400	400

Table 5.3: Specifications of the photodiodes used in this thesis. PD42BS: photodiode at the sensing channel. PD36-03: photodiode at the reference channel.

5.3 Estimation of coupling efficiencies

To estimate the coupling efficiency from the LED to the input waveguide of the integrating cylinder, and the coupling efficiency from the output waveguide to the photodiodes, similar 3D ray tracing simulations (in OpticStudio) as in section 3.2 are performed. The simulation setup is as the following:

- Simulation is performed using the non-sequential mode of OpticStudio, as it allows for multiple reflections of the light rays at a certain interface.
- The LED/PD sits in a metallized trench as shown in Figure 5.6, the trench can be achieved by the selective etching of silicon with KOH. We use access waveguides to couple light from the LED and to the photodiode, as it allows for the decoupling of the LED/photodiode dimensions and the fraction of power extracted from the cavity, therefore the sensitivity of the sensor can be optimized (as discussed in section 4.4).
- As the thickness of the substrate is much larger than that of the active layer, the active regions and the substrates of the LED/PDs are given a refractive index of 3.5, that of n-InAs ($n = 2 - 3e16cm^{-3}$). For the same reason, an absorption coefficient of 10/cm is applied to both the substrates and the active regions [25].
- A coating with the refractive index of gold (200nm) is applied on the trench as well as on the inner walls of the input/output waveguides.
- For the simulation of the LED coupling efficiency, a rectangular volume source emitting at $4.26\mu m$ is placed at the center of the LED, with isotropic emission in all directions. A rectangular power detector is placed at the cross section of the input waveguide to record the power coupled to the waveguide.
- For the simulation of the photodiode coupling efficiency, a point source with isotropic emission is placed at the center of the output waveguide (1mm away from the PD), a rectangular power detector is placed at the cross-section of the PD to record the power coupled to the PD.

In the simulation, a total number of 100,000 rays are emitted from the LED/ point source with the optical power equally distributed in each ray. The coupling efficiency from the LED to the input waveguide is simulated to be about 8%(in one direction), and the coupling efficiency from the output waveguide to the PD is about 30%.

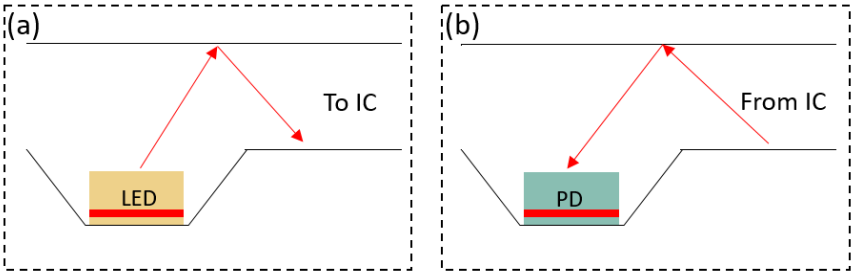

Figure 5.6: Simulation setup for the coupling efficiencies. (a) From LED to the input waveguide. (b) From output waveguide to the photodiode.

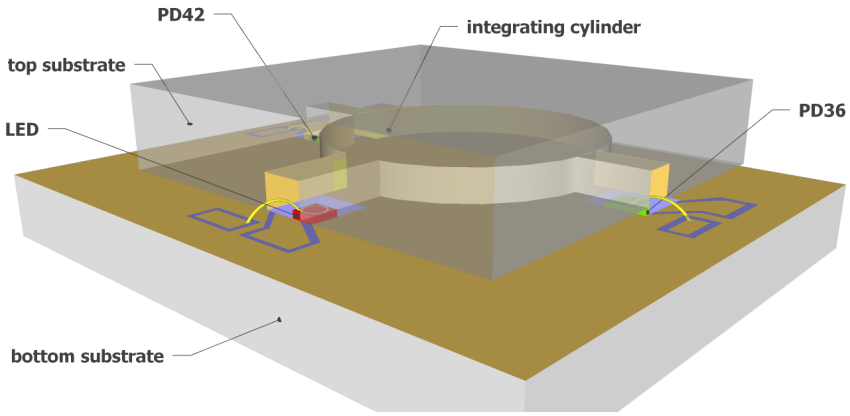

Figure 5.7: 3D schematic of the fully integrated NDIR CO_2 sensor. The sensor consists of two silicon substrates. On the top substrate, the integrating cylinder is defined. On the bottom substrate, the LED and photodiodes are integrated on-chip. PD42: photodiode at the sensing arm, with spectral response aligned with the CO_2 absorption band. PD36: photodiode at the reference arm, with spectral response cutoff at $4\mu m$.

5.4 Full sensor fabrication

The schematic of the fully integrated NDIR CO_2 sensor is shown in Figure 5.7. The sensor is formed by wafer bonding of two silicon substrates. The top substrate contains the integrating cylinder, of which the fabrication process has been discussed thoroughly in Chapter 4. On the bottom substrate, the LED and photodiodes are integrated on-chip. The fabrication process of the bottom substrate starts with a blank silicon substrate. The main steps of the fabrication flow are summarized below as well as in Figure 5.8.

- A first optical lithography and silicon etching step is performed, with the

purpose to define the outer boundary of the bottom substrate, and to define the alignment markers for the following processes.

- A thin layer of SiO_2/SiN_x (300 nm/400 nm) is deposited on both sides of the substrate. The SiN_x layer acts as the hard mask for silicon etching. Three rectangles are then opened for selective silicon etching with a second lithography and dry etching step.

- Three trenches are formed on the substrate by selective etching of silicon with KOH, as shown in Figure 5.8 (b). The etching depth is $\sim 250\mu m$, and the widths of the trenches at the bottom surface are designed to be $\sim 50\mu m$ wider than the widths of the LED/PD.

- A thin layer of SiO_2 ($\sim 500nm$) is deposited on the substrate to isolate the two contact pads of the LED/PD (see later), as the silicon substrate (p-doped) we use is weakly conductive.

- Gold deposition and liftoff. In this step, the gold reflectors on the bottom substrate are formed (with Ti as adhesive layer), as well as the two contact pads (anode and cathode) for the LED/PD. As shown in Figure 5.8 (c), both contact pads need to be isolated from the large-area gold reflector on the substrate. Therefore, the inclined sidewalls of the trenches need to be protected from gold deposition. In this context, we used a resist photopolymer film (FX900 series, from DuPont) as the protective layer. The large thickness of the resist film ($\sim 20\mu m$ thick) allows it to hang over the trenches. Figure 5.9 (a) shows the patterned resist film after lithography, and the contact pads after gold deposition and lift-off are shown in Figure 5.9 (b).

- LED/PD bonding. In this step, the LED/PD bare chips are bonded (with top sides facing up) in the trenches by flip-chip bonding. Due to the high roughness of the gold layer on the bottom of the trench and the bottom contacts of the LED/PD (formed by eletroplating of gold), we use a conductive silver adhesive (478SS, from Electron Microscopy Sciences) as bonding agent. After bonding, the adhesive is then cured at 160° for 30 minutes.

- Wire bonding of the LED/PD. In this step, the top contact pads of the LED/PD are wire-bonded to the anode pads on the silicon substrate, Figure 5.9 (c) shows a microscope image of the LED bare chip with wire bond.

- Finally, the sensor is formed by wafer bonding of the top substrate and the bottom substrate. The bonding is performed by gold-to-gold thermocompression bonding (at 160°, 1MPa, for 30 minutes).

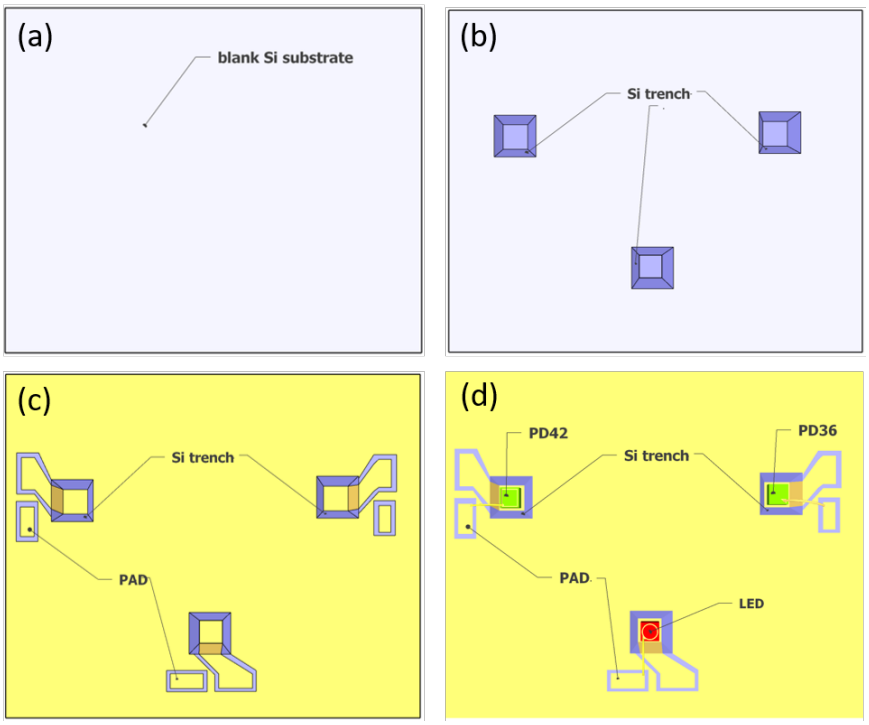

Figure 5.8: Fabrication process flow of the bottom substrate containing the LED/PD chips. (a) Blank silicon substrate. (b) Three trenches are formed on the substrate via selective etching of silicon by KOH. (c) Gold deposition and lift-off. In this step, two contact pads (anode and cathode) are formed for the LED/PD, the deposited gold on the bottom substrate acts as a reflector for the integrating cylinder. (d) LED/PD bonding and wire bonding. The LED/PD chips are bonded in the trench using flip-chip bonding, after which the top contacts of the LED/PD are wire-bonded to the anode pads.

5.5 Trans-impedance amplifier design

When designing the trans-impedance amplifiers (TIA) for the mid-IR photodiodes, one has to take into account the low shunt resistance as it can introduce significant noise currents. Due to the relatively large overall loss of the system, the optical power reaching the photodiodes is very low (on the order of $10nW$). For reasons as described earlier, the photodiode should work in photovoltaic mode (un-biased) to detect such a weak signal. In photovoltaic mode, the Johnson noise is dominant, the spectral noise density i_n of the photodiode is given by:

$$\sqrt{i_{n,PD}^2} = \sqrt{\frac{4kT}{R_{sh}}}[A/\sqrt{Hz}] \tag{5.11}$$

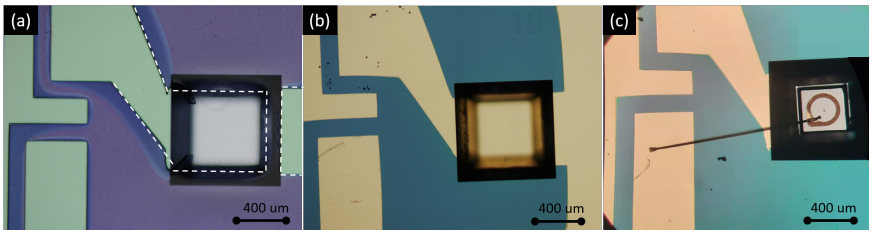

Figure 5.9: (a) Patterned photoresist film (in purple) at the input side, the resist film is hanging over the edge of the trench. (b) Contact pads after gold deposition and lift-off. (c) Flip-chip bonded LED in the trench, with a wire bond connecting the top contact of the LED and the contact pad on the substrate.

The TIA for the photodiode consists of a current-voltage converter, in which the anode and cathode of the photodiode are connected to the inverting and non-inverting inputs of the op-amp, respectively. The photo current I_P from the photodiode is then amplified by a feedback resistor R_f, which also has a Johnson noise given by:

$$\sqrt{i_{n,R_f}^2} = \sqrt{\frac{4kT}{R_f}}[A/\sqrt{Hz}] \tag{5.12}$$

In the TIA circuit, the op-amps themselves exhibit both a voltage noise $\sqrt{e_{n,OP}^2}$ and a current noise $\sqrt{i_{n,OP}^2}$ at the input side. The available low-noise op-amps can be divided into two categories [20]:

- op-amps with entrance circuit based on bipolar transistors, the voltage noise for these op-amps is typically very low (< 1 nV/$\sqrt{Hz}$), but the current noise is significant (up to a few pA/$\sqrt{Hz}$);
- op-amps with entrance circuit based on field-effect transistors, the current noise for these op-amps is low (a few fA/$\sqrt{Hz}$), but the voltage noise is high (up to a few nV/$\sqrt{Hz}$);

To determine which type of op-amps can be used in the TIA circuit, the total noise current at the input of the op-amp can be calculated by:

$$\begin{aligned} i_{n,\Sigma} &= \sqrt{i_{n,PD}^2 + i_{OP}^2 + i_{n,R_f}^2} \\ &= \sqrt{\frac{4kT}{R_{sh}} + i_{n,OP}^2 + (\frac{e_{n,OP}}{R_{sh}})^2 + \frac{4kT}{R_f}} \end{aligned} \tag{5.13}$$

in which the first and the last terms under the square root are the noise currents generated by the shunt resistor and the feedback resistor, respectively. As the feedback resistor R_f is usually much larger (up to MΩ) than the shunt resistance R_{sh} of the mid-IR photodiodes (typically on the order of tens of Ω), the last term in

Eq.5.15 can be ignored. The second and the third terms are the noise contributions from the op-amp. It can be seen that the voltage noise of the op-amp is scaled by a factor of $1/R_{sh}$. For small R_{sh}, the noise contribution from the voltage noise of the op-amps is dominant. It has been demonstrated by numerical calculations that for photodiodes with $R_{sh} < 3k\Omega$, op-amps with low voltage noise is the preferred choice to minimize the total noise current [20]. Therefore, in the TIA design for both the sensing photodiode and the reference photodiode we use the op-amp LT1028 (from Analog Devices), which has a low input noise density of only $e_{n,OP} = 0.85nV/\sqrt{Hz}$.

The circuit of the TIA for the sensing photodiode (PD42) is schematically shown in Figure 5.10(a). The LED works at the Quasi-CW (QCW) mode, with a driving current of 200mA (pulse width = 1ms, duty cycle = 50%). The TIA is designed to amplify a photocurrent of $20nA$ to a voltage of $20mV$, with a transimpedance gain of $10^6\Omega$, the bandwidth of the TIA is 2kHz. For the TIA of the reference photodiode (PD36), we set the gain to be $5 \cdot 10^6\Omega$, considering the smaller overlap between the spectral response of the reference photodiode and the emission spectrum of the LED (see Figure 5.5). The two TIAs are otherwise identical. An electronic circuit simulator LTspice (Analog Devices) is used for the simulation of both TIAs. The simulated transient response and the frequency response are shown in Figure 5.10(b-c). The two TIA circuit are then soldered on a printed circuit board (PCB), after which the fabricated sensor chip is mounted on the PCB and the contact pads of the LED/PDs are wire-bonded to the contact pads on the PCB. The PCB consisting of two TIAs is shown in Figure5.11, with the sensor mounted and wire-bonded on it.

5.6 Experimental results

As in Chapter 4, we use the normalized absorbance S_{norm} as the figure of merit to evaluate the performance of the full sensor. In the full sensor, we use an integrating cylinder with a radius of $2.6mm$, and the input/output waveguide widths are $400\mu m$. Such an integrating cylinder yields an equivalent path length of $\sim 3.4cm$ and a total loss of $\sim$ 7.2dB as shown in section 4.3. The LED is driven by a pulsed current source (LDP-3811, ILX Lightwave), and the output signals from the TIAs are fed into two lock-in amplifiers (SR380, Stanford Research Systems). The two lock-in amplifiers are triggered by the current source, and they are synchronized with identical settings during the measurement.

5.6.1 Allan deviation

As in Chapter 4, to determine the optimal integration time of the lock-in amplifiers and the limit of detection of the sensor system, an Allan deviation (with definition

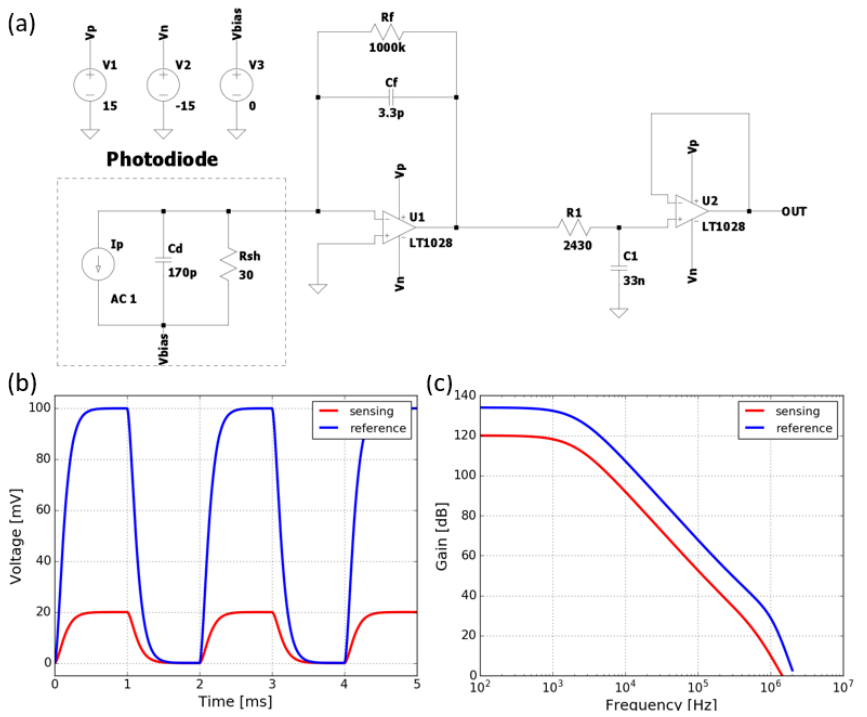

Figure 5.10: (a) Circuit schematic of the TIA for the sensing photodiode (PD42). The TIA for the reference photodiode (PD36) only differs in the feedback resistor and capacitor. (b) Transient response of both TIAs. (c) AC response of both TIAs.

given in Chapter 4) measurement is performed. The sensing signal and the reference signal are measured over a period of ∼3 hours (with a time interval of 100 ms). During the measurement, the integrating cylinder is constantly flushed with pure N_2. Figure 5.12 shows the signals at the two arms as a function of time. It can be seen that the amplitudes of the sensing and the reference signals are about $25mV$ and $15mV$, respectively. To compare the signal strengths with the theoretical predictions, we can calculate the strength of the sensing signal (as the strength of the reference signal is more difficult to calculate due to the uncertainties in the spectral overlap) using the specifications of the LED (optical power P_{LED} from Table 5.1) and the sensing photodiode (peak responsivity R_{PD} from Table 5.3), the simulated coupling efficiencies (η_{LED} and η_{PD}, from section 5.3), as well as the simulated loss (or transmission T_{IC}) of the integrating cylinder (7.8dB for the cylinder used in this experiment, from Figure 4.2) and the transimpedance amplifier gain ($G = 10^6\Omega$). The strength of the sensing signal (I_{sens}) can be calculated

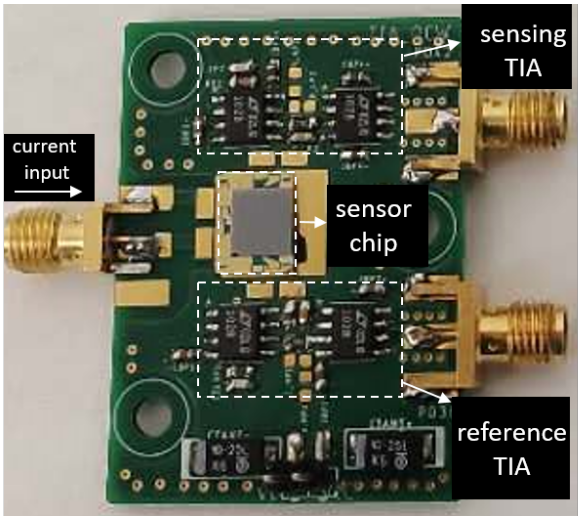

Figure 5.11: PCB consisting of the TIAs for the sensing photodiode and the reference photodiode. The fabricated sensor chip is mounted on the PCB and the contacts pads of the LED/PDs are connected to the board with wire bonds.

by:

$$\begin{aligned} I_{sens} &= P_{LED} \cdot \eta_{LED} \cdot T_{IC} \cdot \eta_{PD} \cdot R_{PD} \cdot G \\ &= 10\mu W \cdot 0.08 \cdot 0.15 \cdot 0.3 \cdot 2.5 A/W \cdot 10^6 \Omega \\ &= 90mV \end{aligned} \tag{5.14}$$

As we used the peak responsivity (R_{PD}) instead of the 'average' responsivity (data not available) of the photodiode in the calculation, the predicted signal strength at the sensing arm is about $90mV/25mV = 3.6$ times larger than the measured value. Other factors such as deviations in the LED output power, the feedback resistance, and the coupling efficiencies can also contribute to the difference between the prediction and the measurement. One can see in the measurement that although the gain of the reference TIA is $5\times$ larger than that of the sensing TIA, the reference signal is still smaller than the sensing signal. This is because the spectral overlap between the response of the reference PD (PD36) and the emission spectrum of the LED is much smaller than that of the sensing PD (PD42) and the LED, as can be seen in Figure 5.5. Moreover, the noise (or deviation) of the reference signal is larger than the noise of the sensing signal, which is due to the difference in the trans-impedance gain. The noise present on the signals can be classified into two types: (1) correlated noise, the correlated noise is the common mode noise present on both arms, and it can originate from factors such as power fluctuations of the LED; (2) un-correlated noise, one example of this type of noise is the noise due to the performance variations of the two PDs (eg. due to temperature fluctuations), the noises produced by the two PDs can be uncorrelated as

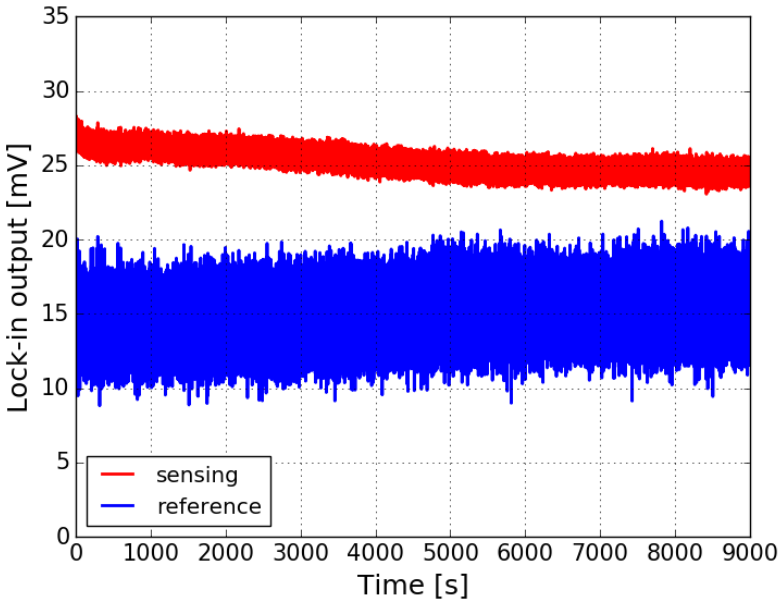

Figure 5.12: The sensing signal and the reference signal measured over a period of 3 hours, the measurement interval is 100 ms.

the two PDs are essentially different and they are placed far apart ($\sim 5mm$). The un-correlated noise can be minimized by signal averaging. To eliminate the correlated noise present on both arms, the following data processing procedure can be applied: (1) the reference signal is scaled by a factor of 1/5, which is ratio of the gain of the TIAs at the sensing arm and the reference arm; (2) an offset is added on the scaled reference signal such that both signals have the same mean values; (3) the sensing signal is then normalized w.r.t the corrected reference signal. The Allan deviations of the sensing signal, the (uncorrected) reference signal, and the normalized signal are calculated and plotted in Figure 5.13. One can see that the minimum deviation of the normalized signal is about 1.2×10^{-3} AU, which is also the detection limit of the system (1σ). The optimal integration time of the lock-in amplifiers (i.e. when Allan deviation of the normalized signal is at its minimum) is approximately 30 seconds.

5.6.2 CO_2 sensing measurement

The response of the fully integrated sensor to CO_2 is measured by purging the sensor with a series of sample gases containing various concentrations of CO_2. In each concentration step, the sensor is first flushed with CO_2 and then with pure N_2.

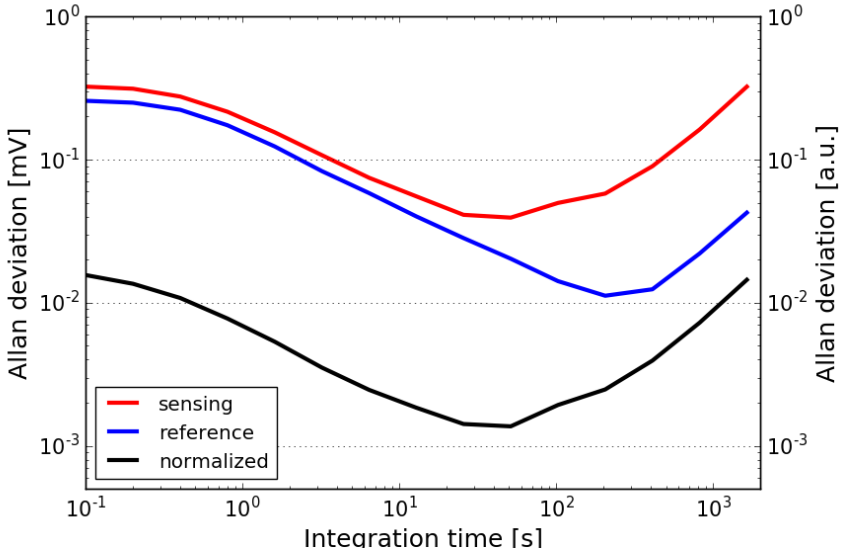

Figure 5.13: (a) Allan deviations of the sensing signal, the reference signal and the normalized signal.

The evolution of the two signals when the CO_2 concentration is varied is shown in Figure 5.14 (a). The letters from A to I correspond to different CO_2 concentrations which are listed on the right side of the figure, the signals are measured with an integration time of 30 seconds. It can be seen that for the sensing signal, a step response to CO_2 concentration changes is present, while the reference signal stays relatively stable, which is due to the lack of spectral overlap between the spectral response of the reference photodiode and the CO_2 absorption spectrum. To eliminate the common mode noise present on both signals, the sensing signal is normalized w.r.t the reference signal, and the results are shown in 5.14 (b). It can be seen that unlike the case in the 'passive' measurement of the integrating cylinder presented in Chapter 4, where the deviation of the normalized signal is relatively small (as shown in Figure 4.19(b)), the normalized signal for the full sensor is still quite noisy. This is because in the fully integrated sensor case, two different photodiodes and TIAs are used, thus the sensing and the reference arms are not balanced. Moreover, the sensing signal and the reference signal have opposite temperature coefficients, which will become clear in section 5.6.5. This opposite temperature coefficients make the normalized signal less immune to the low-frequency noise due to temperature fluctuations.

The normalized absorbance S_{norm} for each CO_2 concentration step, calculated using Eq.4.27, is shown in Figure 5.15. The limit of detection of the full sensor

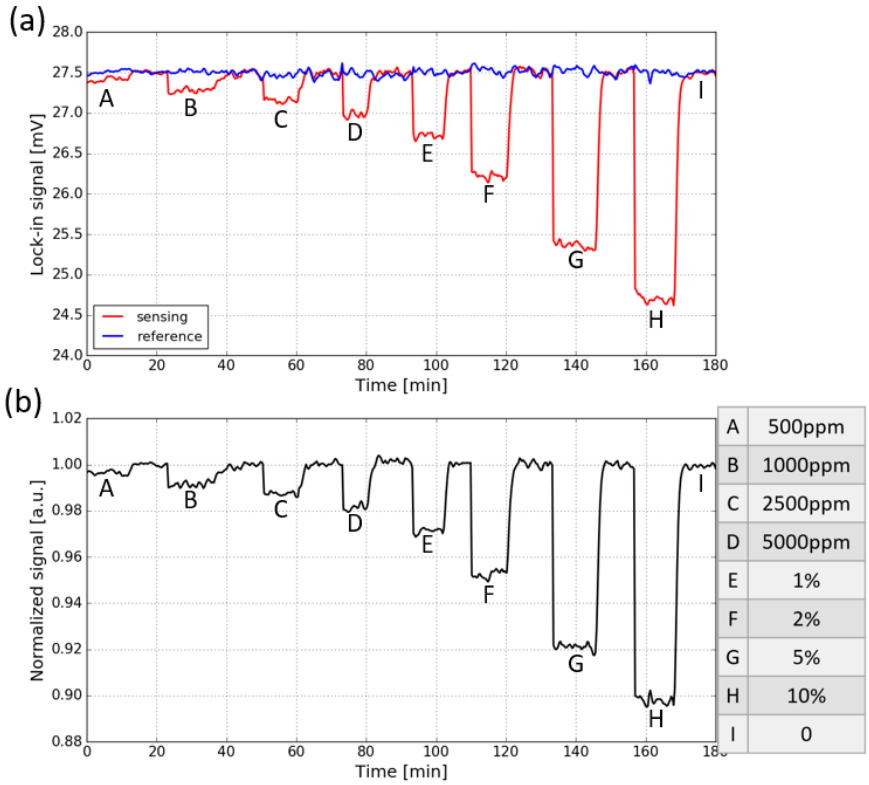

Figure 5.14: (a) Response of both the sensing signal and reference signal to CO_2 concentration steps, the signals are measured with an integration time of 30s. (b) Normalized transmission, obtained by dividing the sensing signal with the reference signal. The CO_2 concentration steps are listed on the right side.

is about 250 ppm (for 1σ), which is significantly larger than the limit of detection of the 'passive' integrating cylinder as presented in Chapter 4. The reasons for this deterioration are three-fold: (1) the bandwidth of the LED emission (FWHM = 800 nm) is larger than the bandwidth of the optical filter (FWHM = 500 nm) used in passive measurement of the integrating cylinder, which leads to a larger 'dilution' of the CO_2 absorbance over the bandwidth; (2) for the passive measurement of the integrating cylinder, an ultra-stable optical source is used, while there is no stabilization circuit for the LED of the full sensor. In principle the power fluctuations of the LED can be eliminated by normalizing the sensing signal w.r.t the reference signal, however, the two arms are not perfectly balanced due to the differences in the sensing arm and the reference arm (PDs and TIAs). (3) the shunt resistance of the photodiodes in the full sensor are much smaller than that of the photodiodes used in the passive measurement (30Ω vs. $300k\Omega$), which gives a

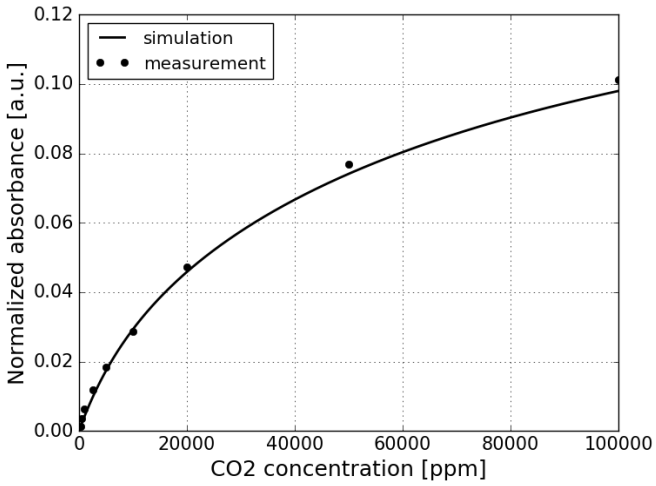

Figure 5.15: Normalized absorbance of the full sensor at different CO_2 concentrations.

much larger noise at the input of the TIA circuit. In principle a longer signal averaging time can minimize this noise contribution, however, a long averaging time makes the photodiodes vulnerable to temperature fluctuations as the temperature coefficients of the two photodiodes are different. The temperature dependence of the photodiodes will be discussed in section 5.6.5.

The normalized absorbance can also be calculated in the same manner as in section 4.6.2, which can be mathematically described by the following formula:

$$\begin{aligned} S_{norm}(c) &= 1 - \frac{I_A(c)}{I_{0A}(c=0)} \\ &= 1 - \frac{\int_{\lambda_1}^{\lambda_2} P(\lambda)\cdot\exp[-\alpha(\lambda)\cdot L\cdot c]\cdot R(\lambda)\, d\lambda}{\int_{\lambda_1}^{\lambda_2} P(\lambda)\cdot R(\lambda)\, d\lambda} \end{aligned} \tag{5.15}$$

where I_A and I_{0A} are the sensing signals with/without the presence of CO_2, respectively. The difference of the upper and lower bounds (λ_1 and λ_2) of the integral represents the wavelength range of interest. $P(\lambda)$ is the emission spectrum of the LED, $R(\lambda)$ is the responsivity function of the sensing photodiode. The term $\exp[-\alpha(\lambda)\cdot L\cdot c]$ represents the absorption of CO_2, with $\alpha(\lambda)$ being the absorption coefficient, and L and c being the equivalent path length and CO_2 concentration, respectively. It can be seen that the agreement between the measurement and the simulation is reasonably good.

5.6.3 Response time

The response time of the fully integrated sensor is measured in the same manner as in section 4.6.3, i.e., the sensor is first flushed with a sample gas containing 50%

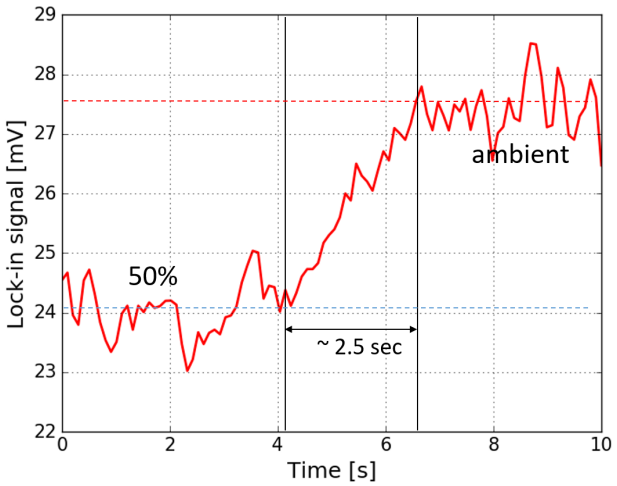

Figure 5.16: Response time measurement of the fully integrated sensor.

CO_2, then the gas flow is abruptly shut off, after which the CO_2 concentration in the sensor reaches ambient level (∼400 ppm) due to gas diffusion. The evolution of the sensing signal is recorded when the reading becomes stable. The sensing signal as a function of time is shown in Figure 5.16, in this measurement we use an integration time of 100ms to resolve the step of the signal. It can be seen that the response time (T_{90}) of the fully integrated sensor is approximately 2.5 seconds. This relatively short response time is sufficient for the leak detection of high CO_2 concentrations (a few percents), where a fast response time is required to give a timely warning signal. However, one should note that a much longer integration time (eg. 30s) is needed to detect ambient-level CO_2 concentrations (a few hundreds of ppm). This long integration time also makes the response time of the sensor much longer, although it is usually not a problem for applications such as air quality monitoring.

5.6.4 Water interference

The accuracy of NDIR gas sensors can deteriorate with the presence of water molecules, which largely depends on the relative humidity (RH) of the environment. Water vapor has a broad absorption in the infrared wavelength range, and this absorption can be significant at some specific wavelengths [26]. Depending on the spectral overlap between the absorption band of the target gas and the water molecules, NDIR gas sensors exhibit different water interference characteristics. The water interference for an NDIR CO_2 sensor is typically very small as

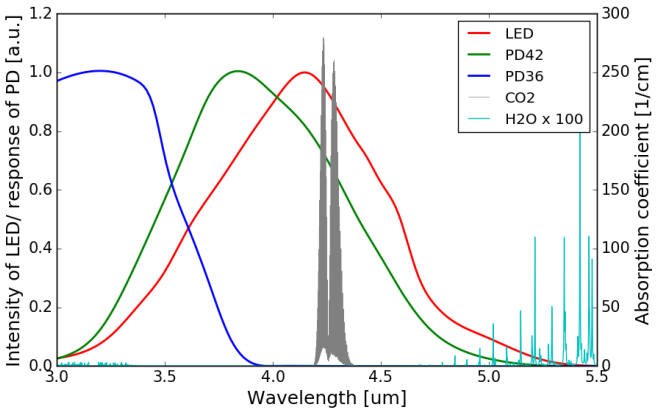

Figure 5.17: Water vapor and CO_2 absorption spectra in $3.0\mu m - 5.5\mu m$ wavelength range [24], together with the emission/responsivity spectra of the LED/PDs. The amplitude of the water vapor absorption spectrum is magnified by a factor of 100.

there is virtually no overlap between the water absorption spectrum and the CO_2 absorption band at $4.2\mu m$. Figure 5.17 shows the absorption spectra of water vapor and CO_2, as well as the emission/responsivity spectra of the LED/PDs in the $3.0\mu m - 5.5\mu m$ wavelength range. It can be seen that the overlaps between the water absorption and the emission spectrum of the LED/spectral responses of the two PDs are negligible. To experimentally evaluate the response of the sensor under different RH levels, we introduce a third gas containing pure N_2 with 100% RH (with flow rate of F_{N_2,H_2O}), obtained by flushing pure N_2 through a bottle with liquid water. Then sample gases with different RH levels can be generated by adjusting the flow rates of the three gases:

$$RH = \frac{F_{N_2,H_2O}}{F_{N_2,H_2O} + F_{N_2} + F_{CO_2}} \times 100\% \tag{5.16}$$

During the measurement, the CO_2 concentration is kept constant at 2500 ppm while the RH level is swept from 0 to 99%. Figure 5.18(a) shows the normalized signal against time. It can be seen that no notable water interference can be observed for the sensor, which means that the cross sensitivity introduced by the water vapor is below the detection limit of the sensor. To determine the magnitude of the cross-sensitivity introduced by water vapor, numerical simulations are carried out. The simulation procedure is the same as in section 5.6.2: propagating the emission spectrum of the LED through the absorption spectra of water vapor (with various RH levels), after which the resulting spectrum is "sampled" by the photodiode by calculating its spectral overlap with the spectral response of the sensing photodiode. The absorbance of the water vapor at various RH levels are plotted in

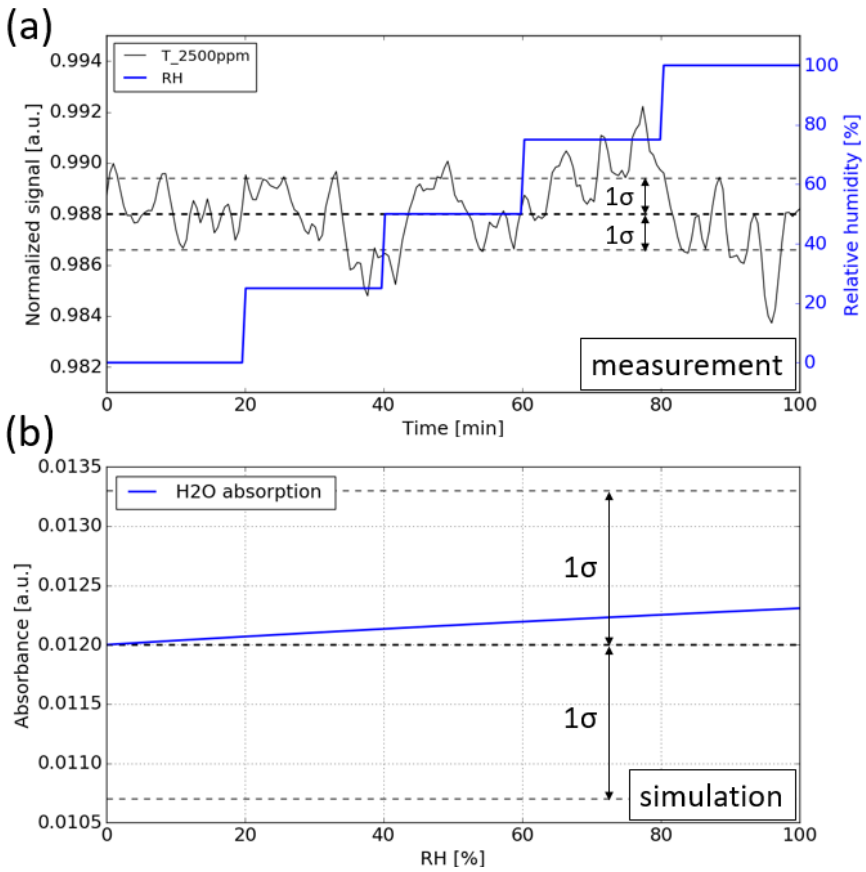

Figure 5.18: (a) Water interference measurement. During the measurement, the RH level is swept from 0 to 99% while the CO_2 concentration is kept at 2500ppm. (b) Simulation of the water vapor absorption at various RH levels, the absorption of water is added on top of the absorption of 2500ppm CO_2.

Figure 5.18(b). The baseline corresponds to the absorbance of 2500ppm CO_2. It can be seen that the absorbance induced by water vapor is within 5e-4, which is much smaller than the detection limit of the sensor (1σ = 1.2e-3).

5.6.5 Long term stability

The stability of the sensor (also known as drift) deals with the degree to which the sensor's characteristics remain constant over time. Changes in stability can be attributed to factors such as temperature fluctuations and component aging. To study the long-term stability of the sensor, we measured the response of the sensor in ambient for a period of $\sim$ five days. Figure 5.19(a) shows both the sensing

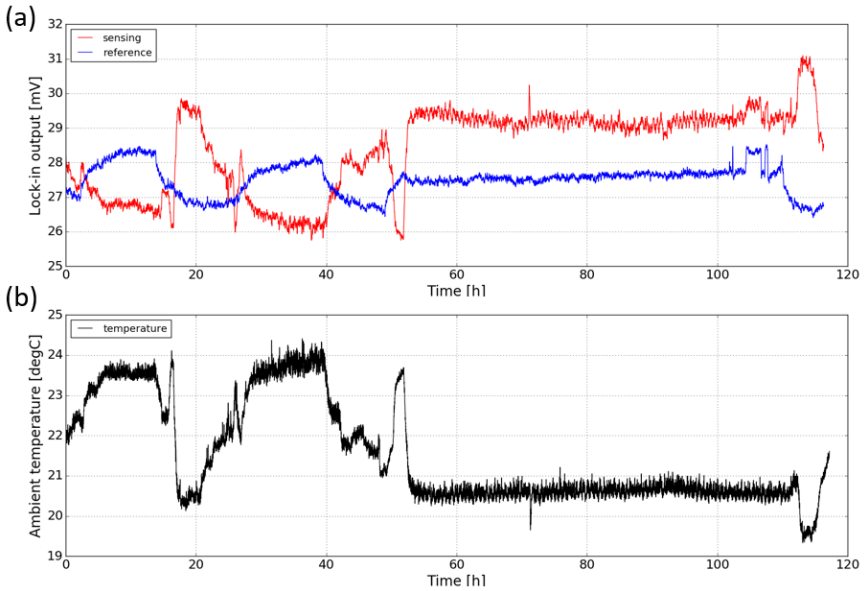

Figure 5.19: (a) Long-term stability measurement of the sensor for a period of ∼ five days. (b) Ambient temperature profile measured with a thermopile detector.

and the reference signal of the sensor against time. It can be seen that during the measurement, both signals exhibit relatively large scale fluctuations (up to 15%), and the sensing signal and the reference signal change in opposite directions. It is believed that the changes in both signals are due to the temperature fluctuations in the laboratory. To test this hypothesis, the ambient temperature during the course of the measurement is also monitored with a thermopile detector (MLX90632, Melexis) and the temperature profile is plotted in Figure 5.19(b). One can see that there is a strong correlation between the ambient temperature and the sensing/reference signals. The opposite correlation between the two signals and the ambient temperature can be explained by the temperature-dependence of the LED and photodiode characteristics as shown in Figure 5.20. When temperature increases, the light intensity of the LED emission decreases and the spectrum slightly red-shifts. Meanwhile the response of the sensing photodiode also decreases and the spectrum also red-shifts, these decreases in both LED emission and photodiode response contribute to the decrease of the sensing signal when the temperature is increased. For the reference photodiode, the spectral response also red-shifts and therefore its spectral overlap with the LED emission spectrum increases, leading to an increase of the reference signal. At this stage of the fully integrated sensor, a strong temperature dependence of the sensor performance was observed, possible approaches to solve this issue will be discussed in Chapter 6.

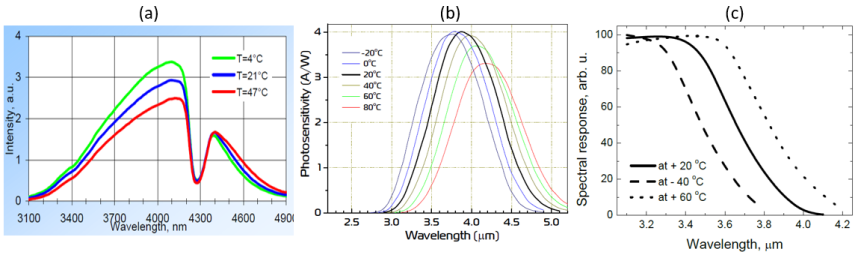

Figure 5.20: Temperature-dependence of the LED/PD characteristics. (a) Emission spectrum of the LED. (b) Spectral response of the sensing photodiode. (c) Spectral response of the reference photodiode. Figures taken from [17], [23], and [18], respectively.

5.7 Conclusions

In this chapter, the characterization of the fully integrated NDIR CO_2 sensor was presented. A mid-IR LED is used as the optical source, and two mid-IR photodiodes are used as detectors for the sensing and the reference arms. The fully integrated sensor is formed by wafer bonding of two silicon substrates. The top substrate contains the integrating cylinder and the LED and photodiodes are integrated on the bottom substrate. The integration procedure involves optical lithography, silicon etching, gold deposition/lift-off and flip-chip bonding. 3D ray tracing simulation was performed to estimate the coupling efficiencies from the LED to the input waveguide of the integrating cylinder and from the output waveguide to the photodiodes. A trans-impedance amplifier (TIA) was designed and fabricated in-house for signal amplification and readout. The design challenges of the TIAs for the photodiodes with low shunt resistance were addressed. The fabricated full sensor was characterized using a dedicated gas sensing setup. CO_2 sensing measurement of the fully integrated sensor was performed, showing a detection limit of $\sim$250ppm (1σ). Compared to the passive measurement of the integrating cylinder presented in Chapter 4, the detection limit is deteriorated, the reasons behind this deterioration were discussed. The cross-sensitivity of the sensor to water vapor was studied both experimentally and numerically. No notable water interference was observed in the experimental characterizations. Numerical simulations reveal that the transmission change induced by water vapor absorption is much smaller than the detection limit of the sensor. A qualitative analysis on the long term stability of the sensor was performed by measuring the response of the sensor for a period of five days. The long term stability of the sensor is subject to the temperature fluctuations in the laboratory. A strong correlation between the sensing/reference signals and the ambient temperature was observed, due to the temperature dependence of the LED/PD characteristics.

References

[1] A Krier and VV Sherstnev. *Powerful interface light emitting diodes for methane gas detection*. Journal of Physics D: Applied Physics, 33(2):101, 2000.

[2] Kyle Thurmond, Zachary Loparo, William Partridge, and Subith S Vasu. *A light-emitting diode-(LED-) based absorption sensor for simultaneous detection of carbon monoxide and carbon dioxide*. Applied spectroscopy, 70(6):962–971, 2016.

[3] Harvey R Hardaway, CT Elliot, Neil T Gordon, and J Graham Crowder. *Optical immersion of mid-infrared LEDs and photodiodes for gas-sensing applications*. In Laser Diodes, Optoelectronic Devices, and Heterogenous Integration, volume 4947, pages 52–58. International Society for Optics and Photonics, 2003.

[4] John Graham Crowder, HR Hardaway, and CT Elliott. *Mid-infrared gas detection using optically immersed, room-temperature, semiconductor devices*. Measurement Science and Technology, 13(6):882, 2002.

[5] Michele Bellancini, Laura Cercenelli, Stefano Severi, Guido Comai, and Emanuela Marcelli. *Development of a CO2 Sensor for Extracorporeal Life Support Applications*. Sensors, 20(13):3613, 2020.

[6] Desmond Gibson and Calum MacGregor. *A novel solid state non-dispersive infrared CO2 gas sensor compatible with wireless and portable deployment*. Sensors, 13(6):7079–7103, 2013.

[7] Anthony Carmine Terracciano, Kyle Thurmond, Michael Villar, Justin Urso, Erik Ninnemann, Akshita Parupalli, Zachary Loparo, Nickolas Demidovich, Jayanta S Kapat, William P Partridge Jr, et al. *Hazardous gas detection sensor using broadband light-emitting diode-based absorption spectroscopy for space applications*. New Space, 6(1):28–36, 2018.

[8] Galina Yu Sotnikova, Gennadyy A Gavrilov, Sergey E Aleksandrov, Alexander A Kapralov, Sergey A Karandashev, Boris A Matveev, and Maxim A Remennyy. *Low Voltage CO _2-Gas Sensor Based on III–V Mid-IR Immersion Lens Diode Optopairs: Where we Are and How Far we Can Go?* IEEE Sensors Journal, 10(2):225–234, 2009.

[9] SS Kizhayev, NV Zotova, SS Molchanov, and Yu P Yakovlev. *High-power mid-infrared light emitting diodes grown by MOVPE*. IEE Proceedings-Optoelectronics, 149(1):36–39, 2002.

[10] Y Aytac, BV Olson, JK Kim, EA Shaner, SD Hawkins, JF Klem, J Olesberg, ME Flatté, and TF Boggess. *Bandgap and temperature dependence of Auger recombination in InAs/InAsSb type-II superlattices*. Journal of Applied Physics, 119(21):215705, 2016.

[11] WK Metzger, MW Wanlass, RJ Ellingson, RK Ahrenkiel, and JJ Carapella. *Auger recombination in low-band-gap n-type InGaAs*. Applied Physics Letters, 79(20):3272–3274, 2001.

[12] Laura Meriggi, Matthew J Steer, Ying Ding, Iain G Thayne, Calum MacGregor, Charles N Ironside, and Marc Sorel. *Development of mid-infrared light-emitting diodes for low-power optical gas sensors*. In 2015 11th Conference on Ph. D. Research in Microelectronics and Electronics (PRIME), pages 180–183. IEEE, 2015.

[13] VK Malyutenko, AV Zinovchuk, and O Yu Malyutenko. *Bandgap dependence of current crowding effect in 3–5 μm InAsSb/InAs planar light emitting devices*. Semiconductor Science and Technology, 23(8):085004, 2008.

[14] VK Malyutenko, O Yu Malyutenko, AD Podoltsev, IN Kucheryavaya, BA Matveev, MA Remennyi, and NM Stus'. *Current crowding in InAsSb light-emitting diodes*. Applied Physics Letters, 79(25):4228–4230, 2001.

[15] VK Malyutenko, O Yu Malyutenko, A Dazzi, N Gross, and J-M Ortega. *Heat transfer mapping in 3–5 μ m planar light emitting structures*. Journal of applied physics, 93(11):9398–9400, 2003.

[16] MK Haigh, GR Nash, SJ Smith, L Buckle, MT Emeny, and T Ashley. *Mid-infrared Al x In 1- x Sb light-emitting diodes*. Applied physics letters, 90(23):231116, 2007.

[17] Independent Business Scientific Group. *LED43 from IBSG*. http://www.ibsg-st-petersburg.com, 2020. Accessed 16 November 2020.

[18] Independent Business Scientific Group. *PD3603 from IBSG*. http://www.ibsg-st-petersburg.com, 2020. Accessed 16 November 2020.

[19] Hamamatsu Photonics. *G15553-003C from Hamamatsu*. https://www.hamamatsu.com/eu/en/product/optical-sensors/photodiodes/ingaas-photodiode/index.html, 2020. Accessed 16 November 2020.

[20] GA Gavrilov, BA Matveev, and G Yu Sotnikova. *Limiting sensitivity of photodetectors based on A 3 B 5 photodiodes for middle infrared range*. Technical Physics Letters, 37(9):866, 2011.

[21] Markus Huuhtanen et al. *Optimal Mid-Infrared Photon Detectors for Use with Voltage-Tunable Filters in Gas Sensing Applications*. 2018.

[22] All about circuit. *Understanding Photovoltaic and Photoconductive Modes of Photodiode Operation*. https://www.allaboutcircuits.com/technical-articles/understanding-photovoltaic-and-photoconductive-modes-of-photodiode-operation, 2021. Accessed 1 January 2021.

[23] Mid-IR Diode Optopair Group. *PD42BS from MidDOG*. http://www.mirdog.spb.ru/products.htm, 2020. Accessed 16 November 2020.

[24] Laurence S Rothman, Iouli E Gordon, Yury Babikov, Alain Barbe, D Chris Benner, Peter F Bernath, Manfred Birk, Luca Bizzocchi, Vincent Boudon, Linda R Brown, et al. *The HITRAN2012 molecular spectroscopic database*. Journal of Quantitative Spectroscopy and Radiative Transfer, 130:4–50, 2013.

[25] Jack R Dixon and James M Ellis. *Optical properties of n-type indium arsenide in the fundamental absorption edge region*. Physical Review, 123(5):1560, 1961.

[26] Sun You-Wen, Liu Wen-Qing, Zeng Yi, Wang Shi-Mei, Huang Shu-Hua, Xie Pin-Hua, and Yu Xiao-Man. *Water vapor interference correction in a non dispersive infrared multi-gas analyzer*. Chinese Physics Letters, 28(7):073302, 2011.

6 Conclusions and Perspectives

6.1 Conclusions

The primary goal of this work was to pursue and develop a miniaturized, low-cost optical CO_2 sensor operating in the mid-IR wavelength range. The applications of such a CO_2 sensor are many-fold. The main drive for this research is leak detection in mobile air conditioning systems. In this case a detection limit of $\sim 1\%$ is sufficient, but the response time of the sensor has to be short to give a timely warning when the leak happens. Other applications include air quality monitoring, greenhouse farming, industrial process control, etc. The requirement on detection limit/resolution is more stringent (sub-100ppm) for these applications, while the response of the sensor can be slow. Different techniques exist today for CO_2 sensing, of which the NDIR technique stands out due to its advantages such as high sensitivity, low cross-sensitivity, and long-term stability. However, the current NDIR CO_2 sensors are bulky as a cm-scale path length is required to achieve a high sensitivity and they are also expensive as they are based on co-assembled discrete optical elements. To address these issues, three on-chip waveguide structures are proposed in this research: the multi-slot silicon waveguide, the hollow metal waveguide, and the hollow metal integrating cylinder. The multi-slot waveguide approach is conceptually novel, however, the fabrication of the waveguides is difficult and is currently not suitable for low-cost and high-volume production. The hollow metal waveguide and the integrating cylinder approaches use gold-coated waveguides for gas sensing, and they can both be implemented on a silicon chip

with wafer-level fabrication processes such as deep reactive ion etching and wafer bonding. The integrating cylinder approach is superior to the hollow waveguide approach in terms of footprint of the sensor. Therefore the integrating cylinder approach was further explored in this work.

We started with the theoretical analysis of the integrating cylinder, and numerical simulations based on ray tracing were performed to determine the optimal parameters of the integrating cylinder. The equivalent path length and the total loss were also extracted from the simulations and they agree well with the predictions from the theoretical calculations. For the experimental demonstration of the integrating cylinder, we chose an integrating cylinder with a radius of 2mm and access widths of $200\mu m$, such a cavity yields an quivalent path length of 3.5cm and a total propagation loss of 7.8dB. The fabrication process of the integrating cylinder was discussed thoroughly, involving deep reactive ion etching, gold deposition and wafer bonding. The proof-of-concept demonstration of the integrating cylinder using an external optical source and detectors indicates a detection limit of 100 ppm and a response time of 3 seconds. Therefore we concluded that the integrating cylinder is a viable approach to achieve a sensitive and fast CO_2 sensor.

A fully integrated CO_2 sensor based on the integrating cylinder was then developed and investigated. A mid-IR LED and two mid-IR photodiode bare chips are used as the optical source and detectors for the sensor respectively. The coupling efficiencies from the LED to the hollow core waveguide (η_{LED}) and from the hollow core waveguide to photodetector (η_{PD}) were estimated by ray tracing simulations, resulting a coupling efficiency of $\eta_{LED} = 8\%$ and $\eta_{PD} = 30\%$. The fabrication process to integrate the LED and photodiodes on-chip was discussed in detail. The use of bare chips allows the integration of the LED/photodiodes with the integrating cylinder using CMOS/MEMS compatible technologies, leading to a fully integrated, miniaturized, low-cost NDIR CO_2 sensor. CO_2 sensing measurements were performed on the full sensor, the fully integrated sensor has a detection limit of $\sim$ 250ppm (1σ). Comparing to the passive measurement of the integrating cylinder using external source and detectors, the detection limit/resolution of the full sensor was compromised due to the lower power spectral density, the imbalance between the sensing and the reference channels, and the different impacts of the ambient temperature on the two photodiodes. NDIR gas sensors are often subject to the interference of other gas species (especially water vapor), in this context the cross-sensitivity of water vapor was studied. The poor spectral overlap between the water absorption spectrum and the emission spectrum of the LED ensures that there are negligible water interference issues. Experimental results confirmed that there was no notable interference from water vapors, further numerical simulations showed that interference induced by water vapor is below the detection limit of our sensor. To investigate the long-term stability and drift of the sensor, the response of the sensor and the ambient temperature were recorded for a few days. The

long-term stability of the sensor was found to be strongly related to the ambient temperature. Opposite correlations between the sensing/reference signal and the ambient temperature were observed, due to the temperature-dependent characteristics of the LED and the two photodiodes. However, this temperature-dependent drift of the sensor can be suppressed by monitoring the chip temperature and use a look up table to compensate for the different sensor and reference PD response.

To conclude, a fully integrated NDIR CO_2 sensor based on an integrating cylinder was developed in this thesis work. The sensor shows a detection limit of 250ppm and a response time of 30 seconds (limited by signal averaging time). Comparing to the state-of-the-art CO_2 sensors on the market as listed in Table 1.1, our sensor has a higher detection limit (750ppm (3σ) *vs.* 50ppm) and a similar response time. Possible approaches to decrease the detection limit of our sensor will be discussed in the next section. While our sensor has a poorer detection limit, it is ~ 10 times smaller than the commercial competitors (5mm *vs.* 5cm), and the expected cost of our sensor is much lower due to the wafer-level fabrication processes of our sensor. At this stage, the CO_2 sensor developed in this work is not yet ready for applications such as air quality monitoring, as it requires a detection limit of sub-100ppm. However, the relatively low cost and small footprint of the sensor are competitive for applications such as in automotive/industrial air conditioning systems and industrial process control, etc.

6.2 Perspectives

6.2.1 Improving the signal to noise ratio

For the prototype demonstration of the fully integrated sensor, the wire-bonding versions of the LED and photodiode bare chips are used. The top point contact and bottom planar contact of the bare chips allow easy access to the LED and photodiodes for driving and for signal readout, and the integration process of the chips is straightforward. However, the input/output waveguide of the integrating cylinder has to remain open for wire bonding of the bare chips. It is beneficial in terms of the response time of the sensor, as the three opened access waveguides allow a fast gas diffusion in and out of the integrating cylinder, leading to a short response time of the sensor. Nevertheless, both the coupling efficiencies from the LED to the input waveguide, and from the output waveguide to the photodiode, are reduced. Therefore, the wire bonding versions of the LED/photodiode bare chips are suboptimal for the sensor in terms of signal to noise ratio. A better solution would be using the flip-chip version of the LED/photodiode chips with top emission/detection, which has both contacts at the bottom of the chips. Therefore, the three access waveguides can be closed and gas access ports can be defined elsewhere on the integrating cylinder, leading to an increase in the coupling efficiencies and the

signal to noise ratio. Further ray tracing simulations show that when both the input waveguide and the output waveguide are closed, the coupling efficiencies from the LED to the input waveguide (η_{LED}) and from the output waveguide to the photodiode (η_{PD}) can be increased by 30% (η_{LED} increased from 8% to 10.4%) and 28% (η_{PD} increased from 30% to 38%), respectively, which increases the signal to noise ratio by a factor of 1.67. During the search for the LED/photodiode chips, several suppliers were contacted, however, the flip-chip version of the bare chips are either not available from those suppliers, or a large order quantity is required for customization. Therefore the flip-chip version of the bare chips was not pursued in this work due to time and budget limitations. In future iterations of the sensor, the use of flip-chip LED/photodiode chips can be explored.

6.2.2 Temperature compensation

The measurement and analysis in section 5.6.5 give a qualitative study of the long term stability of the sensor. At this stage of the sensor development, no temperature control or compensation is implemented in the circuitry, leading to a large dependence of the sensor's response to temperature fluctuations. The influence of temperature can be eliminated or minimized by two approaches: temperature control or temperature compensation. In the temperature control case, a thermoelectric temperature control element can be packaged together with the sensor, therefore the temperature of the sensor chip is fixed during the measurement. Yet, the addition of the temperature control elements increases the complexity and cost of the sensor, and the power consumption of the sensor will also increase as the active cooling is power hungry. In the temperature compensation case, the temperature of the sensor chip is constantly monitored by a temperature sensor, and this temperature information can be used for implementing temperature compensation. In future iterations of the CO_2 sensor developed in this PhD, such a temperature compensation circuit is envisioned. The compensation procedure of the temperature fluctuation is as follows: (1) after fabrication, the sensor is pre-calibrated under various CO_2 concentrations at different temperatures; (2) the temperature-dependent CO_2 response of the sensor is stored in memory, and the calibrated data acts as a 'lookup table' for field measurements; (3) in field measurements, the temperature of the sensor chip is monitored, and the response of the sensor is compared with the lookup table at that particular temperature and the target CO_2 concentration can be extracted.

6.2.3 The shape of the integrating cavity

In the previous chapters, a NDIR CO_2 sensor based on an integrating cylinder was primarily explored. The key benefit of an integrating cylinder is that the incident light is reflected multiple times inside the cavity such that a long optical path length

can be achieved on a small chip area. The integrating cylinder is a direct and the most obvious derivation of the integrating sphere, of which the analysis can be well described mathematically as in Chapter 4. However, the optimal shape of the integrating cavity remains an open question. In future works, the sensing performance of an integrating X (with X being square, rectangle, pentagon, hexagon, etc.) can be explored and compared with the integrating cylinder. The integrating square (a cuboid in 3D) is of particular interest as it yields the largest cavity volume on a give chip area, which can potentially lead to a large CO_2 sensitivity.

6.2.4 Gas membrane

The working environment of the gas sensor can be harsh, and the sensor can be contaminated by eg. dust particles if unprotected. The contamination may 'blind' the sensor and thus measurement error occurs. For commercial gas sensors, porous gas membranes are typically used to cover the diffusion window of the sensor. The gas membranes have microscopic pores with diameters of a few tens of micrometers, and they are effective dust filters that can keep out the dust without compromising the diffusion of the gas. Figure 6.1 shows two examples of the gas membranes used in commercial gas sensors.

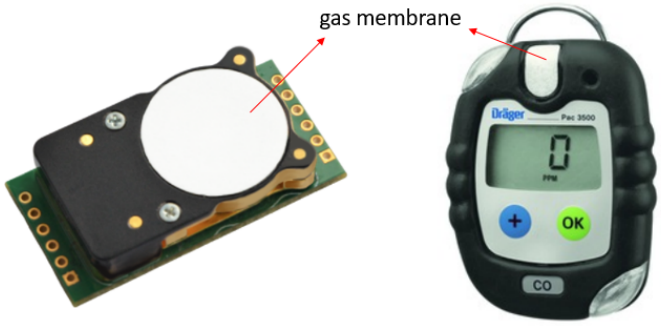

Figure 6.1: Gas membranes used in commercial gas sensors. The two gas sensors are CozIR-LP3 CO_2 sensor from Gas Sensing Solutions, and PAC3500 CO sensor from Draeger, respectively.

6.2.5 LED driver, TIA, and lock-in amplifier

For the proof-of-concept demonstration of the full sensor, an external current source is used to drive the LED and the TIA circuit is soldered on a PCB with discrete electrical components. In future iterations, the LED driver circuit and the TIA circuit can be integrated onto an electrical integrated circuit (EIC) chip, which can be packaged together with the gas sensor, leading to a small overall footprint

of the sensor. Moreover, the functionality of the lock-in amplifiers can also be realized on-chip, by integrating the lock-in circuit on an application-specific integrated circuit (ASIC) chip or using a micro-controller.